Development of Superconducting Nanowire Single Photon Detector Technologies for Advanced Applications

by

Edward Schroeder

A Dissertation Presented in Partial Fulfillment
of the Requirements for the Degree
Doctor of Philosophy

Approved June 2018 by the
Graduate Supervisory Committee:

Philip Mauskopf, Chair
Ralph Chamberlin
Damien Easson
Stuart Lindsay
Nathan Newman

ARIZONA STATE UNIVERSITY

August 2018

ABSTRACT

Measurements of the response of superconducting nanowire single photon detector (SNSPD) devices to changes in various forms of input power can be used for characterization of the devices and for probing device-level physics. Two niobium nitride (NbN) superconducting nanowires developed for use as SNSPD devices are embedded as the inductive (L) component in resonant inductor/capacitor (LC) circuits coupled to a microwave transmission line. The capacitors are low loss commercial chip capacitors which limit the internal quality factor of the resonators to approximately $Qi = 170$. The resonator quality factor, approximately $Qr = 23$, is dominated by the coupling to the feedline and limits the detection bandwidth to on the order of 1MHz. In our experiments with this first generation device, we measure the response of the SNSPD devices to changes in thermal and optical power in both the time domain and the frequency domain. Additionally, we explore the non-linear response of the devices to an applied bias current. For these nanowires, we find that the band-gap energy is $\Delta_0 \approx 1.1$meV and that the density of states at the Fermi energy is $N_0 \sim 10^{10}/\mathrm{eV}/\mu\mathrm{m}^3$.

We present the results of experimentation with a superconducting nanowire that can be operated in two detection modes: i) as a kinetic inductance detector (KID) or ii) as a single photon detector (SPD). When operated as a KID mode in linear mode, the detectors are AC-biased with tones at their resonant frequencies of 45.85 and 91.81MHz. When operated as an SPD in Geiger mode, the resonators are DC biased through cryogenic bias tees and each photon produces a sharp voltage step followed by a ringdown signal at the resonant frequency of the detector. We show that a high AC bias in KID mode is inferior for photon counting experiments compared to operation in a DC-biased SPD mode due to the small fraction of time spent near the critical current with an AC bias. We find a photon count rate of $\Gamma_{KID} = 150$ photons/s/mA in a critically biased KID mode and a photon count rate of $\Gamma_{SPD} = 10^6$ photons/s/mA in SPD mode.

This dissertation additionally presents simulations of a DC-biased, frequency-multiplexed readout of SNSPD devices in Advanced Design System (ADS), LTspice, and Sonnet. A multiplexing factor of 100 is achievable with a total count rate of > 5MHz. This readout could enable a 10000-pixel array for astronomy or quantum communications. Finally, we present a prototype array design based on lumped element components. An early implementation of the array is presented with 16 pixels in the frequency range of 74.9 to 161MHz. We find good agreement between simulation and experimental data in both the time domain and the frequency domain and present modifications for future versions of the array.

DEDICATION

I would like to dedicate my work to four individuals who have been instrumental to my successes leading up to this point. First, to my uncle, Kevin Anderson, who inspired me to study the universe in the earliest years of my life. I recall many days spent with him in front of his computer looking up information on astronomical phenomenon and the latest happenings with NASA. I sincerely thank you for your attention and for passing on your love of space to me.

Secondly, to my mom, Kathy Schroeder, who encouraged me to follow my dreams. She bought me my first book on outer space. I remember reading it over and over again and reciting the order of the planets to my friends on the bus to and from elementary school. Thank you for always believing in me and helping with everything you possibly could along the way.

Dogs are notorious for being man's best friend, and I am lucky enough to have a beagle-weagle who stayed up on late nights as I wrote my dissertation. Thank you, Louie, for being by my side late into the night as I worked. I appreciate your companionship.

Lastly, to my girlfriend, Brittany Barnes, who supported me throughout the process of graduate school and this dissertation. We met when I was going through the ordeal that was the written and oral qualifying exams. Despite the uncertainty and insanity of the last several years, you have been my constant. Thank you for your love and dedication to our future. You complete me.

ACKNOWLEDGMENTS

I would like to first thank the person who contributed the most to my success as a graduate student, Hamdi Mani. Without his tireless effort and dedication to helping me set up and complete my measurements, I would not have finished this doctoral program. Hamdi doesn't give up. Despite the frustrations involved with my project, he stood by me and supported me every step along the way. As far as I'm concerned, there is no greater electronics engineer than Hamdi. He taught me everything that I know about electrical engineering including RF/microwave circuit- and system-level design, testing, and electronics microassembly. I am inspired by his passion for his work and I look forward to seeing the undoubtedly great things he accomplishes in the near future. I am also thankful for his, as everyone that knows him would attest to, unique personality. He is a good person and a great friend. I sincerely thank him for all of the time (including the countless late nights) that he spent helping me achieve what, at times, seemed impossible.

Additionally, I would like to thank Sean Bryan for his mentorship and for his friendship. Like Hamdi, (and as everyone that knows him would attest to) Sean has a very unique personality. He can spend hours talking about Cleveland (and/or the rust belt and/or the famous rest stop at Angola with the pedestrian bridge that crosses the highway) before getting to the point of a discussion about something completely unrelated, like the results of an experimental run for example. When he does get to the point though, there is no one better to explain the intricacies of anything involving physics and measurement in an accessible way. That isn't to say Sean's incessant tangents are a hindrance to his helpfulness as I wouldn't have it any other way. It is what makes Sean who he is. He was absolutely essential to the early days of my involvement with superconducting nanowires. He taught me everything that I know about cryogenics and data analysis. Without his expertise in these subjects and in scientific instrumentation, I would have been lost in a vast sea of confusion. Sean is one of the most intelligent people I know and I thank him for his constant service to me and my project.

Two other members of the Astronomical Instrumentation Lab deserve to be acknowledged. The first is Nathan Smith. Nathan was the first graduate student that I worked with in the lab. We spent a lot of time together counting photons and discussing his crazy ideas for fantastical animated stories and tabletop games. Nathan is very creative and has a lot to offer the world with respect to his imagination. I am glad that he has seen success with this passion. The second is Adrian Sinclair. Adrian was always excited to discuss science with me and I greatly appreciated that. It was a great way to reignite my interest and motivation to study physics. He is extremely hard working and probably the most dedicated student that I have ever met. I very much enjoyed my time in graduate school with both of these individuals and I wish them the best in their futures.

I would like to thank Brandon Butler and George Che for their friendship in graduate school. Brandon and I spent a lot of time together working throughout the night to finish tedious and exceedingly difficult homework sets. We spent a lot of time drinking coffee and eating lunch while discussing the difficulties of our graduate program. We also spent a lot of time at the gym and I thank him for all the years of spotting me during those grueling powerlifting sessions. George and I became good friends after we traveled to Scotland together for a conference. We stayed up all night more than a couple times finishing our respective presentations in the hotel room. George is very organized and when it comes to traveling, I thank him for efficiently exploring Edinburgh, Bath, and London with me. We also traveled to Japan together for a conference and I likewise thank him for his companionship during that trip. I also thank George for pleasant lunchtime conversations and for lifting with me at the gym.

I would be remiss if I did not acknowledge my friends from my time at the University of Rochester, especially those with which I have kept most connected up until this point. First is Dan Gresh. I thank him for useful conversation throughout the years and for keeping me sane (or insane, maybe). Dan is a model physicist and an even better powerlifter. He taught me everything I know about powerlifting and it has been a constant discussion between us for over ten years now. Without powerlifting, the frustrations of graduate school may have taken an even heavier toll. I would also like to thank Tim DeHaas and Travis Kneen. Both of have visited me in Tempe and have kept me connected with my experiences at Rochester that made me, for better or for worse, who I am today. I feel very fortunate to have such long-standing friends. Rascal.

Thank you to Brittany's friends who have become my friends as well. I have been included in countless adventures throughout the years and for that I am very thankful. Without discontinuities in and distractions from the graduate school process, one would go (more) insane. Thank you especially to Derek Montiel for his friendship. Derek is also one of those very unique individuals in my life that has had a great influence on me. I look forward to having more insane exploits with him in the future.

Thank you to my family. My mom, Kathy, my dad, Doug, and my sisters, Jamie and Karen, drove with me across the country from Sinclairville, NY to Tempe, AZ when I moved to Arizona in 2011 to attend ASU for graduate school. Thank you to my grandma, Marilyn Anderson, for everything that she did for me and for my sisters while we were growing up. I thank them all for their support and love. I would also like to thank the Barnes family for accepting me into their family and inviting me to participate in holiday celebrations. They have provided me with a home away from home and for that I am very thankful.

Finally, I would like to acknowledge my supervisory committee for agreeing to support me and my work leading up to this dissertation. I would especially like to thank my advisor, Phil Mauskopf, for allowing me to work with him. His knowledge of device-level physics and his ability to come up with new and useful ideas for astronomical instruments to study the universe is unparalleled. I admire his intelligence and thank him for everything that he has done to allow me to finish this dissertation.

CONTENTS

LIST OF TABLES

Table Page

LIST OF FIGURES

Figure Page

Figure Page

Figure Page

Chapter 1

INTRODUCTION

"*All the fifty years of conscious brooding have brought me no closer to answer the question, 'What are light quanta?' Of course today every rascal thinks he knows the answer, but he is deluding himself.*"
–Albert Einstein

A single photon is the smallest possible discrete unit of light. The most sensitive detectors are therefore required to analyze single photons. This chapter begins with a description of the physical properties of single photons and the fields which they compose and follows up with a short history leading up to the advent of superconducting single photon detectors (SSPD). This includes a discussion on the photoelectric effect, photomultiplier tubes (PMT), and single photon avalanche diodes (SPAD). Additionally, an overview of the two detector types relevant to the content in this dissertation, superconducting nanowire single photon detectors (SNSPD) and kinetic inductance detectors (KID), is presented. Finally, superconducting nanowire resonator single photon detectors (SNRSPD), the merger of these two detector types and the focus of this dissertation, are discussed.

Table 1: Physical Properties of Single Photons.

Property	Value
Mass	0
Charge	0
Spin	1

1.1 Single Photons

1.1.1 Physical Properties

Photons are one of many elementary particles and, in particular, are classified as gauge bosons. A bosonic particle is not restricted by the Pauli exclusion principle to singularly occupy a particular quantum state. Gauge bosons are integer spin particles that carry the fundamental interactions of nature; moreover, they are force carriers. Specifically, photons carry the electromagnetic force in the form of virtual particles. This can be represented in a spacetime diagram called a Feynman diagram. Figure 1 shows the Feynman diagrams for the photon propagator and the annihilation of an electron and its antiparticle, the positron. The photon propagator (Figure 1a) is a function that describes the amplitude of the probability that a particle will travel from one spacetime point to another spacetime point. In Figure 1b, the photon propagator represents the exchange of a virtual particle and specifies the rate of the $e^+e^- \to \mu^+\mu^-$ event.

More important to the present dissertation is that photons are the substance of

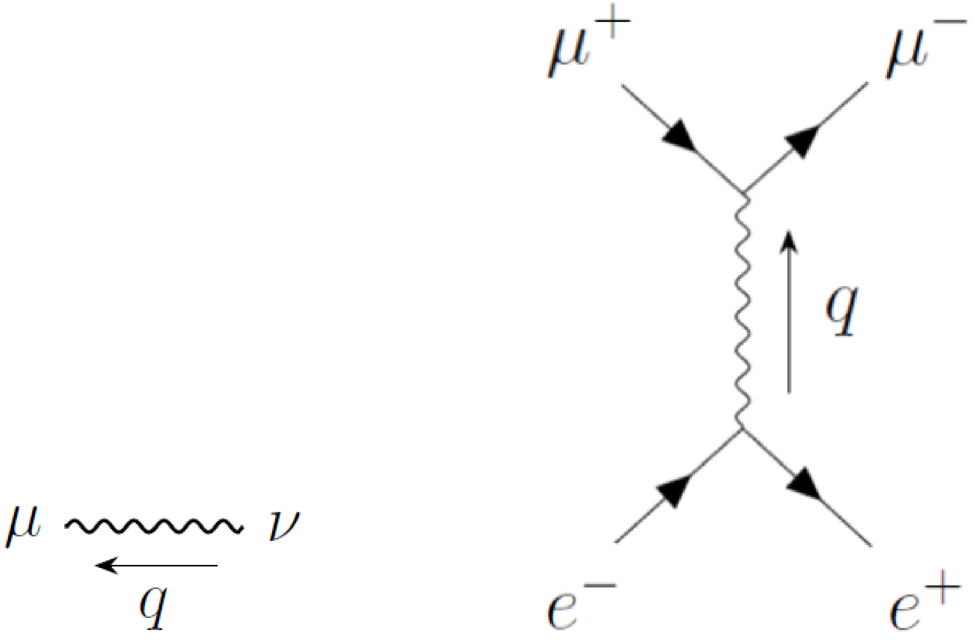

(a) (b)

Figure 1: Feynman diagrams: (a) photon propagator, (b) electron-positron annihilation ($e^+e^- \rightarrow \mu^+\mu^-$).

electromagnetic radiation. Electromagnetic radiation moves at $c = 3 \times 10^8$m/s within a vacuum. A photon does not carry any charge and is a massless particle (Table 1). Regardless of its zero mass, a photon does carry momentum and therefore can exert force on matter. This can be shown with the relativistic relation between energy and momentum given by

$$E^2 = p^2c^2 + m^2c^4, \tag{1.1}$$

where E is the energy of a photon, p is the momentum, c is the speed of light, and m is the mass. For m = 0, we arrive at

$$p = \frac{E}{c}, \tag{1.2}$$

where the Planck relation $E = h\nu$ gives

$$\vec{p} = \hbar\vec{k}, \tag{1.3}$$

where $\hbar$ is the reduced Planck constant and $|\vec{k}| = 2\pi/\lambda$ is the magnitude of the wave vector. ν is the frequency of the radiation and λ is the wavelength and they are related with $c = \nu\lambda$.

Photons also carry angular momentum and, in particular, spin angular momentum and orbital angular momentum. These two components of the angular momentum are independent. Spin angular momentum is the component of the angular momentum that corresponds to the polarization of the photon and is a quantum observable. For a single photon, spin angular momentum has two possible eigenvalues and, therefore, two possible eigenstates given by

$$\vec{S}_z = \pm\vec{\hbar}, \tag{1.4a}$$

$$|\pm\rangle = \frac{1}{\sqrt{2}} \begin{pmatrix} 1 \\ \pm i \end{pmatrix}, \tag{1.4b}$$

where these two states represent the left-handed and right-handed circular polarizations of the photon. The spin angular momentum of a single photon is easy to measure using a waveplate and a polarizing beam splitter (Beijersbergen et al. 1994).

Orbital angular momentum states are not as easily measured due to having an infinite number of possible orthogonal eigenstates (Molina-Terriza, Torres, and Torner 2001). The eigenvalues of orbital angular momentum are given by

$$\vec{L}_z = m\vec{\hbar}, \tag{1.5a}$$

$$\vec{L}^2 = \ell\left(\ell + 1\right)\vec{\hbar}^2, \tag{1.5b}$$

where $m \in \{\ldots, -2, -1, 0, 1, 2, \ldots\}$ and $\ell \in \{0, 1, 2, \ldots\}$. These values determine the wavefront shape. In terms of a single photon, measurement of the azimuthal quantum number, ℓ, can be measured with an interferometric method (Leach et al. 2002) with 100% efficiency.

1.1.2 Black Body Gas

A common example of photonic behavior is black body radiation. A black body is a non-reflective physical object. This object comprises of a system that encompasses a collection of photons. Photons are non-interacting and indistinguishable and, at thermal equilibrium, exhibit a behavior governed by Bose-Einstein statistics (Bose 1924; Einstein 1924). These statistics describe the way a collection of photons in a system may occupy a set of discrete energy states intrinsic to and available within the given system. The statistical properties of a single photon in this system are described by the partition function given by

$$\mathcal{Z} = \frac{1}{1 - \exp\left(\left(\mu - \epsilon\right)/k_B T\right)}, \tag{1.6}$$

where μ is the chemical potential, ϵ is the energy of the photon state, k_B is the Boltzmann constant, and T is the absolute temperature of the system. The average photon number is then given by

$$\langle N \rangle = k_B T \frac{1}{\mathcal{Z}} \left(\frac{\partial \mathcal{Z}}{\partial \mu}\right)_{V,T} = \frac{1}{\exp\left(\left(\mu - \epsilon\right)/k_B T\right) - 1}, \tag{1.7}$$

where the volume V and temperature T of the system is unvarying.

In the case of black body radiation, or a photon gas, $\mu = 0$ due to the lack of a constraint on the number of photons in the system. Moreover, the photon number is not conserved. This can be explained by the possible circumstance arising from a photon of energy E_1 being absorbed by an electron in the wall of the black body cavity. The electron will be excited to a higher energy state. When the electron returns to its initial energy state, it may do so in a series of steps that result in two photons being emitted of energies E_2 and E_3 such that $E_1 = E_2 + E_3$. Furthermore, photons have energy $\epsilon = h\nu$ such that the spectral energy density is given by (Planck 1900)

$$u_\nu d\nu = \frac{8\pi h\nu^3}{c^3}\frac{d\nu}{\exp\left(h\nu/k_B T\right) - 1}, \tag{1.8}$$

where h is the Planck constant and ν is the frequency of the photon. The spectral radiance of the body is then given by

$$B_\nu(T) = \frac{u_\nu(T)c}{4\pi}, \tag{1.9}$$

since the radiation travels at the speed of light in all directions.

1.1.3 Incoherent and Coherent States

A Heisenberg-type order-of-magnitude relationship can be used to describe the level of order in incoherent and coherent states of the radiation field with respect to the frequency span of the field and is given by (Wolf 1958)

$$\Delta\tau_c \Delta\nu \sim 1, \tag{1.10}$$

where $\Delta\tau_c$ is the coherence time and $\Delta\nu$ is the effective spectral frequency range. The coherence time is the time over which a beam of light has a well defined phase relationship and therefore characterizes how dispersed the frequency is over time. The larger the bandwidth of the source, the more polychromatic the light is coming from the source and, therefore, the shorter the coherence time is.

Incoherent light is a state of the radiation field with a coherence time that approaches zero. This occurs with a field that has randomly varying phase and amplitude. To see this, consider the wave equation of light given by

$$\Box\Psi = 0, \tag{1.11}$$

where $-\Box = \vec{\nabla}^2 - c^{-2}(\partial^2/\partial t^2)$ is the d'Alembert operator and Ψ is the generic waveform upon which it acts. By experimentation, we know that electromagnetism is linear. Therefore, we have the following constraints for some constants, α and β:

$$\Box\left(\alpha\Psi\right) = 0 \rightarrow \alpha\Box\Psi = 0, \tag{1.12a}$$

$$\Box\Psi = 0 \rightarrow \Box\left(\alpha\Psi_1 + \beta\Psi_2\right) = 0 \rightarrow \alpha\Box\Psi_1 + \beta\Box\Psi_2 = 0, \tag{1.12b}$$

where Equation 1.12a demonstrates homogeneity and Equation 1.12b demonstrates additivity. These properties show that electromagnetic radiation conforms to the superposition principle.

The electric field of two plane waves propagating in free space are solutions to Equation 1.11 and can be written as

$$\vec{E}_1 = \vec{E}_{01} e^{i\left(\vec{k}_1\cdot\vec{r} - \omega t + \phi_1\right)}, \tag{1.13a}$$

$$\vec{E}_2 = \vec{E}_{02} e^{i\left(\vec{k}_2\cdot\vec{r} - \omega t + \phi_2\right)}, \tag{1.13b}$$

where $\vec{E}_0$ is the peak magnitude of the oscillation, $\vec{k}$ is the wavenumber, $\vec{r}$ is the position vector, ω is the angular frequency, and ϕ is the phase. The total electric field is just the addition of the two fields given by

$$\vec{E}_T = \vec{E}_1 + \vec{E}_2 = e^{-i\omega t}\left[\vec{E}_{01} e^{i\left(\vec{k}_1\cdot\vec{r} + \phi_1\right)} + \vec{E}_{02} e^{i\left(\vec{k}_2\cdot\vec{r} + \phi_2\right)}\right]. \tag{1.14}$$

The time-averaged intensity of the total field is then given by

$$I_T = \langle \vec{E}_T \cdot \vec{E}_T^{*} \rangle = I_1 + I_2 + 2\sqrt{I_1 I_2}\cos\delta, \tag{1.15}$$

where $\delta = (\vec{k}_1 - \vec{k}_2)\cdot\vec{r} + (\phi_1 - \phi_2)$ is the phase difference between the two waves. One can imagine a superposition of N fields with varying frequencies of light. The intensity of an incoherent source shifts with time as the phase difference changes between the multiple frequencies of light. Thermal light is one such field that exhibits incoherence.

Consider again N harmonic oscillators such that the total field is given by

$$E(t) = \sum_{j=1}^{N} E_0 e^{-i[\omega t - \phi_j(t)]}, \tag{1.16}$$

where $\phi_j(t)$ is the phase of the j-th oscillator. The probability distribution of the time-varying intensity is then given by

$$p(I(t)) = \frac{1}{\langle I(t) \rangle} e^{-I(t)/\langle I(t) \rangle}, \tag{1.17}$$

where $\langle I(t) \rangle = N E_0^2$ is the average intensity of the field and $I(t) = E_0^2 \left|\beta(t)\right|^2$ is the instantaneous intensity. $\beta(t)$ is the sum of the phases of the oscillators and represents the complex amplitude of the total field.

Applying Mandel's formula (Mandel 1959) to Equation 1.17, we arrive at the probability distribution for thermal light given by

$$P_n = \frac{1}{\langle n \rangle + 1} \left(\frac{\langle n \rangle}{\langle n \rangle + 1} \right)^2, \tag{1.18}$$

where n is the number of photon counts registered at an ideal detector. The variance of P_n is given by

$$\Delta n^2 = \langle n \rangle + \langle n \rangle^2 . \tag{1.19}$$

Moreover, for thermal light, the average value of the registered number of photons fluctuates by the square of the average value.

Coherent light is a state of the radiation field with a coherence time that is infinite since the intensity is constant over time and is best handled with a quantum mechanical analysis. A single photon detection can be represented with an operation on the oscillator state given by (Mandel and Wolf 1965)

$$\hat{a} \left|\alpha\right\rangle = \alpha \left|\alpha\right\rangle , \tag{1.20}$$

where $\hat{a}$ is the annihilation operator and $\left|\alpha\right\rangle$ is the single-mode wave function of the photon field. The state of the field is coherent if it satisfies this equation because when $\hat{a}$ acts on $|\alpha\rangle$, the state remains unchanged. In this way, the phase of the field is preserved upon detection, or annihilation, of a photon.

Consider the photon number eigenstate equation for the quantum harmonic oscillator given by

$$\hat{n}\,|n\rangle = n\,|n\rangle\,, \tag{1.21}$$

where n is the number of photons in the field, $\hat{n}$ is the photon number operator, and $|n\rangle$ is the wave function. $|n\rangle$ is given by

$$|n\rangle = \frac{1}{\sqrt{n!}}\left(\hat{a}^{\dagger}\right)^{n}|0\rangle\,, \tag{1.22}$$

where $\hat{a}^{\dagger}$ is the creation operator. For a full analysis of the harmonic oscillator state see Appendix I.

We follow a derivation of the coherent states of a single-mode oscillator (Glauber 1963). We begin by taking the inner product on both sides of Equation 1.20 with the arbitrary excited state given by Equation 1.21:

$$\langle n|\,\hat{a}\,|\alpha\rangle = \alpha\,\langle n|\alpha\rangle\,. \tag{1.23}$$

It follows from Equation A18a that $\langle n|\,\hat{a} = \sqrt{n+1}\,\langle n+1|$, such that Equation 1.23 takes the following form:

$$\sqrt{n+1}\,\langle n+1|\alpha\rangle = \alpha\,\langle n|\alpha\rangle\,. \tag{1.24}$$

It is then clear that the inner products $\langle n|\alpha\rangle$ are recursive and given by

$$\langle n|\alpha\rangle = \frac{\alpha^{n}}{\sqrt{n!}}\,\langle 0|\alpha\rangle\,, \tag{1.25}$$

where we obtain the oscillator state $|\alpha\rangle$ via a summation over all states with $\langle n|\alpha\rangle$ as the expansion coefficients:

$$|\alpha\rangle = \sum_{n}|n\rangle\,\langle n|\alpha\rangle = \langle 0|\alpha\rangle\sum_{n}\frac{\alpha^{n}}{\sqrt{n!}}\,|n\rangle\,. \tag{1.26}$$

It remains to us to find the factor $\langle 0|\alpha\rangle$ via normalization and invoking the definition of the exponential function:

$$\begin{aligned} \langle\alpha|\alpha\rangle &= |\langle 0|\alpha\rangle|^2 \sum_n \frac{|\alpha|^{2n}}{n!} = |\langle 0|\alpha\rangle|^2 \exp\left(|\alpha|^2\right) = 1 \qquad (1.27a) \\ \Rightarrow \langle 0|\alpha\rangle &= \exp\left(-\frac{1}{2}|\alpha|^2\right). \end{aligned}$$

Finally, we have the coherent states of the harmonic oscillator given by

$$|\alpha\rangle = \exp\left(-\frac{1}{2}|\alpha|^2\right) \sum_n \frac{\alpha^n}{\sqrt{n!}} |n\rangle . \tag{1.28}$$

Using the Born rule (Born 1926) by projecting the number eigenstate $|n\rangle$ onto the coherent states of the harmonic oscillator we obtain

$$P_n = |\langle n|\alpha\rangle|^2 = \frac{|\alpha|^{2n}}{n!} \exp\left(-|\alpha|^2\right), \tag{1.29}$$

which is of a Poisson distribution form representative of the average occupation number of photons in the n-th state. The variance of P_n is then given by

$$\Delta n^2 = \langle n\rangle . \tag{1.30}$$

Moreover, for coherent light, the average value of the registered number of photons does not fluctuate.

1.1.4 Wave-Particle Duality

Robert Hooke and Issac Newton had differing views on the nature of light. Hooke believed that light was made up of waves (Hooke 1672). On the other hand, Newton was a proponent of the corpuscular theory of light (Newton 1672). It turns out that photons have both wave and particle properties (Bohr 1928). This is best demonstrated

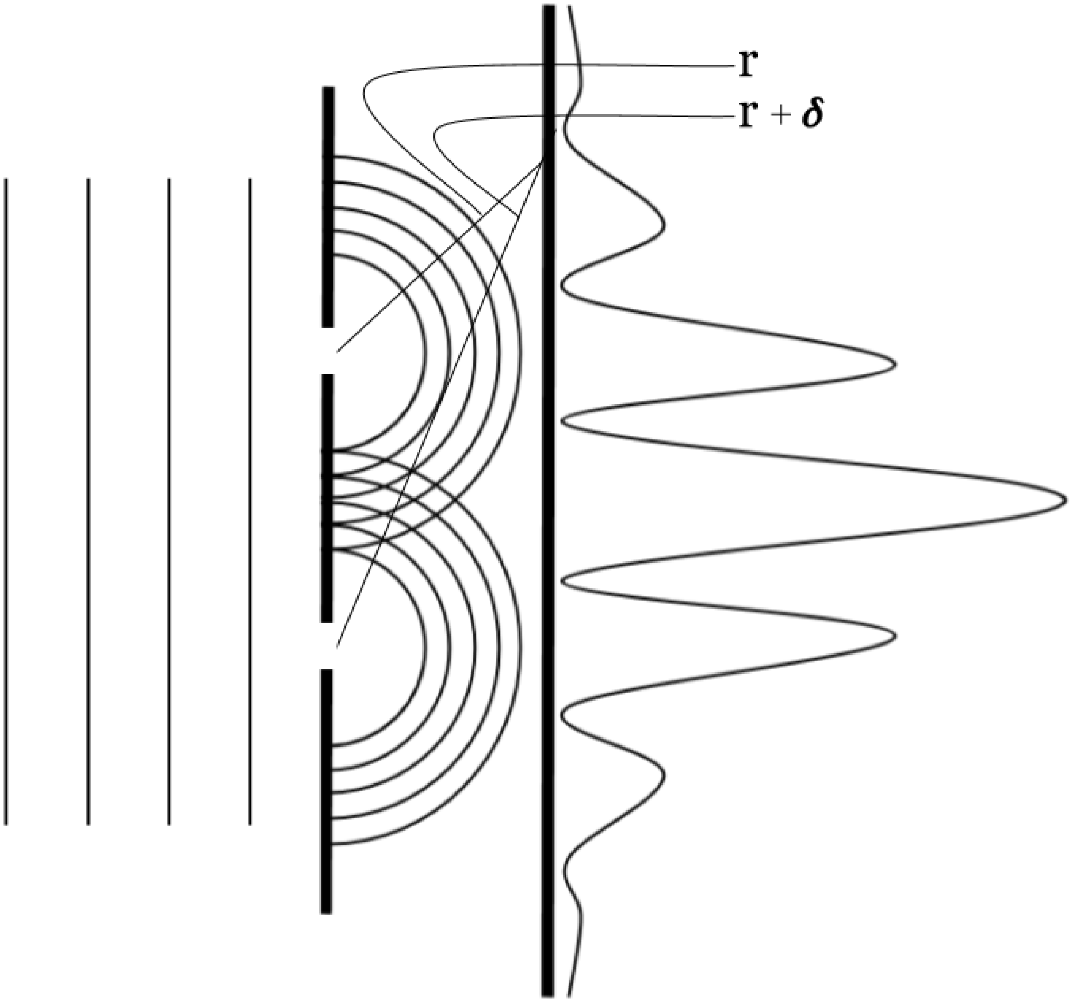

Figure 2: Classic double-slit experiment. Plane waves are incident on two slits. The wavefronts propagate outward to a detector and an interference pattern is observed. Minima pertain to total destructive interference and maxima pertain to total constructive interference.

with the double-slit experiment. The original double-slit experiment was carried out by Thomas Young which displayed the wave nature of light (Young 1802). When waves are incident on small apertures, they diffract. Diffraction in this case is a spreading out of the waves into circular propagating wavefronts. Young's experiment involved two narrow slits upon which monochromatic light was incident. The result was a predictable interference pattern projected onto a flat surface perpendicular to the direction of propagation of the original light waves (Figure 2). The intensity of the resulting light pattern is given by (Jenkins and White 1950)

$$I(\theta) \propto \cos^2(\gamma)\,\mathrm{sinc}^2(\beta)\,, \tag{1.31}$$

where the arguments of the trigonometric functions are given by

$$\gamma = \frac{\pi d}{\lambda}\sin(\theta) \tag{1.32a}$$

$$\beta = \frac{\pi b}{\lambda}\sin(\theta). \tag{1.32b}$$

γ and β are functions of the wavelength of the light λ and the angle θ that defines the path difference between the two waves. d is the distance between the centers of the slits and b is the slit width.

The cosine function in Equation 1.31 is a result of the interference of the two waves due to a phase difference between the waves. The cardinal sine function is a result of single-slit diffraction. Therefore, the intensity observed in the double-slit experiment is zero when either the diffraction term or the interference term is zero. Maxima occur when $\gamma = 0$ which occurs when $d\sin(\theta)$ takes on values that are integer increments of the wavelength of the light. Due to the properties of constructive and destructive interference being being a well-known consequence of interacting waves, it was concluded that light was wave-like.

It may come to no surprise that light has the properties of wave-mechanics, but the double-slit experiment has been performed explicitly with particles that have mass (Donati, Missiroli, and Pozzi 1973; Eibenberger et al. 2013) with an interference pattern result. Therefore, at small scales, relatively massive particles exhibit measurable wave-like properties and wave-particle duality is demonstrated. Additionally, the particle nature of photons has been explored at length (Pfleegor and Mandel 1967, 1968; Grangier, Roger, and Aspect 1986; Mandel 1999).

The peculiarity of the double-slit experiment that makes it a superlative example of wave-particle duality is that the same interference pattern as in Young's continuous wave experiment is obtained when only one particle at a time passes through the double-slitted partition. If the process of the photon passing through one or the other slit is measured, the interference pattern is destroyed. The act of monitoring the path of the photon destroys its wave-like properties. If the photon path is left unchecked, it retains its wave-like properties and an interference pattern is recovered. It can therefore be concluded, since the single photon particle must interfere with itself, that a photon exhibits both wave- and particle-like properties. Moreover, the photon arrives like a particle, but interferes like a wave. The the classical, or wave-like, and quantized, or particle-like, nature of the photon are two detectable conditions of a single object. This necessitates that the photon be considered a quantum object.

1.2 Photon Detectors

1.2.1 The Photoelectric Effect

It turns out, as discussed previously, that light is not a continuous wave but rather composed of discrete quanta of energy called photons. This dissertation is particularly invested in single photon detection and therefore the particle nature of photons. The possibility of the detection of single photons began when Albert Einstein realized why the kinetic energy of electrons being emitted from a metallic surface were independent of the intensity of the light incident on the surface (Einstein 1905).

If the wavelength of a photon that is incident on the surface is below a certain threshold that is defined by the material, electrons will not be emitted because there is

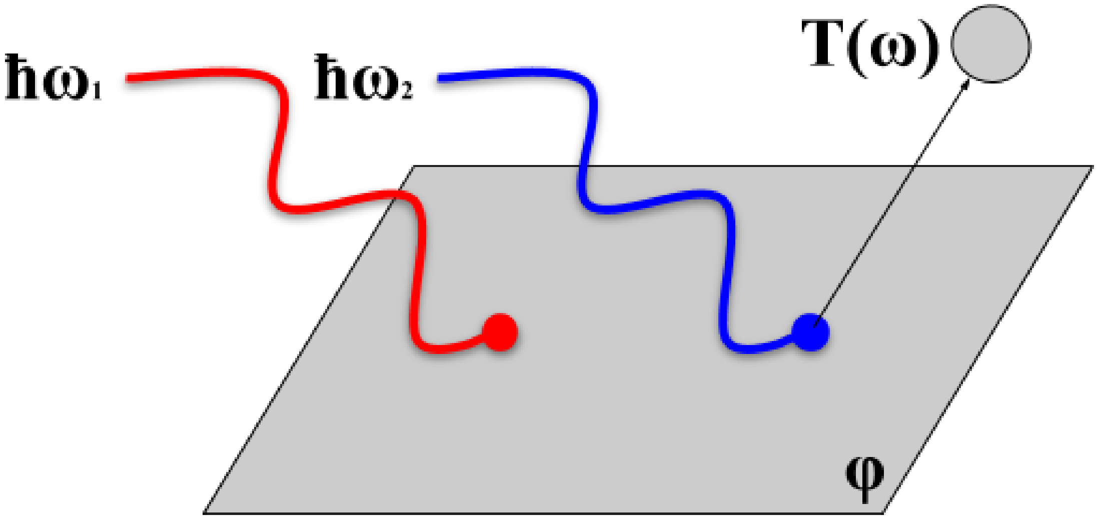

Figure 3: ϕ is the minimum amount of energy required to remove an electron from the metallic surface. Red light ($\hbar\omega_1 < \phi$) is less energetic than blue light ($\hbar\omega_2 > \phi$). Shining light of energy $\hbar\omega > \phi$ on a metallic surface results in the emission of photoelectrons with kinetic energy $T(\omega)$, but light of energy $\hbar\omega < \phi$ will not free an electron. This is called the photoelectric effect.

not a sufficient amount of energy transfered from the photon. No amount of intensity increase of photons below this threshold wavelength will result in an emission event. This is contradictory to the wave-model of light. If the wavelength is above the threshold, then a photoelectron will be emitted with kinetic energy T given by

$$T = E_\gamma - \phi, \tag{1.33}$$

where $E_\gamma = \hbar\omega$ is the energy of the photon and $\phi = \hbar\omega_0$ is the work function of the material.

Figure 3 illustrates the frequency dependence of the emission process. The amount of light incident on the surface does not affect the maximum kinetic energy of the photoelectrons emitted. This is due to the particle nature of light and how energy is transfered to the electrons in the metal. If the intensity of the light in increased, the photoelectrons emitted will retain the same maximum kinetic energy.

1.2.2 Photomultiplier Tubes

One consequence of the photoelectric effect was the invention of the photomultiplier tube (PMT). A PMT is an evacuated glass tube that accepts small light signals and alters the input into a measurable output. PMTs were the first detectors capable of detecting the signals from a single photon (Kiepenheuer 1937; Allen 1939). There are four major components that are necessary for the operation of a PMT: a window, a photocathode, a dynode network, and an anode. The window accepts the photons and contains a thin layer of photo-emissive material. This layer acts as the photocathode in that it emits electrons via the photoelectric effect. The emitted photoelectrons will have kinetic energy equal to the energy of the incident photon minus the work function of the material. The photoelectrons are fed onto the first dynode by electrodes within the tube. The signal is amplified by a cascading of electrons through a network of dynodes coated in emissive material. The anode receives the amassed electrons and produces the measurable output in the form of an electric current.

1.2.3 Single Photon Avalanche Diodes

A single photon avalanche photodiode (SPAD) is another device that operates through the photoelectric effect. SPADs are semiconductor devices that are voltage biased just above the breakdown voltage of the p-n junction (Stipčević, Skenderović, and Gracin 2010). This is the voltage at which the the material to be exposed to

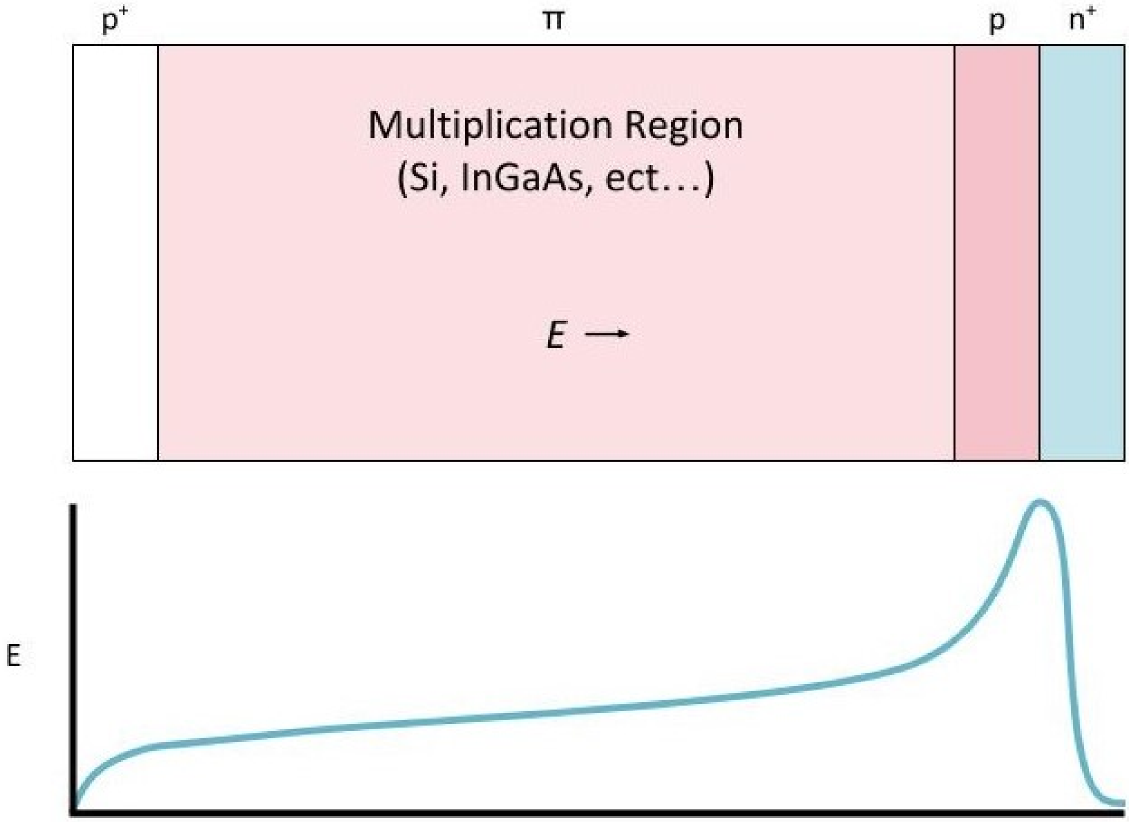

Figure 4: The interior of a SPAD showing how the electric field across the length of the multiplication region induces the avalanche effect.

the photons conducts. A single photon event causes the semiconductor material to conduct and commences the avalanche effect. When a photon creates an electron-hole pair in the multiplication region of a SPAD, the strong electric field formed at the p-n junction motivates impact ionization and results in an avalanche pulse that coincides with a photon arrival. The SPAD returns to an operational state by a reset of the voltage bias. See Figure 4 for a visual representation of how the electric field varies in the detector.

1.2.4 Superconducting Nanowire Single Photon Detectors

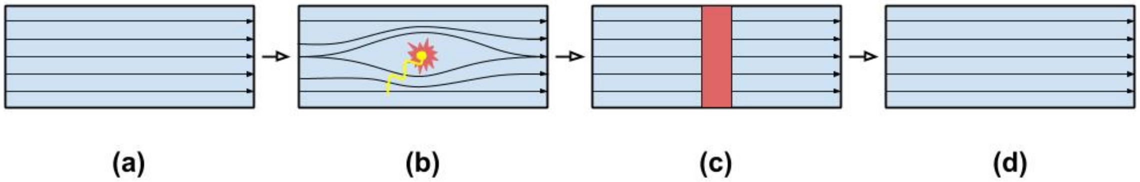

Figure 5: Detection mechanism of an SNSPD. (a) The superconducting state of a section of nanowire biased with a current below the switching current. (b) When a photon is absorbed by the nanowire, it creates a hotspot. The current is diverted around the hotspot. (c) The critical current density is exceeded and a resistive strip is formed across the width of the nanowire, shunting the current and resulting in a readable voltage pulse. (d) The bias current is diverted to the load and the resistive region is dissipated. The nanowire returns to the superconducting state.

Superconducting nanowire single photon detectors (SNSPD) are fabricated with materials that are capable of reaching a superconducting state. One such material is niobium nitride (NbN) (Zhang et al. 2003). When cooled below the critical temperature of NbN, the nanowire becomes superconducting. When the superconducting nanowire is biased close to its switching current, a single photon carries enough energy to drive a section of the nanowire normal (Natarajan, Tanner, and Hadfield 2012).

Initially, the superconducting state of a section of nanowire is undisturbed with a bias current just below the switching current. The switching current is the characteristic current of the material at which superconductivity is destroyed. At some point, a photon strikes this section of the wire. This incident photon is absorbed and a resistive hotspot is formed. The current is repelled to the sides, causing the local current density to exceed the critical current density. The hotspot then grows and switches a local cross section of the nanowire to the resistive state. The current is completely blocked such that a measurable voltage pulse is generated. Finally, since the bias current is diverted to the load, there is not enough current in the nanowire to sustain the generated resistive strip and the nanowire returns to the superconducting state (Figure 5).

The experimental parameters of SNSPD devices consist of detection efficiency, maximum count rate, dark count rate, dead time, and timing jitter. In order for a single photon detector to be maximally useful, it must detect a large fraction of the photons incident on it. This detected fraction is called the detection efficiency. It is the probability that a count is recorded if a photon is incident on the detector. A variety of factors affect the detection efficiency. When the photon field enters the environment of the experimental apparatus, photons may be scattered or absorbed. The geometry of the nanowire and the properties of the film, such as composition and thickness, also determine how many photons are detected. The detection efficiency is highly dependent on the wavelength of the observed radiation (Hofherr et al. 2010).

The count rate is the number of photon counts per second. Only a fraction of the incident photons will be detected as determined by the detection efficiency, but the detector dead time also affects the number of recorded counts. The dead time τ is the amount of time that it takes for the detector to return to a state in which the detector is capable of a second detection. If a photon is incident on the detector during this dead time, it is likely that the photon will not be detected. Likewise, if the detector reaches a saturated state in a time before can it can reset, it will be unable to detect additional incident photons. The maximum count rate (MCR) is related to the dead time by

$$\mathrm{MCR} = \frac{1}{\tau}. \tag{1.34}$$

Dark counts are false counts that are impossible to differentiate from real counts from photons incident on the detector. Dark counts are intrinsic to many detectors due to thermal fluctuations. One source of these fluctuations occurs via blackbody radiation in fiber-coupled devices (Yamashita et al. 2010; Shibata et al. 2013). Another source involves current-assisted unbinding of vortex-antivortex pairs (Yamashita et al. 2011). The dark count rate (DCR) depends on the material used and is the number of dark counts per second. The number of dark counts over the total number of counts gives the probability that a registered count is a dark count. Therefore, the dark count fraction is high if the detection efficiency is low or if the occupation number of the field is low, resulting in a small number of real counts per second.

Timing jitter Δt is the uncertainty in the arrival time of an individual photon. Moreover, it is the spread in the span of time that occurs between the incidence of the photon on the detector and the detection of the corresponding output signal. The typical parameters of the aforementioned single photon detectors are summarized in Table 2. SNSPD devices significantly outperform PMTs and SPADs at the operating wavelength of 1550nm.

Table 2: Typical parameters of single photon detectors (Hadfield 2009). T_{op} is the operating temperature, η is the detection efficiency, Δt is the timing jitter, DCR is the dark count rate, and MCR is the maximum count rate.

Detector	T_{op}(K)	η(%@1550nm)	Δt(ps)	DCR(Hz)	MCR(MHz)
PMT(InP/InGaAs)	200	2	300	2×10^5	10
SPAD(InGaAs)	200	10	370	91	0.01
SNSPD(NbN)	1-4	57	30	10	1000

1.2.5 Kinetic Inductance Detectors

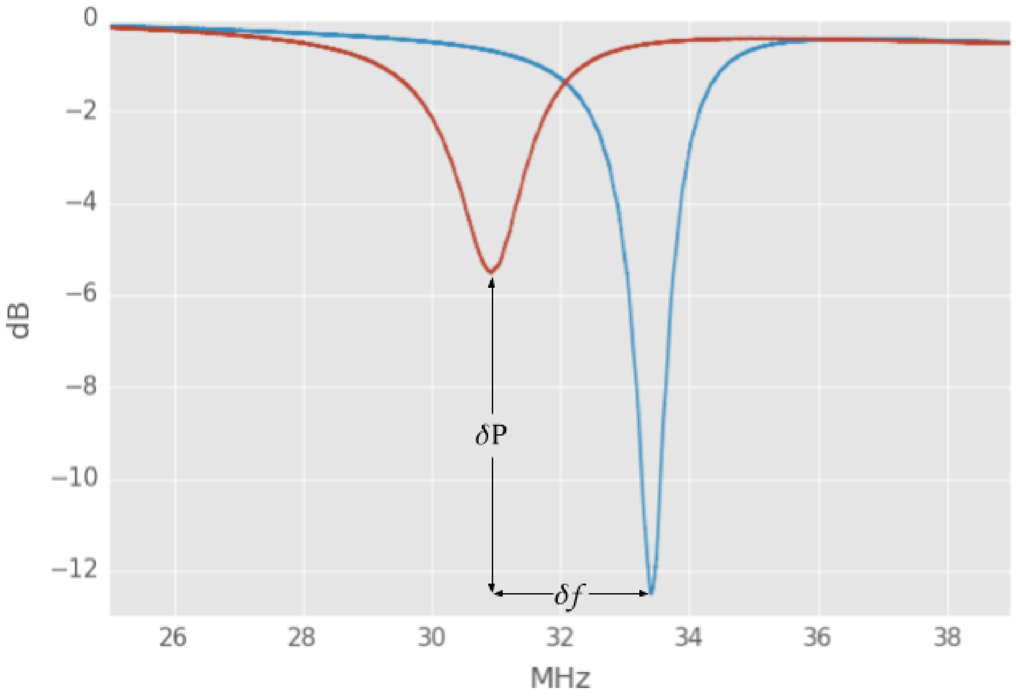

Figure 6: Measured response with respect to the transfer function S_{21} of a low frequency KID. The breaking of Cooper pairs due to absorbed photons causes a shift in the resonant frequency δf and the power level δP as represented by the S_{21} curves.

Kinetic Inductance Detectors (KID) have been developed and analyzed extensively (Mazin et al. 2001; Day et al. 2003; Mazin 2004; Doyle et al. 2008; Gao 2008). KIDs are based on a resonator mechanism that responds to a change in the population of Cooper pairs and quasiparticles in a superconducting material. Cooper pairs are electrons that experience zero DC resistance due to electron-phonon interaction in the material lattice (Cooper 1956). Quasiparticles are electrons of an effective mass that is different from the free-particle mass due to interactions with other particles in the material (Kaxiras 2003). The basic principle of KID operation is the detection of incident radiation by the breaking of Cooper pairs due to the energy of the absorbed photon flux. The kinetic inductance of the inductive component of the resonator changes as a function of the number density of Cooper pairs. Since the resonant frequency is a function of the inductance, it shifts as a function of absorbed power in the inductor. From this measurable shift in resonant frequency (Figure 6) the absorbed power of a KID can be determined.

Electrons form into Cooper pairs in superconducting material that is cooled below its critical temperature. These electrons are bound by an energy given by (Lynton 1962)

$$2\Delta_0 \sim 3.5 k_B T_C, \tag{1.35}$$

where Δ_0 is the binding energy at low temperatures, k_B is the Boltzmann constant, and T_C is the critical temperature. Breaking of these Cooper pairs by phonons or photons of energy $E > 2\Delta_0$ results in the formation of quasiparticles. It will be of importance in this dissertation to extract Δ_0 from experimental data and to determine the quasiparticle density as a function of temperature for a KID-style detector developed at Arizona State University (ASU).

Monitoring the number of quasiparticles in a superconducting film at a constant temperature gives insight into the power incident on the film. Breaking of the Cooper pairs by a single photon results in the creation of a quasiparticle density given by

$$n_{qp} \sim \frac{\eta h \nu}{\Delta_0}, \tag{1.36}$$

where η is the efficiency of quasiparticle formation from photon energy, h is the Planck constant, and ν is the frequency of the photon energy. When multiple photons are absorbed in steady-state the density of quasiparticles will change with respect to the total power absorbed within the quasiparticle lifetime given by (Mauskopf 2018)

$$dn_{qp} = \frac{\eta P_{abs} \tau_{qp}}{\Delta_0}, \tag{1.37}$$

where P_{abs} is the total power absorbed and τ_{qp} is the quasiparticle lifetime.

The main applications of KID-style detectors are in observational astronomy. Mazin incorporated KIDs as sensitive x-ray detectors (Mazin et al. 2006). Schlaerth showed that KIDs at the Caltech Submillimeter Observatory could be used to map objects such as Jupiter, Saturn, and G34.3 (Schlaerth et al. 2008). Baselmans describe the the use of KIDs for sub-mm astronomy (Baselmans et al. 2008). Vardulakis expands on the use of KIDs for sub-mm and x-ray imagining arrays for astrophysics (Vardulakis et al. 2008). Che provides a contemporary and comprehensive report on advancements in KID technologies for mm-wave astronomy (Che 2018).

1.2.6 Superconducting Nanowire Resonator Single Photon Detectors

In this dissertation, the characterization of a new type of nanowire device based on the KID principle is discussed. This detector will be referred to as a Superconducting Nanowire Resonator Single Photon Detector (SNRSPD). The primary difference between a KID and an SNRSPD is the implementation of an inductive component with dimensions on the order of nanometers instead of micrometers. SNSPD devices are readily available for implementation into resonant circuits and to subsequently create SNRSPD devices.

To operate an array of SNSPD devices with the traditional approach, each device needs to be wired individually from cryogenic temperatures to a room temperature environment. This increases system complexity and heat load on the coldplate and results in high power consumption. Implementing the SNSPD in a resonant circuit allows the multiplexing scheme already well-developed for KIDs to be used with SNRSPD devices. Since the capacitive portion of the resonant circuit is easily tuned, the resonant frequency of each SNRSPD pixel can be uniquely read out on the same feedline. Additionally, the SNRSPD can be tuned by varying the dimensions of the nanowire (A. J. Annunziata et al. 2010b). It is possible to bias the nanowires with RF-power instead of DC (Doerner et al. 2016). Doerner et al. have demonstrated a two-pixel proof-of-concept multiplexed SNSPD array biased with RF-power. The circuits used included one capacitor per pixel.

In this dissertation we will explore a SNRSPD circuit setup that includes an additional parallel capacitor modeled after the standard KID. First, we will present a two-pixel, proof-of-concept SNSPDR package with surface mount device (SMD) capacitors. We will characterize the SNRSPD response to changes in base temperature and to changes in bias current. From the results, we will obtain band-gap information and insight into the non-linear behavior of the kinetic inductance. We will calculate the density of states at the Fermi energy at zero temperature in order to obtain the quasiparticle number for each SNRSPD pixel. Additionally, we will present designs and a prototype for an imager array that consists of several pixels on a single chip that is biased by a single DC source.

Chapter 2

SCIENTIFIC MOTIVATION

This chapter is a an overview of four advanced applications that SNSPDs or SNRSPDs may be used for: intensity interferometry, the fast imaging of exoplanet signals, deep space optical communication, and quantum information. Intensity interferometry in particular is discussed at length due to concentration in this subject in the early years of the work done in the Astronomical Instrumental Lab at ASU for this dissertation.

2.1 Intensity Interferometry

An immediate application of SNSPDs is intensity interferometry. Stars are incoherent (thermal) sources of light that radiate over a wide range of frequencies. Correlations in the intensity of filtered thermal radiation can be measured within a coherence time that is determined by the central wavelength and bandwidth of the filtered light by correlating signals from two or more detectors observing the same source. Moreover, the amplitude of this second order correlation function is a function of spatial separation between detectors and depends on the angular size of the source.

Measurements of diameters of stars using this technique, called intensity interferometry, were first accomplished by Hanbury Brown and Twiss (HBT) (Hanbury Brown 1956) as they were able to accurately determine the diameter of Sirius using photomultiplier tubes to detect the fluctuations in intensity of the starlight. Our motivation for the reinvestigation of this measurement technique is the advent of

SNSPD technology. The speed of these detectors allow for the measurement of more compact and dimmer objects than previously possible.

In this section, we describe the experimental setup required for measurements of intensity correlations from laboratory sources and for measuring diameters of bright stars with small-to-moderate sized telescopes using SNSPDs. With a sensitive detector, the raw signal that is measured is a superposition of signals from multiple sources across a given area containing the object from which the signal is desired. This skews the desired result. Therefore, intensity interferometry is used to isolate the correlated light from the desired source. This is done through the use of (at least) two separated detectors measuring light from the source at the same time.

2.1.1 Correlation Function

The correlation function is an nth-order function that relates the electromagnetic field at multiple spacetime points. The first-order correlation function is given by

$$C_{(1)}(r_1 t_1, r_2 t_2) = \langle E^*(r_1 t_1) E(r_2 t_2) \rangle \,, \tag{2.1}$$

where E is the electric field and rt represents the position in space and time of the detectors. For $r_1 = r_2$ and $t_1 = t_2$, $C_{(1)}$ is simply the intensity of the field. For $r_1 = r_2$ and $t_1 \neq t_2$, $C_{(1)}$ is a time-dependent intensity; if the intensity varies in time, it can be measured. For $r_1 \neq r_2$ and $t_1 = t_2$, $C_{(1)}$ is a spatially-dependent intensity; if the intensity varies with distance across the wavefront, it an be measured.

The second-order correlation function is measured by correlating the intensity of the radiation field emitted by a source at two different detectors separated in space and time. Coherent radiation exhibits random intensity fluctuations due to the stochastic nature of the arrival and detection time of the photons that are uncorrelated between any two detectors measuring the same source. However, incoherent light exhibits additional intensity fluctuations corresponding to photon bunching that are correlated at some level between detectors.

The second-order correlation function is given as (Foellmi 2009)

$$C_{(2)}(r_1t_1, r_2t_2) = \langle I(r_1t_1)I(r_2t_2)\rangle\,, \tag{2.2}$$

where I is the intensity of the electric field at the detectors. For $r_1 \neq r_2$ and $t_1 = t_2$, $C_{(2)}$ provides a spatially-dependent measurement of the wavefront state; if the distribution of photons vary with distance across the wavefront, it can be measured. This is the key to measuring the coherence pockets in the radiation field from the source and to performing the HBT experiment.

The signal-to-noise ratio (SNR) for detecting second-order intensity fluctuations from an incoherent light source is given by

$$\frac{S}{N} = \epsilon n_{occ} N_{modes} \sqrt{\frac{\tau_{int}}{\tau_{det}}} C_{(2)}(r_1t_1, r_2t_2), \tag{2.3}$$

where ϵ is the overall efficiency of the system, n_{occ} is the occupation number of a single radiation mode, N_{modes} is the number of expected modes, τ_{int} is the integration time, τ_{det} is the detector time constant, and $C_{(2)}(r_1t_1, r_2t_2)$ is the normalized second-order correlation function as discussed previously. Modern PMTs have time constants on the order of 300ps. SNSPDs have time constants on the order of 10ps. This corresponds to over a factor of 5 increase in signal-to-noise. See Appendix VII for a derivation of the SNR.

$C_{(2)}(r_1t_1, r_2t_2)$ is experimentally obtained by varying the distance between the two detectors. The maximum separation between detectors, or baseline, where spatial correlations can be detected is given approximately by the Rayleigh criterion (Rayleigh

1879):

$$\sin\theta = \frac{1.22\lambda}{d}, \tag{2.4}$$

where θ is the angular size of the source, λ is the central wavelength of the observed bandwidth of light, and d is the baseline.

The baselines required to determine stellar diameters are on the order of a kilometer (Dravins, Lagadec, and Nuñez 2015). Intensity interferometry has advantages for large baselines compared to conventional phase interferometry. Phase interferometry requires the light from multiple telescopes observing the same source to be physically combined so that an interference pattern is formed and can be analyzed while maintaining phase coherence. Fluctuations in the path lengths between telescopes and through the atmosphere limit the duration of a fixed fringe pattern and therefore the detectable source magnitude. This is not a problem for lab experiments taking advantage of sources with a large angular size and the corresponding small required variations of the baseline. For stars, which have small angular sizes, the baselines are too large for this conventional setup to work without significant difficulty. The attenuation alone from the large distances of fiber optics required to combine the beams is enough to derail any attempts to accurately measure stellar diameters.

For intensity interferometry, instead of the physical recombination of the beams, the time streams from two detectors corresponding to the arrival times of photons can be stored digitally. In post-processing, the two steams can be combined and correlations can be determined. Therefore, in principle, a baseline of any size can be used for intensity interferometry measurements.

By increasing the distances over which correlated beams of light can be analyzed, incoherent light sources with small angular diameters can be measured. In addition to typical stellar objects such as Sirius, other extra-solar objects may be considered for measurement such as neutron stars and perhaps even exoplanets. Since there is no loss in signal by adding additional baselines in intensity interferometry, a large array of commercially available telescopes with a combined area equal to or greater than existing large telescopes may be used.

2.1.2 SNSPD Packaging

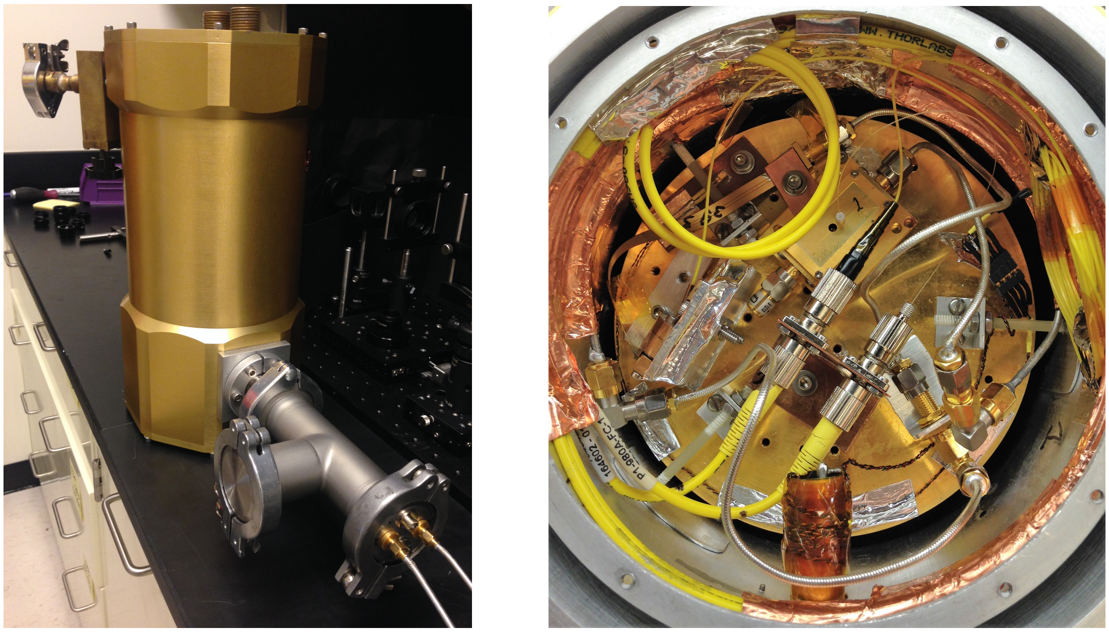
(a) (b)

Figure 7: (a) Liquid helium Infrared Laboratories, Inc. HD-3 cryogenic dewar. (b) Setup inside of the dewar with a single-mode fiber optic cable attached to the cover of the device package via a bare ferrule situated in a low tolerance guiding circular bore. The position of the ferrule was carefully determined via measurements made of the position of the nanowires under a high-magnification microscope. The single-mode fiber connected to the SCONTEL device was directed coupled to the nanowire with adhesive before shipment to ASU.

We mounted two SNSPDs in a small liquid helium Infrared Laboratories, Inc. HD-3 cryogenic dewar coupled to single mode fiber optic cables which pass through a hermetic feed-through built in-house (Figure 7). The detectors were read out with microwave amplifiers and FPGA-based coincidence electronics.

The SNSPDs used in this experiment were from two different collaborators. The first SNSPD was obtained from Cardiff University and was fabricated by SCONTEL. This device was pre-packaged and fiber-coupled. We characterized the nanowire at ASU where we determined the critical temperature to be 9.65K. The second device was fabricated at the Massachusetts Institute of Technology. This device was packaged and coupled to fiber optics at ASU.

We modified an existing package primarily used for low noise amplifiers. We had a pocket milled in the bottom of the package to mount the chip. We also had a cover made with alignment pin-holes and holes for the fiber optic ferrule to rest in above the detector. Due to imperfections in this process, the ferrule-hole was not aligned with the detector. We aligned the ferrule-hole above the detector by hand with an optical microscope and were able to place the center of the hole to within $\pm 30\mu$m of the detector.

The fiber used to couple to the MIT detector was made in-house with materials from ThorLabs, Inc. (Figure 8b). On the detector side, a bare ferrule was inserted with single-mode fiber and polished. The other side was fitted with an FC-connector in order to be coupled with an FC-FC connector to a matching single-mode fiber through a hermetic feedthrough also made at ASU (Figure 8a). The feedthrough contains four D-shaped holes with o-ring grooves extruded from a stainless steel NW-40 vacuum flange.

Based on the uncertainty in alignment, we calculated the expected efficiency as a function of vertical separation between the fiber and the nanowire. The percentage of light falling on a detector can be approximated by

$$\% = \left(\frac{d_{\text{snspd}}}{d_{\text{spot}}}\right)^2 = \left(\frac{d_{\text{snspd}}}{2 * z * tan(arcsin(NA))}\right)^2, \tag{2.5}$$

where d_{snspd} is the diameter of the detector, d_{spot} is the diameter of the spot of light incident on the detector chip, z is the ferrule-to-chip vertical displacement, and NA is the numerical aperture of the fiber optic cable. Given the numerical aperture of our single-mode fiber NA $= 0.13$, a vertical distance of 300μm between the ferrule and the detector chip yields a spot size of diameter 78.7μm compared to the detector diameter of 15.0μm and we arrive at $\% = 2.63$.

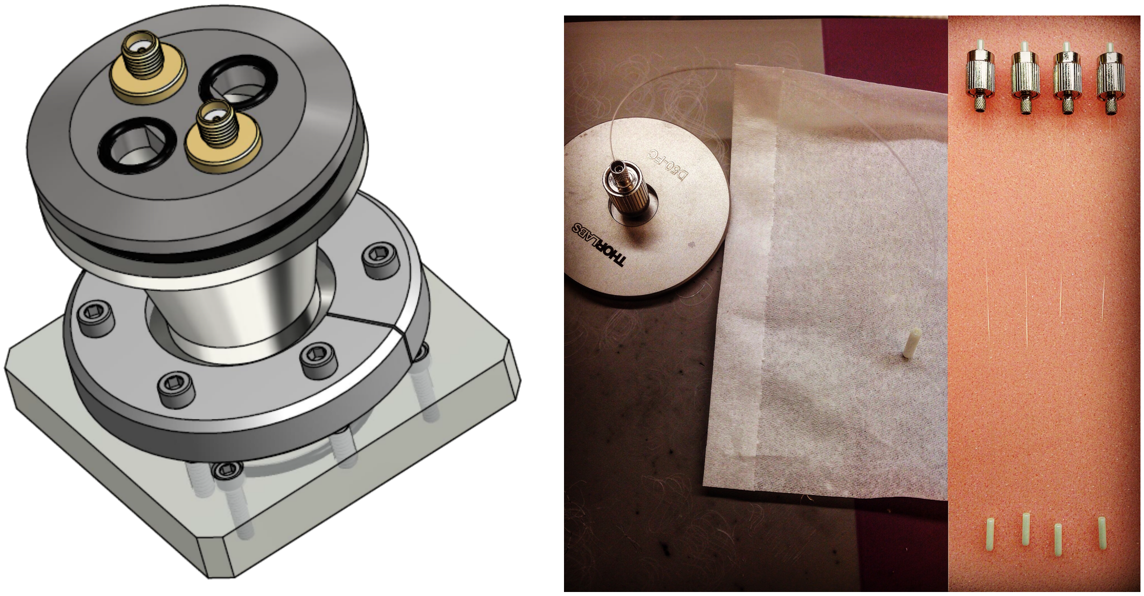

(a) (b)

Figure 8: (a) NW-40 vacuum flange designed in Autodesk Inventor with two SMA input/output ports and two fiber optic input/output ports that lead to the two detectors. (b) Single-mode fiber optic cables assembled for the photon counting experiment.

2.1.3 Lab Setup

2.1.3.1 Optical Setup

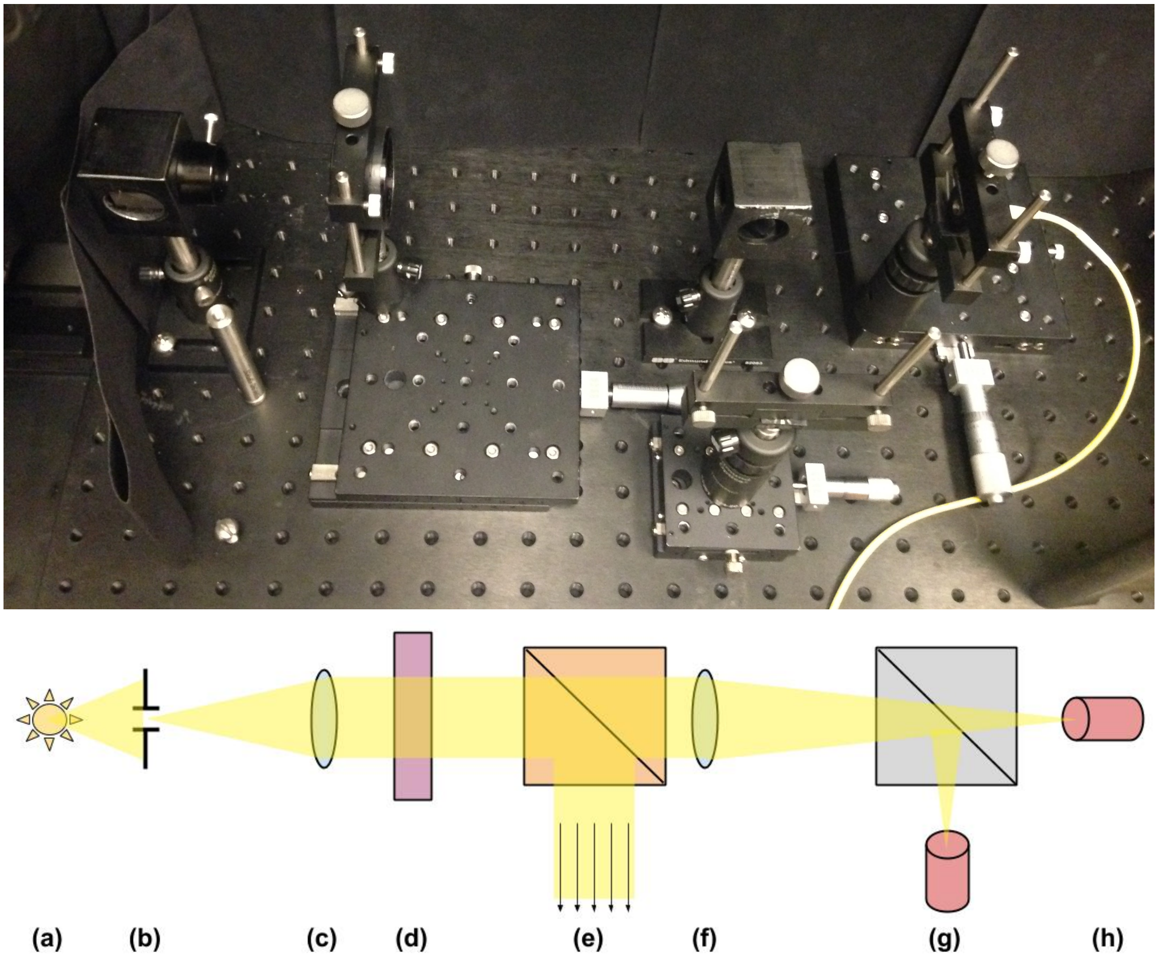

Figure 9: (a) Thermal light source (b) 12.5μm pinhole (c) 2.5cm lens (d) narrow band filter (e) polarizing beam splitter (f) 2.5cm lens (g) beam splitter and detector channel 1 (h) detector channel 2. A portion of the optical setup is shown above the diagram. From left to right: polarizing beam splitter with filter, focusing lens, beam slitter and two stages to house the optical cables coupled to the detectors. The focusing lens is on a stage which allows for z-axis (depth) control. Both fibers are on up-down (y-axis) and left-right (x-axis) stages, giving three degrees of freedom for alignment.

In the original HBT lab experiment, photomultiplier tubes were used as photon detectors. A stream of incoherent photons was generated by a mercury arc lamp. This source was chosen because it contained an emission line that corresponded to the high-efficiency region of the photomultiplier tubes and had a bandwidth of 10pm. This bandwidth resulted in a coherence time that was smaller than the timing accuracy of the detectors, which allowed them to probe the intensity fluctuations of the source. If the coherence time was larger than the timing accuracy that the detectors can resolve a photon event, then the fluctuations would not be resolved because the light collected at the detectors would not necessarily be light contained in the same coherence packet and therefore much of the light collected would be uncorrelated.

At ASU, an optical table setup was fashioned to allow us to detect spatial intensity correlations with a laboratory thermal source. Our artificial star consisted of a 12.5μm pinhole illuminated by a $\simeq$2100K incandescent lamp. A 2.5cm diameter lens was placed at its focal length of $\sim$40cm from the pinhole in order to collimate the light which was then passed through a narrow band filter. Collimation of the light beam is necessary for efficient operation of the filter. From here, the collimated beam was fed through a 50/50 polarizer as differing polarizations are uncorrelated. Now that the beam has some bandwidth $\Delta\nu$ and is polarized, the light was passed through an additional 2.5cm lens with a $\sim$30cm focal length for refocusing into the two detector receptacles via a 50/50 beam splitter. The beam is fed into two single-mode fibers with an active area of 10μm.

2.1.3.2 Readout

The electronic pulses from both detectors must be amplified before entering the readout electronics. The SNSPDs require a relatively high frequency microwave readout chain with low phase noise (timing jitter) components. This microwave readout chain consists of a low noise current source which is low-pass filtered to the DC port of a Mini-Circuits bias-tee (ZFBT-4R2G+). The AC+DC port biases the nanowires and the AC output port is amplified with two Mini-Circuits amplifiers (ZKL-1R5+). To reduce the risk of standing waves forming in the AC output chain, an attenuator is added before and after the first amplifier. This chain is successful in producing 1.5V pulses which are capable of being read by the timing electronics.

2.1.4 Lab Results

We measured the efficiency for the setup with the SCONTEL SNSPD compared to measurements and efficiency curves for a 4-channel single photon avalanche diode (SPAD) from Excelitas (SPCM-AQ4C). The SPCM-AQ4C was used in an optical setup that contained a 1000nm filter with a 10nm bandwidth and a single mode fiber. With this illumination the photon count rate for the SPAD was approximately 50kHz. The same setup was used and coupled to the SCONTEL SNSPD. For the same optical setup, the photon count rate in the SNSPD was approximately 8.6kHz. The number of detected photons can be expressed by

$$N = \gamma \epsilon_{SPAD}, \tag{2.6}$$

where γ is the number of photons incident on the detector and ϵ_{SPAD} is the efficiency of the SPAD. Given that the efficiency of the SPAD at 1000nm is approximately 10%, the efficiency of the SNSPD is then found to be $\epsilon_{SNSPD} = 1.7\%$ at 1000nm.

2.1.5 Existing Optical Telescopes

A key motivation for this experiment is the pre-existence of suitable telescopes. Commercially available telescopes in the 8-20 inch range can be used. In addition to convenience, this is useful because the more telescopes that are integrated into the system, the more baselines there are to construct. The signal-to-noise scales as the square root of the number of baselines.

Medium and large optical telescopes arrays are also available to the scientific community. For example, Kitt Peak National Observatory in Arizona has many suitable telescopes that can provide baselines up to 650 meters (Pilyavsky et al. 2017). On November 2, 2016, we measured a 1MHz photon count rate from Capella ($m = +0.08$) at the Bok 2.3m telescope with an SNSPD device (Figure 10).

2.1.6 Magnitude Limits Achievable

The number of photons per second per Hertz from a selected source of magnitude M can be found via the following equation:

$$\Gamma_\gamma = 0.05\lambda f_0 2.512^{\Delta m} A, \tag{2.7}$$

where λ is the observed central wavelength, f_0 is the calibrated flux (in Jy) at a given λ of an $m = 0$ star (Bessell 1979; Schneider, Gunn, and Hoessel 1983; Campins, Reike, and Lebofsky 1984), Δm is the change in magnitude of the star from $m = 0$, and A is

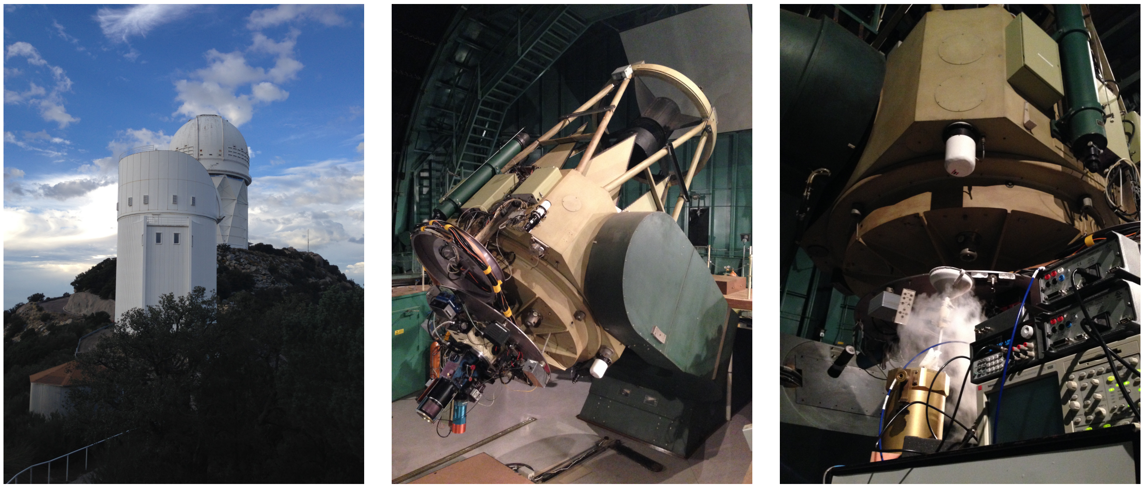
(a) (b) (c)

Figure 10: (a) The Bok dome (foreground) on Kitt Peak. (b) The Bok telescope. (c) The cryogenic system coupled to the Bok telescope.

the collecting area of the telescope. The signal-to-noise ratio is then related to the magnitude of the target by

$$\frac{S}{N} = \epsilon 0.05\lambda f_0 2.512^{\Delta m} A\sqrt{\frac{\tau_{int}}{\tau_{det}}}, \tag{2.8}$$

where ϵ is the system efficiency, τ_{int} is the integration time, and τ_{det} is the detector time constant.

Table 3 shows the achievable magnitudes based on a zero-point measurement with $S/N = 10$ and for different values of the parameters λ, telescope diameter d_{tele}, and detector time constant τ_{det}. τ_{det} is taken to be the achievable timing resolutions from SPADs and SNSPDs. τ_{int} was taken to be the course of a single night, or 8 hours. An overall system efficiency of 5% was assumed.

Table 3: Limiting magnitudes of stars for which zero-point correlation is achievable in 8 hours with 5% system efficiency. The calibration flux (f_0) was obtained from the Gemini Observatory magnitudes-to-flux calculator.

Observation Wavelength (nm)	Calibration Flux (Jy)	Telescope Diameter (m)	Detector Resolution (ps)	Apparent Magnitude Limit
671	2841	0.36	500	Sirius (m_R)
671	2841	4.0	500	4.1 (m_R)
1150	1725	0.36	60	0.1 (m_J)
1150	1725	4.0	60	5.3 (m_J)

2.1.7 Science Targets

Once the system is optimized and intensity correlations are measured in the lab, the optical setup can be coupled to telescopes and stellar diameters will be measured. When this is accomplished, intensity interferometry will have been reinstated as a viable science tool with single photon detector technology.

The timing accuracy of SNSPDs and therefore increased signal-to-noise ratio will have opened the door to the measurement of stellar diameters to a higher precision than ever before. Perhaps even stellar feature resolution such as star spots will be possible. The lower magnitude measurement possibilities may also allow for the detection of more exotic objects such as exoplanets. Other interesting science targets include measuring the precise rotation periods of neutron stars, the behavior of binary objects such as a black hole accretion disk and an OB star (Cygnus X-1), and tests of quantum gravity.

2.2 Other Applications

2.2.1 Fast Imaging of Exoplanet Signals

There have been many methods developed in order to image exoplanets. Angular differential imaging (ADI) is a technique that involves the reduction of speckle noise from a slowly evolving imaging plane in order to detect companion bodies in the proximity of a highly luminous star (Marois et al. 2006; Bottom, Ruane, and Mawet 2017). Raw images from a telescope configured to stay aligned with the instrumentation and images created from a reference point-spread function (PSF) are rotated and combined to resolve the exoplanet. Locally optimized combination of images (LOCI) is a technique that dispenses with PSF processing to subtract starlight from an image (Lafrenière et al. 2007). Instead, the reference frame is constructed using a linear combination of library reference images to produce an improvement in effective contrast. Reference star differential imaging (RSDI) singles out a target by subtracting a compilation of images taken at different times with respect to a reference star (Marois et al. 2005). Non-redundant aperture masking interferometry (NRM) is a technique that combines the views of N-telescopes with pupils obstructed by a non-redundant mask to produce a single image (Baldwin et al. 1986; Haniff et al. 1987).

Several exoplanets of been directly imaged. 2M1207b (Figure 11a) was the first and was imaged at the Very Large Telescope (VLT) in 2004 using adaptive optics infrared wavefront sensing (Chauvin et al. 2004). It is a gas giant that is five times more massive than Jupiter. 2M1207b orbits the brown dwarf 2M1207 and its distance form Earth is approximately 170 light years (Mamajek 2005). Fomalhaut b (Dagon) was directly imaged in 2008 using RSDI (Kalas et al. 2008). Dagon (Figure 11b) is approximately 7.7 parsecs from Earth and was the first exoplanet to be predicted to exist before discovery (Quillen 2006). The prediction was made based on the eccentricity and sharpness of the disc surrounding the star being caused by a revolving planet near the edge of the disc.

Using SPDs for the fast imaging of exoplanet signals could dramatically improve the signal-to-noise ratio of direct images. Due to the low photon flux of exoplanets, it has been suggested that a 256×256 array of APDs be used for NASA exoplanet missions with $> 10^6$ photons/s/pixel (Figer, Lee, et al. 2011). Additionally, sensitivity is maximized due to the elimination of read noise inherent to CMOS and CCD sensors (Figer, Aull, et al. 2011). One challenge to this approach is the presence of after-pulsing in APD devices. It has been suggested that the Wide-Field Infrared Survey Telescope (WFIRST) use APDs for exoplanet detection (Kolb and Figer 2015). An SNSPD camera with high maximum count rates and low timing jitter is proposed to capture rapidly moving exoplanets (McCaughan 2017). SNSPDs are preferable when compared to APDs due to having little-to-no after-pulsing probability and a shorter dead time. Additionally, exoplanets emit thermal radiation in the near-infrared (NIR). This band eliminates the problem of small angular separation because thermal emission is independent from the separation between the star and the exoplanet to be imaged. NIR is the frequency range that the SPDs presented in this dissertation are most efficient.

Lumped element kinetic inductance detectors (LEKID) have been extensively developed (Doyle 2008). An interesting investigation involving LEKID technology that would allow for the characterization of exoplanets is being carried out (Dzifa Akua Parrianen et al. 2018). It is suggested that spectroscopy can be preformed on exoplanet signals with energy-resolving LEKIDs. This would eliminate the need for

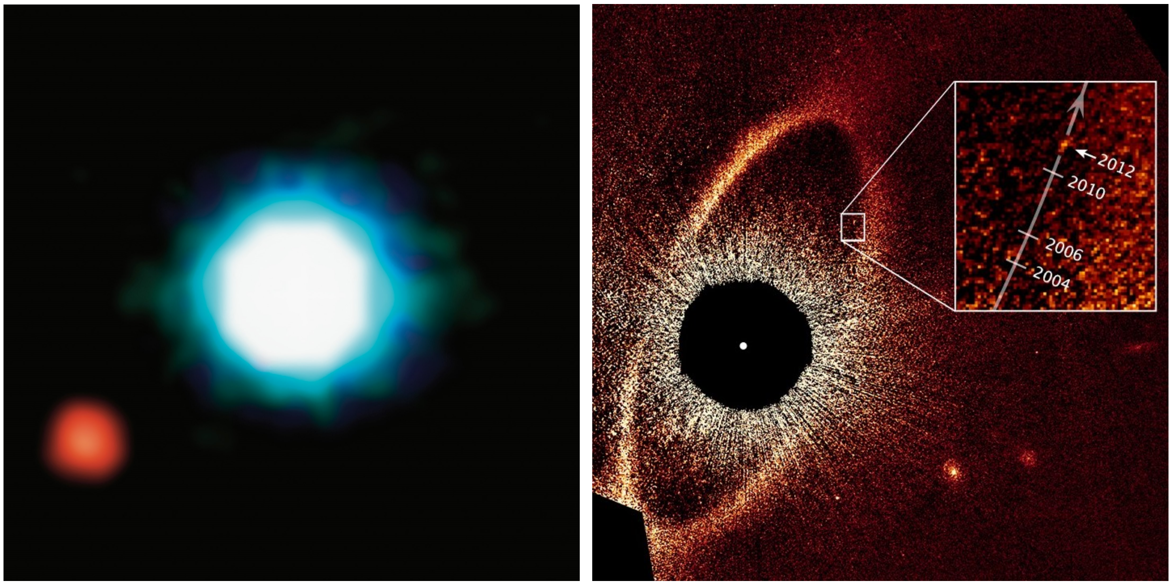

(a) (b)

Figure 11: (a) 2M1207b (Image Credit: European Southern Observatory) (b) Dagon (Image Credit: National Aeronautics and Space Administration)

additional optical components such as diffraction gratings to separate the incident spectrum and would lower the total number of detectors required for the instrument to operate.

2.2.2 Deep Space Optical Communication

RF/microwave signals have traditionally been used to transmit information to and from satellites. Radio waves in the HF- and VHF-band were used to receive signals from humanities first satellite, Sputnik 1, launched in 1957 by the Soviet Union. The United States responded with Explorer 1 in 1958. The Ka-band and X-band ranges of the electromagnetic spectrum were used for the first deep space network involving spacecraft (Smith 1985; Dickinson 1985).

Deep space optical communication (DSOC) is essential for the success of future satellite missions. The capability to use optical lasers for DSOC was first demonstrated in 1993 (Wilson, Lesh, and Yan 1993). Beams from two Earth-based lasers were detected from a distance of 6-million kilometers by the CCD on board the Galileo satellite. An infrared laser was used to communicate with the Messenger satellite at a distance of 24-million kilometers in 2005 (Neumann et al. 2008).

In 2022, the Psyche orbiter will launch to study a unique metallic asteroid (16 Psyche) that is approximately 348-million kilometers from Earth (Elkins-Tanton et al. 2014). It is possible that 16 Psyche is the remnant core of a failed protoplanet. To achieve efficient communication with the Psyche orbiter at ranges up to and over 2AU, high-efficiency photon counting detector arrays will be required in order to differentiate between the weak signal and background noise. The ground based receiver will implement tungsten silicide (WSi) SNSPD arrays to detect 1550nm laser signals from the orbiter (Biswas et al. 2018).

2.2.3 Quantum Information

Quantum information is a field that is rapidly coming to the forefront of industrial pursuit after decades of academic inquiry. As technology has advanced, it is natural that the quantum limit is sought in applications such as communication and computing. Quantum key distribution (QKD) is of particular interest with respect to single photon detector technology.

Circa 1970, the idea that set in motion the groundwork for what would become QKD was presented by Stephen Wiesner. What Wiesner proposed was a multiplexed quantum messaging system that allowed for the transmission of two messages to a receiver (Wiesner 1983). The receiver would have the ability to choose which message to read with the consequence that the other message would be destroyed due to the properties of quantum mechanics.

In addition to this quantum multiplexing, Wiesner also proposed using quantum mechanics to produce secure currency (Lo, Popescu, and Spiller 2002). The mechanism that drives the security is a sequence of two-state quantum systems each in either one predefined basis or another. Someone trying to forge the banknote would be likely to disrupt the state without knowing with respect to which basis to measure each member of the sequence. If even one state is measured in the wrong basis, then the forged banknote will have an incorrect sequence. Assuming knowledge of the bases and a sequence of N required measurements, the probability of guessing all of the correct bases and thereby recreating the banknote with the proper states is $P = (3/4)^N$.

QKD is a form of communication that invokes quantum mechanics in order to provide security for the sender and the intended receiver. Additionally, it is possible to detect the presence of intrusion on the message. The mechanism by which this works is the production of a randomized key by the sender and receiver in order to provide a tool for encryption and decryption of the messages. If the undesired third party attempts to measure the quantum key, the key will depart from its original form in a detectable way. QKD became a serious consideration of the academic community upon the advent of the BB84 protocol in 1984 in which the polarization states of photons were the suggested two-state quantum systems to be used for this application (Bennett and Brassard 1984). Moreover, BB84 was a prepare-and-measure-based protocol. In 1991, the E91 protocol provided an alternative to BB84. In this version of QKD, quantum entanglement is utilized in order to secure messages (Ekert 1991). The intended sender and receiver share an entangled pair of objects. The intruder on the message will alter the system by intercepting one of the objects.

Since QKD is mostly done at a single photon level, loss is the primary limitation in achieving a long-distance reception of a secure message. SNSPD devices play a crucial role in achieving a secure transmission distance of 100km or longer (Baek et al. 2009). Additionally, since the devices discussed in this dissertation are highly sensitive at 1550nm, SNSPDs are a clear choice for QKD in optical fibers. 1550nm is also the wavelength at which losses in optical fibers are the lowest (Gisin et al. 2002). Many academic groups have performed QKD experiments with SPDs at and over 100km (Chen et al. 2013; Takemoto et al. 2015; Tretyakov et al. 2016).

Another application for SNRSPDs is quantum computing and in particular linear optics quantum computation (LOQC). LOQC was first realized in 1999 and is a variation of quantum computing that takes advantage of photons as information carriers (Adami and Cerf 1999). Linear optical elements are used to manipulate the photons and SPDs are used to detect processed photons (Knill, Laflamme, and Milburn 2001). LOQC is an active area of research in the field and is being developed by many groups in order to provide realistic system performance (Pittman, Jacobs, and Franson 2004; Kok et al. 2007; Jennewein, Barbieri, and White 2011). In order to make LOQC practical, nanophotonics is being developed to miniaturize the required linear optical components (Goban et al. 2014).

The ability to encode bits of information on a single photon is clearly of importance to these applications. The obvious way to do this is with polarization encoding as previously discussed. Encoding can also be done with respect to momentum states. In 2002, the ability to encode two bits of information on a single photon via the sorting of four orbital angular momentum states was demonstrated (Leach et al. 2002). A decade later, using a mode transformer method to convert orbital angular momentum states to transverse momentum states, 3.46 bits of information per photon was encoded

(Lavery et al. 2012). Recently, up to 10.5 bits have been attributed to a single photon with a strategy that involves a grid of symbols (Tentrup et al. 2017). A photon that is incident on a particular symbol encodes information with respect to that symbol. Time-bin encoding of bits is a technique that involves a single photon taking one of two possible paths of differing lengths. The path taken determines the state. For this type of analysis, SNSPDs are ideal detectors due to their inherent free-running operation and superior dead time performance (Valivarthi et al. 2014).

Chapter 3

SUPERCONDUCTIVITY THEORY

This chapter is a review of the fundamentals of superconductivity theory and the physics of superconducting films. We discuss the carriers of the superconducting current and the theory that describes their behavior. We discuss important parameters of superconducting films including quasiparticle number, conductivity, and surface impedance.

3.1 Fundamentals of Superconductivity Theory

3.1.1 Cooper Pairs and the Bardeen–Cooper–Schrieffer Theory

Bardeen–Cooper–Schrieffer (BCS) theory is a microscopic theory of superconductivity that describes the phenomenon in terms of the net attractive potential between electrons that are inherently repulsive toward each other via the Coulomb force (Bardeen, Cooper, and Schrieffer 1957a, 1957b). These electrons are known as Cooper pairs. Cooper pairs conduct without dissipation via electron-phonon interactions within the material lattice. These interactions cause the paired electrons to bypass the Pauli exclusion principle and act as an effective bosonic particle (with integer spin). In turn, this allows for the overlap of electron pairs and the formation of a condensed state. This state is maintained at low temperatures because the thermal energy is less than the energy barrier of the super-fluid. This interaction results in zero resistance at DC. The coupling of these electrons into pairs takes place on the order of a few hundred nanometers, which is greater than the crystalline lattice structure spacing in the metal (Rohlf 1994).

BCS theory is particularly useful because it provides a formulation for the temperature dependent gap energy of superconductors and the coherence length. The attraction between the electrons is a ground state energy on the order of milli-electron volts (meV). This is called the binding energy and is given by (Tinkham 1996)

$$\Delta(T) \approx 1.764 k_B T_C \sqrt{1-(T/T_C)}, \tag{3.1}$$

where $\Delta(T)$ changes slowly at low temperatures but increases as $T \rightarrow T_C$. T_C is the critical temperature of the superconducting material set by the material composition. When $T \rightarrow 0$, we recover the zero-point binding energy Δ_0 given by Equation 1.35.

The coherence length for a pure superconducting metal ξ_0 is on the order of the minimum size of a Cooper pair as prescribed by the Heisenberg uncertainty principle (Pippard 1953). In terms of the zero-point binding energy and the Fermi velocity v_F, this coherence length is given by (Annett 2004)

$$\xi_0 = \frac{\hbar v_F}{\pi \Delta_0}. \tag{3.2}$$

For pure niobium, $\xi_0 \approx 39$nm (Finnemore, Stromberg, and Swenson 1966; Buckel 1991).

3.1.2 The Two-Fluid Model

The behavior of a superconducting material in a time varying electromagnetic field can be described with the two-fluid model (Bardeen 1958). There exist two groups of charge carriers that constitute the two paths through which current can flow in a superconductor: non-dissipative Cooper pairs and normal-conducting quasiparticles.

Cooper pairs behave in a manner that causes current to move with zero resistance at DC and quasiparticles behave as electrons in a normal metal.

The total density of charge carriers in a superconducting material can be expressed as

$$n = n_{cp} + n_{qp}, \tag{3.3}$$

where n_{cp} is the density of the Cooper pairs and n_{qp} is the density of the quasiparticles. This is a conserved quantity, but the populations of the Cooper pairs and quasiparticles can change with respect to each other. The ratio of Cooper pairs to quasiparticles depends on the proximity of the base temperature to the critical temperature. At $T = 0$, $n = n_{cp}$ such that all of the charge carriers in the material constitute the super-fluid. As $T \rightarrow T_C$, the number of quasiparticles increases as the number of Cooper pairs decreases. At $T > T_C$, $n = n_{qp}$ such that all of the charge carriers in the material constitute normal electrons. The relationship between n_{qp} and n_{cp} with respect to temperature can be expressed as follows:

$$\frac{n_{cp}}{n_{cp} + n_{qp}} = 1 - \left(\frac{T}{T_C}\right)^4. \tag{3.4}$$

An experimental determination of n_{qp} as a function of temperature for NbN nanowires is carried out in Chapter 5.

3.1.3 The London Equations and Penetration Depth

The London equations are a set of equations that describe the relationships between the electric field, the magnetic field, and the superconducting current in a material. The relationship between the superconducting current density with the electric field in a material can be obtained by substituting the superconducting current density into the equation of motion for Cooper pairs.

The superconducting current density is given as

$$\vec{i}_{cp} = -n_{cp} e \vec{v}_{cp}, \tag{3.5}$$

where n_{cp} is the Cooper pair number density, e is the elementary charge, and $\vec{v}_{cp}$ is the Cooper pair group velocity. The equation of motion for Cooper pairs in an electric field is given as

$$n_{cp} m_e \frac{dv_{cp}}{dt} = -n_{cp} e \vec{E}, \tag{3.6}$$

where m_e is the mass of an electron, and $\vec{E}$ is the electric field. We then arrive at

$$\frac{d\vec{i}_{cp}}{dt} = \frac{e^2 n_{cp}}{m_e} \vec{E}, \tag{3.7}$$

which is the first London equation.

The second London equation is a the relationship between the superconducting current density and the magnetic field. Moreover, the application of Ampère's law to this equation reveals the nature of the material with respect to the penetration depth of the magnetic field.

Ampère's law is given as

$$\vec{\nabla} \times \vec{H} = \vec{i}_{cp}, \tag{3.8}$$

and the second London equation is given as

$$\vec{\nabla} \times \vec{i}_{cp} = -\frac{e^2 n_{cp}}{m_e} \vec{H}, \tag{3.9}$$

where $\vec{H}$ is the magnetic field in the material. Substituting Ampère's law into the second London equation results in

$$\nabla^2 \vec{H} = \frac{\vec{H}}{\lambda_L^2}, \tag{3.10}$$

where λ_L the London penetration depth of the magnetic field in the material. The magnetic field will decay exponentially to a point within the material with respect to this parameter of the material. This is know was the Meissner effect.

The London penetration depth can be written more explicitly as

$$\lambda_L = \sqrt{\frac{m_e}{\mu_0 n_{cp} e^2}}, \tag{3.11}$$

where it is evident that since there is a dependence on the Cooper pair density, there must be a dependence of the penetration depth on temperature. Moreover,

$$\lambda_L(T) = \frac{\lambda_{L,0}}{\sqrt{1-(T/T_C)^4}}, \tag{3.12}$$

where $\lambda_{L,0}$ is the penetration depth at $T = 0$ and T_C is the critical temperature of the material. For pure niobium, $\lambda_L \approx 39$nm (Van Duzer and Turner 1981).

3.2 Physics of Superconducting Films

3.2.1 Density of States and Quasiparticle Number Density

The density of states at the Fermi level N_0 is the number of possible states of electrons at zero temperature per energy level per volume. In a superconductor, a band-gap forms around the Fermi level with width 2Δ where all of the electrons that would have occupied that energy band are available to form Cooper pairs. The number of electrons that can form Cooper pairs is given approximately by $N \approx 2\Delta N_0 V$, where V is the volume of the material.

The number density of quasi-particles can be found with (Rohlf 1994)

$$n_{qp}(T) = 4\int_{\Delta}^{\infty} \frac{N(E)E}{\sqrt{E^2-\Delta^2}} f(E)dE \tag{3.13}$$

where E is the possible energy states of the quasiparticles and $E/\sqrt{E^2-\Delta^2}$ modifies the single-spin density of states $N(E)$ to include only the states that the quasiparticles can occupy. $f(E)$ is given as (Fermi 1926; Dirac 1926)

$$f(E) = \frac{1}{1+e^{E/k_B T}}, \tag{3.14}$$

which is the Fermi-Dirac distribution that represents the probability that a particular energy state will be occupied.

Assuming that thermal quasiparticles dominate the total number of quasiparticles in the nanowire in the absence of incident radiation and for $k_BT \ll \Delta$ and $\hbar\omega \ll \Delta$, the number density of quasiparticles as a function of temperature is given as (Mauskopf 2018)

$$n_{qp}(T) \cong 2N_0\sqrt{2\pi k_BT\Delta_0}e^{-\Delta/k_BT}, \tag{3.15}$$

for low temperatures ($T \ll T_C$). The number of quasiparticles is dependent on the density of states at the Fermi energy.

At the critical temperature, when all of the charge carriers are in the form of quasiparticles,

$$n_{qp}(T = T_C) = 4N_0\int_0^\infty \frac{dE}{1+e^{E/k_BT_C}} = 4N_0k_BT_C\ln(2), \tag{3.16}$$

where this population of particles is available for Cooper pair production should the temperature drop below the critical temperature.

3.2.2 The Drude Model of Conductivity

In order to discuss the dynamics of superconducting films, the conductivity of materials must be understood. How current responds to a change in voltage is described by the conductivity of the material:

$$\vec{i} = \sigma_0\vec{E}, \tag{3.17}$$

where σ_0 is the conductivity of the material at DC and $\vec{E}$ is the electric field. As discussed previously, $\vec{i} = en_e\vec{v}$, such that we arrive at

$$\sigma_0 = \frac{en_e\vec{v}}{\vec{E}}, \tag{3.18}$$

where $\vec{E}$ can be described by the equation of motion for a charge carrier in a material with finite conductivity. The equation of motion is given as

$$m_e \frac{d\vec{v}}{dt} = e\vec{E} - \frac{m_e \vec{v}}{\tau}, \tag{3.19}$$

where τ is the characteristic scattering time of a charge carrier in the material. At DC, $d\vec{v}/dt \to 0$ such that $\vec{E} = m_e v / e\tau$ and with Equation 3.18 we arrive at

$$\sigma_0 = \frac{e^2 n_e \tau}{m_e}, \tag{3.20}$$

which is the DC conductivity of the material.

For an AC field, $\vec{E} = \vec{E}_0 e^{i\omega t}$, the linear response to the equation of motion is given as

$$\sigma_d(\omega) = \sigma_{d,r}(\omega) - i\sigma_{d,i}(\omega), \tag{3.21}$$

where ω is the frequency of oscillation of the applied field, $\sigma_{d,r}(\omega)$ is the real part, and $\sigma_{d,i}(\omega)$ is the imaginary part. These parts can be expressed as

$$\sigma_{d,r}(\omega) = \frac{\sigma_0}{1 + \omega^2 \tau^2}, \tag{3.22a}$$

$$\sigma_{d,i}(\omega) = \frac{\sigma_0 \omega \tau}{1 + \omega^2 \tau^2}, \tag{3.22b}$$

such that, for normal metals, the Drude model (Drude 1900a, 1900b) predicts the complex conductivity with respect to the scattering time between collision events as

$$\sigma_d(\omega) = \frac{n_e e^2 \tau}{m_e \left(1 + \omega^2 \tau^2\right)} - i \frac{n_e e^2 \omega \tau^2}{m_e \left(1 + \omega^2 \tau^2\right)} = \frac{\sigma_0}{1 + i\omega\tau}, \tag{3.23}$$

where the imaginary part of the Drude conductivity is an effect of the resistance of the charge carriers to an instantaneous change in applied voltage; the electrons take a non-zero time to react to an applied field during the time τ between collisions (Doyle et al. 2008). This inertia of the charge carriers is the manifestation of kinetic inductance. A similar form of conductivity as presented here is present in superconductors.

3.2.3 The Mattis-Bardeen Equations

As discussed previously, conductivity is a measure of the ability of a material to transmit an electrical current and is given generally by (Doyle 2008)

$$\sigma(\omega) = \sigma_1(\omega) - i\sigma_2(\omega), \tag{3.24}$$

where $\sigma_1(\omega)$ is the real part of the conductivity and $\sigma_2(\omega)$ is the complex part. The physical interpretation in the case of the two-fluid model (Bardeen 1958) of superconductivity is that σ_1 is the conductivity due to resistive quasiparticle excitations and σ_2 is the conductivity associated with superconducting Cooper pairs.

Mattis and Bardeen (Mattis and Bardeen 1958) give the general relationship between the complex conductivity of a superconductor to the normal state conductivity as follows:

$$\begin{aligned} \frac{\sigma_1(\omega)}{\sigma_n} &= \frac{2}{\hbar\omega}\int_{\Delta}^{\infty}[f(E) - f(E+\hbar\omega)]g(E,\hbar\omega)dE \qquad &(3.25\text{a})\\ &+ \frac{1}{\hbar\omega}\int_{\Delta-\hbar\omega}^{-\Delta}[1-2f(E+\hbar\omega)]g(E,\hbar\omega)dE, \\ \frac{\sigma_2(\omega)}{\sigma_n} &= \frac{1}{\hbar\omega}\int_{max(\Delta-\hbar\omega,-\Delta)}^{-\Delta}\sqrt{\frac{E^2-\Delta^2}{\Delta^2-E^2}}[1-2f(E+\hbar\omega)]g(E,\hbar\omega)dE, \qquad &(3.25\text{b}) \end{aligned}$$

where E is the energy of the particle state,

$$g(E,\hbar\omega) = \frac{E^2+\Delta^2+\hbar\omega E}{\sqrt{E^2-\Delta^2}\sqrt{(E+\hbar\omega)^2-\Delta^2}}, \tag{3.26}$$

and $f(E)$ is the Fermi-Dirac distribution as given in Equation 3.14. The Fermi-Dirac distribution governs the behavior of quasiparticles in thermal equilibrium as these particles have half-integer spin. These equations for the conductivity of superconductors are valid for $T \ll T_C$.

The Mattis-Bardeen equations can be related to the quasiparticle density with (Gao 2008)

$$\frac{\sigma_1(n_{qp},T)}{\sigma_n} = \frac{2\Delta_0}{\hbar\omega}\frac{n_{qp}}{N_0\sqrt{2\pi k_B T\Delta_0}}\sinh(\chi)K_0(\chi), \tag{3.27a}$$

$$\frac{\sigma_2(n_{qp},T)}{\sigma_n} = \frac{\pi\Delta_0}{\hbar\omega}\left[1-\frac{n_{qp}}{2N_0\Delta_0}\left(1+\sqrt{\frac{2\Delta_0}{\pi k_B T}}e^{-\chi}I_0(\chi)\right)\right], \tag{3.27b}$$

where $\chi = \hbar\omega/2k_BT$, I_0 is the modified zeroth-order Bessel function of the first kind, and K_0 is the modified zeroth-order Bessel function of the second kind. From these equations, it is evident that incident photons that break apart Cooper pairs and create quasiparticles will cause the conductivity of the material to change and therefore will create a measurable response.

It is instructive to quantify how the conductivity of the superconducting material changes with a change in the density of quasiparticles. This is achieved by taking the derivative with respect to the quasiparticle density:

$$\frac{d\sigma_1}{dn_{qp}} = \frac{\sigma_n}{N_0\hbar\omega}\sqrt{\frac{2\Delta_0}{\pi k_B T}}\sinh(\chi)K_0(\chi), \tag{3.28a}$$

$$\frac{d\sigma_2}{dn_{qp}} = -\frac{\pi\sigma_n}{2N_0\hbar\omega}\left(1+\sqrt{\frac{2\Delta_0}{\pi k_B T}}e^{-\chi}I_0(\chi)\right), \tag{3.28b}$$

where Equation 3.28b is used in Chapter 5 to calculate the thermal response of SNRSPD devices.

3.2.4 Surface Impedance

The photon sensitive components of SNRSPD devices, the inductive nanowires, are formed using electron-beam lithography on a thin film. During KID mode measurements, the surface impedance of the thin film nanowire varies with the absorption of photons of energy $\hbar\omega > 2\Delta$ and the concurrent generation of quasiparticles. It is therefore appropriate to derive the surface impedance of thin films.

The superconducting surface impedance is given by

$$Z_S = R_S + iX_S, \tag{3.29}$$

where R_S is the superconducting surface resistance and X_S is the superconducting surface reactance. We will discuss two limits were the surface impedance can be related to the complex conductivity: $t \gg \lambda_{eff}$ and $t \ll \lambda_{eff}$, where t is the thickness of the film and λ_{eff} is the effective penetration depth of the magnetic field and is given by

$$\lambda_{eff} = \sqrt{\frac{\hbar}{\pi\mu_0\Delta\sigma_n}}. \tag{3.30}$$

μ_0 is the permeability of free space, Δ is the temperature dependent energy gap, and σ_n is the normal state conductivity.

Respectively, for $t \gg \lambda_{eff}$ and $t \ll \lambda_{eff}$ (Gao 2008),

$$Z_{S,thick}(\omega, T) = \frac{Z_S(\omega, 0)}{\sqrt{\zeta}}, \tag{3.31a}$$

$$Z_{S,thin}(\omega, T) = \frac{Z_S(\omega, 0)}{t\zeta}, \tag{3.31b}$$

where $Z_S(\omega, 0) = i\omega\mu_0\lambda_{eff}$ is the superconducting surface impedance at zero temperature. The factor ζ is given by

$$\zeta = 1 + \frac{i\delta\sigma(\omega, T)}{\sigma_2(\omega, 0)}, \tag{3.32}$$

where $\delta\sigma(\omega, T) = \sigma_1(\omega, T) - i\delta\sigma_2(\omega, T)$ and $\sigma_1(\omega, T)$ and $\sigma_2(\omega, T)$ are given by Equations 3.27a and 3.27b.

Nanowire devices have films with thickness on the order of a few nanometers. In this case, the mean free path of the electrons is much larger than the thickness and the superconducting surface impedance is given by

$$Z_{S,nano} \approx \frac{1}{t\sigma_2^2}(\sigma_1 + i\omega_2), \tag{3.33}$$

where $R_{S,nano} = \sigma_1/t\sigma_2^2$ and $X_{S,nano} = 1/t\sigma_2$. This thin film impedance can be related to the conductivity with (Zmuidzinas 2012)

$$\frac{\delta Z_{S,nano}(\omega, T)}{Z_{S,nano}(\omega, 0)} \approx -\frac{\delta\sigma(\omega, T)}{\sigma(\omega, 0)}, \tag{3.34}$$

where $\delta Z_{S,nano}(\omega, T) = Z_{S,nano}(\omega, T) - Z_{S,nano}(\omega, 0)$. Probing the superconducting surface impedance therefore allows for information on the complex conductivity to be obtained.

Chapter 4

SUPERCONDUCTING RESONATOR THEORY

This chapter is a review of resonator theory in the context of superconducting nanowire devices. Two types of inductance will be reviewed: geometric and kinetic. The resonator circuit and its properties will be discussed along with various forms of responsivity.

4.1 Classification of Inductance

To understand inductance, we will consider a perfectly conducting wire. With respect to the inductance, the wire has two principle quantities: the rate of change in the current through the wire and the voltage across it. The inductance in the wire is the coefficient of proportionality between these two quantities. There are two types of inductance: geometric and kinetic. For superconducting nanowires, the kinetic term of the total inductance dominates over the geometric term but, for completion, both types of inductance are derived and discussed.

4.1.1 Geometric Inductance

The first type of inductance we will discuss is the geometric inductance. Geometric inductance arises due to the energy stored in the magnetic field of the wire. This stored energy results in a resistance to an instantaneous response of the current to a change in applied voltage.

Consider a perfectly conducting wire of length ℓ and cross-sectional area A as shown in Figure 12. Any current that flows through this wire must conform to Ampère's law which is given as

$$\vec{\nabla} \times \vec{H} = \vec{i}, \tag{4.1}$$

where $\vec{H}$ is the magnetic field and $\vec{i}$ is the current density. The energy density associated with the field is given as $w_m = \mu H^2/2$, where μ is the permeability of the material. From this, we arrive at the total stored magnetic energy:

$$W_M = \frac{\mu}{2} \int H^2 d\mathcal{V} = \frac{1}{2} L_M I^2, \tag{4.2}$$

where $\mathcal{V}$ is the total volume and L_M is the geometric inductance. It is important to note that L_M is dependent only on the geometry of the conductor.

The stored energy in the magnetic field is related to the current in the wire. Each electron experiences a force proportional to the applied voltage, $F = eV/\ell$, such that the power contribution, or rate of change of the energy in the magnetic field ($P = dW_e/dt$), by a single electron is given as

$$P = Fv = \frac{eVv}{\ell}, \tag{4.3}$$

where e is the charge of an electron, V is the applied voltage, and v is the speed of the charge carriers. The total power ($P_{tot} = NP$, where $N = n_e A\ell$ is the total number of charge carriers and n_e is the electron number density) is then given as

$$P_{tot} = n_e AeVv, \tag{4.4}$$

where the current in the wire is $I = n_e evA$, which gives, as expected, $P_{tot} = dW_M/dt = IV$. It is therefore straightforward to show that given Equation 4.2, we arrive at

$$V = L_M \frac{dI}{dt}, \tag{4.5}$$

where it is clear that the geometric inductance is a ratio of the voltage across the wire and the rate of change of the current.

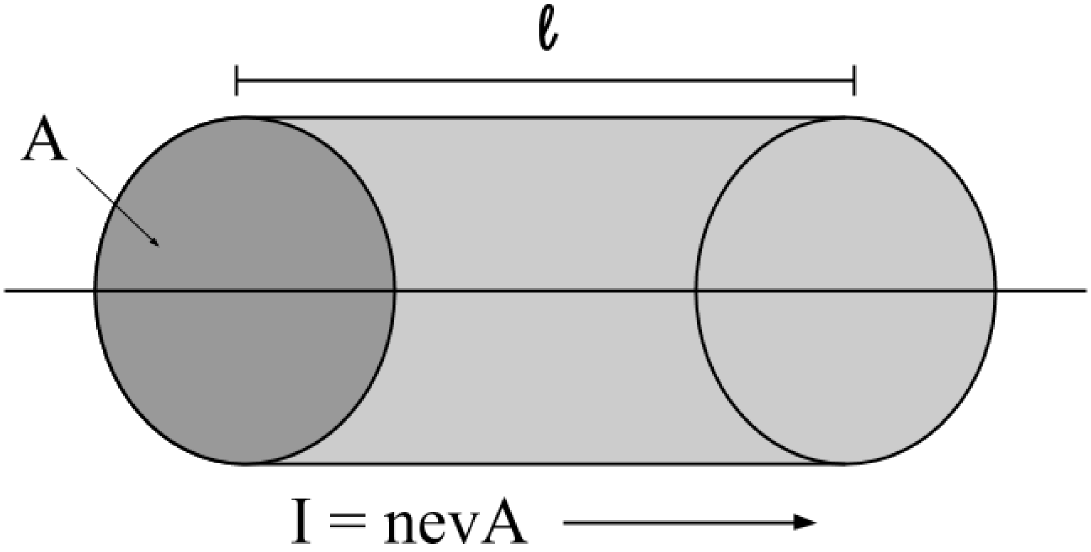

Figure 12: A simplified model of a wire of length ℓ, cross-sectional area A, and current density I.

4.1.2 Kinetic Inductance

The second type of inductance, and the most important type to the present work, is kinetic inductance. Kinetic inductance arises due to the inertia of the charge carries in the wire. Moreover, the inertia of the charge carriers resists an instantaneous change to the applied voltage.

Consider a force acting on a object. The force on the object can be found using the household equation $F = ma$, where m is the mass of an object and a is the acceleration of the object. Mass can be thought of as a measure of an objects inertia, or its tendency toward remaining in its initial state given an applied force. Moreover, the more mass an object has, the slower its speed will increase over time. Kinetic inductance is analogous to the object of mass m undergoing acceleration.

Voltage is related to the force on the charge carriers in a wire by the equation $F = qE$, where $q = e$ is the charge of the electron and $E = V/\ell$ is the magnitude of the electric field due to the applied voltage V over a length ℓ of wire. The voltage applied across some wire can be found using $V = L_K dI/dt$, where L_K is the kinetic inductance of the wire and I is the current. Current can be expressed as $I = n_e evA$, where n_e is the number of charges per unit volume, e is the elementary charge, v is the average velocity of the charge carriers, and A is the cross-sectional area of the wire.

It follows that

$$F = \frac{eV}{\ell} = m\frac{dv}{dt} \implies V = \frac{m\ell}{e}\frac{dv}{dt}, \tag{4.6}$$

where dv/dt can be expressed in terms of the current density given above such that

$$V = \frac{m\ell}{n_e e^2 A}\frac{dI}{dt}, \tag{4.7}$$

where the coefficient $L_{K0} = m\ell/n_e e^2 A$ is the kinetic inductance. The kinetic inductance of a nanowire changes in a non-linear way as a function of bias current as follows:

$$L_K = L_{K0}\left[1 + \left(\frac{I}{I_*}\right)^2\right], \tag{4.8}$$

where I is the bias current and I_* is a parameter of the material and the geometry of the nanowire. This will be explored in Chapter 5.

For nanowire geometries, $L_K >> L_M$, where L_M is the magnetic inductance and is given by (Annunziata 2010)

$$L_M = \frac{\mu_0 \ell}{2\pi}\left[ln\left(\frac{2\ell}{r}\right) - 1\right], \tag{4.9}$$

where μ_0 is the permeability of free space and r is the effective radius of the nanowire. In the case of nanowire inductors, since $L_K \sim \ell/A$ and ℓ is large and A is small, the kinetic inductance dominates over L_M. Therefore, any contribution from L_M will be ignored in the following analysis and it will be held that (Gao 2008)

$$\alpha = \frac{L_K}{L_T} = 1, \tag{4.10}$$

where $L_T = L_K + L_M$ is the total inductance and is virtually equal to L_K. The kinetic inductance of superconducting films is the phenomenon that underlies every technology we analyze in this dissertation.

4.2 Quality Factors and Time Constants

Resonators can be characterized based on their ability to store energy. This characterization can be discussed in terms of the quality factors and the intrinsic time constants associated with a given resonator.

4.2.1 Resonator Detector Quality Factors

The total resonator quality factor is given by (Tooley 2006)

$$Q_r = \frac{f_0}{\Delta f_{3dB}}, \tag{4.11}$$

where f_0 is the central resonant frequency and Δf_{3dB} is the half-power bandwidth of the resonance dip. Q_r scales with the sharpness of the resonance feature, which corresponds to a change in energy storage efficiency. Q_r can be written as a combination of quality factors given by

$$Q_r = \left(\frac{1}{Q_i} + \frac{1}{Q_c} + \frac{1}{Q_\ell}\right)^{-1}, \tag{4.12}$$

where Q_i is the internal quality factor, Q_c is the coupling quality factor, and Q_ℓ is the quality factor associated with processes that induce loss in addition to the loss associated with the quasiparticle density.

Assuming that the capacitors are non-limiting, the internal quality factor of the resonator is dependent only on the inductive component. An inductor with a series loss resistance has a quality factor given by

$$Q_i = \frac{\omega_0 L_K}{R}, \tag{4.13}$$

where ω_0 is the angular resonant frequency, L_K is the kinetic inductance, and R is the series loss resistance.

The coupling to a microwave feedline is described by the coupling quality factor Q_c. Moreover, Q_c is a measure of the amount of energy that leaks from the resonator (Gao 2008) and is given by

$$Q_c = \frac{2(C_P + C_C)}{\omega_0 C_C^2 Z_0}, \tag{4.14}$$

where Z_0 is the characteristic impedance of the microwave feedline.

4.2.2 Two-Fluid Model Quality Factor

The internal quality factor with respect to the two-fluid model can be derived via a consideration of the impedance of the inductive branch of the resonator. The inductive branch consists of the inductor in series with a resistor representing the quasiparticles. This can be further represented by considering the magnetic component of the inductance to be in series with a parallel combination of the kinetic component of the inductance and the resistive quasiparticles.

Assuming that the associated quality factors of the capacitors are non-limiting, the internal quality factor of this branch can be found with (Di Paolo 2000)

$$Q_i = \frac{Im\{Z_L(\omega_0)\}}{Re\{Z_L(\omega_0)\}} = \frac{X_L(\omega_0)}{R_L(\omega_0)}, \tag{4.15}$$

where $X_L(\omega_0)$ is the reactance of the inductor, $R_L(\omega_0)$ is the series resistance of the inductor, and $Z_L(\omega_0)$ is the impedance of the inductor which is evaluated at the center of the resonance feature. For a variable frequency ω, $Z_L(\omega)$ is given as

$$\begin{aligned} Z_L(\omega) =& i\omega L_M + \frac{1}{\frac{1}{R_{qp}} + \frac{1}{i\omega L_K}} \\ =& i\omega L_M + \frac{i\omega L_K R_{qp}^2 + \omega^2 L_K^2 R_{qp}}{R_{qp}^2 + \omega^2 L_K^2}, \end{aligned} \tag{4.16}$$

where R_{qp} is the resistance due to the quasiparticle density in the material. The first term is a consequence of the magnetic inductance and the second term is a consequence of the series contribution to the impedance from the kinetic inductance of the Cooper pairs and the resistance of the quasiparticles.

The devices relevant to this dissertation are operated well below the critical temperature of the material from which they are fabricated. Therefore, since $T \ll T_C$, the impedance contribution from the quasiparticles dominates and we can write Equation 4.16 as

$$Z_L(\omega) = \frac{\omega^2 L_K^2}{R_{qp}} + i\omega(L_M + L_K). \tag{4.17}$$

Applying Equation 4.17 to Equation 4.15, we arrive at

$$Q_i = \frac{L_M + L_K}{L_K} \frac{R_{qp}}{\omega_0 L_K} = \frac{R_{qp}}{\omega_0 L_K}, \tag{4.18}$$

for $L_K >> L_M$ as is the case for nanowires. The conductivity of the quasiparticles varies with frequency such that the dependence of Q_i on R_{qp} is indicative of a variation of the resonator quality factor as a function of frequency because R_{qp} itself is a function of frequency.

4.2.3 Time Constants

The resonator time constant is defined as the period over which the resonator loses energy during an oscillation (Wernis 2013) and is given in terms of Q_r by

$$\tau_r = \frac{Q_r}{\pi f_0}. \tag{4.19}$$

The quasiparticle time constant at low temperatures for clean materials is given as (Kaplan et al. 1976)

$$\begin{aligned}\tau_{qp} =& \frac{\tau_0}{\sqrt{\pi}} \left(\frac{k_B T_C}{2\Delta_0}\right)^{5/2} \sqrt{\frac{T_C}{T}} e^{\Delta_0/k_B T} \\ =& \frac{\tau_0}{n_{qp}} \frac{N_0 (k_B T_C)^2}{2\Delta_0^2},\end{aligned} \tag{4.20}$$

were τ_0 is the material dependent electron-phonon interaction time which can easily found in the literature (e.g. for Niobium, $\tau_0 = 1.49 \times 10^8$s (Kaplan et al. 1976)). τ_{qp} corresponds to the lifetime of a quasiparticle before recombination into a Cooper pair.

4.3 Impedance of a Parallel Resonator with a Coupling Capacitor

To understand the behavior of the SNRSPD circuit, we analyze the impedance of the circuit coupled to a microwave feedline. The circuit contains a parallel resonator coupled to the feedline via a capacitor. We can write the total impedance as the sum of two impedances,

$$Z_T = Z_1 + Z_2, \tag{4.21}$$

where Z_1 is the impedance of the coupling capacitor C_C, and Z_2 is the impedance of the parallel inductor L and capacitor C_P. It is instructive to consider the ideal case without added series resistance due to quasiparticles. The reactance equations for ideal inductors and capacitors are $X_L = i\omega L$ and $X_C = 1/i\omega C$ such that Equation 4.21 may be written as:

$$Z_T = \frac{1}{i\omega C_C} + \frac{L/C_P}{i\omega L + 1/i\omega C_P}, \tag{4.22}$$

where the resonant frequency ω_0 may be calculated by setting the impedance Z_T to zero and is found to be:

$$\omega_0 = 2\pi f_0 = \frac{1}{\sqrt{L(C_C + C_P)}}. \tag{4.23}$$

With series resistance added due to the existence of quasiparticles in the inductive component, the shunt impedance to ground is given by

$$\begin{aligned} Z_r(\omega) =& \frac{1}{i\omega C_C} + \frac{1}{i\omega C_P + \frac{1}{i\omega L + R}} \\ =& \frac{1}{i\omega C_C}\left[\frac{1 - \omega^2 L(C_P + C_C) + i\omega R(C_P + C_C)}{1 - \omega^2 L C_P + i\omega R C_P}\right], \end{aligned} \tag{4.24}$$

where using Equation 4.23, we arrive at

$$Z_r(\omega_0) = R\left(\frac{C_P + C_C}{C_C}\right)^2 \frac{1}{1 + i\omega_0 RC\left(\frac{C_P + C_C}{C_C}\right)} = \frac{Z_0}{2}\frac{Q_c}{Q_i}\frac{1}{1 + i\epsilon}, \tag{4.25}$$

where

$$\epsilon = \omega_0 RC\left(\frac{C_P + C_C}{C_C}\right) = \frac{C_P}{Q_i C_C} \tag{4.26}$$

and Q_i is given in Equation 4.14.

We can modify Equation 4.25 to include frequencies near resonance with a Taylor expansion:

$$Z_r(\omega) \cong \left(\frac{Z_0}{2}\frac{Q_c}{Q_i} + iZ_0 Q_c x\right)\frac{1}{1 + i\epsilon}, \tag{4.27}$$

where x is the fractional detuning of the resonant frequency given by

$$x = \frac{\delta\omega}{\omega_0} = \frac{\omega - \omega_0}{\omega_0}. \tag{4.28}$$

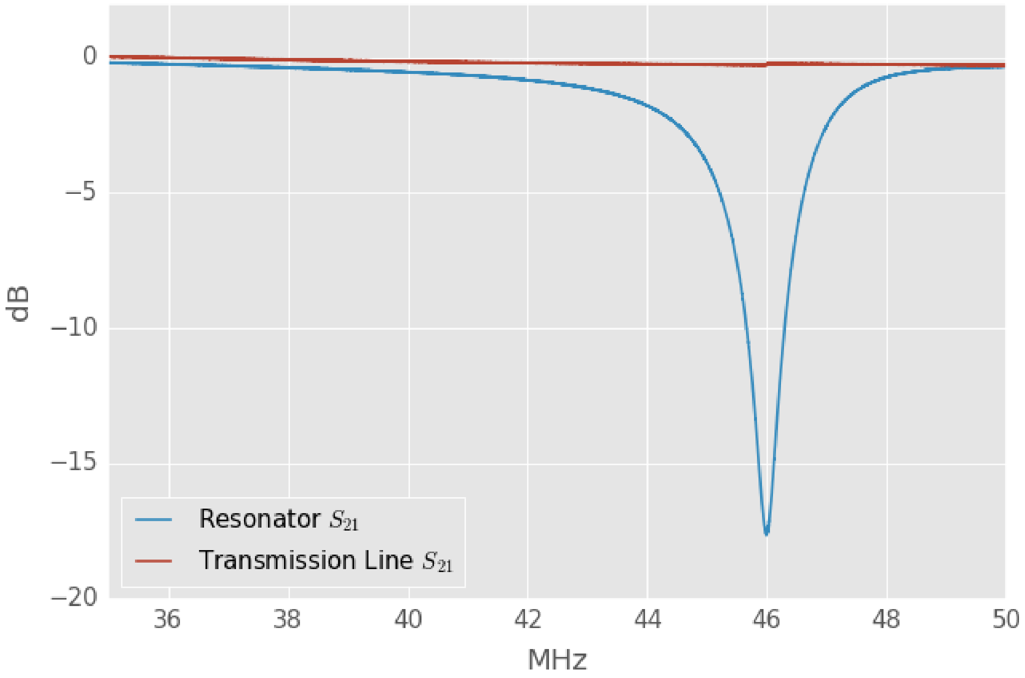

Figure 13: S_{21} is shown for a resonator (red) and for a transmission line (blue).

In general, the response of resonators embedded in a two-port network can be characterized based off of a scattering matrix given by

$$\begin{pmatrix} V_1^- \\ V_2^- \end{pmatrix} = \begin{pmatrix} S_{11} & S_{12} \\ S_{21} & S_{22} \end{pmatrix} \begin{pmatrix} V_1^+ \\ V_2^+ \end{pmatrix},$$

where V_1^- and V_2^- are the voltage waves traveling from port 1 and 2, and V_1^+ and V_2^+ are the voltage waves incident on port 1 and 2. From this, it is clear that the outgoing waves take the following form:

$$V_1^- = S_{11}V_1^+ + S_{12}V_2^+, \tag{4.29a}$$

$$V_2^- = S_{21}V_1^+ + S_{22}V_2^+. \tag{4.29b}$$

In the case of a realistic measurement, the scattering parameters are measured in a calibrated setup such that the impedance of the load is matched to the characteristic impedance of the current carrying lines ($Z_L = Z_0$). This ensures that there will be no reflected waves from the load ($V_2^+ = 0$) due to an impedance mismatch. Moreover, we arrive at the reflection and transmission coefficients in terms of the traveling waves:

$$S_{11} = \frac{V_1^-}{V_1^+}, \tag{4.30a}$$

$$S_{21} = \frac{V_2^-}{V_1^+}. \tag{4.30b}$$

S_{11} and S_{21} are of particular importance to resonator analysis because they describe the reflected voltage signal and the transmitted voltage signal, respectively. These two scattering parameters are related by

$$S_{11} = S_{21} - 1, \tag{4.31a}$$

$$|S_{11}|^2 + |S_{21}|^2 = 1, \tag{4.31b}$$

which shows that if a signal is injected into port 1, then any portion that is not transmitted to port 2 must be reflected and arrive back at port 1.

For an ideal transmission line and for all frequencies, no reflection occurs ($S_{11} = 0$) and the signal is completely transmitted ($S_{21} = 1$) in accordance to with Equation 4.31a. In the case of a resonator, at and around the resonant frequency of the circuit, power is reflected such that a Lorentzian resonant feature is observed in S_{11} and S_{21} (Figure 13).

The reflection coefficient can be written as a function of the impedance of the resonator and the characteristic impedance and is given by

$$S_{11} = -\frac{1}{1 + 2Z_r/Z_0}, \tag{4.32}$$

where using Equation 4.31a, S_{21} is found to be

$$S_{21} = 1 - \frac{1}{1 + 2Z_r/Z_0}. \tag{4.33}$$

Making a substituting of Equation 4.27 into Equation 4.33, we obtain

$$S_{21} = 1 - \frac{1 + i\epsilon}{1 + i\epsilon Qr/Q_c}\frac{Q_r}{Q_c}\left[\frac{1}{1 + 2iQ_r x/(1 + i\epsilon Q_r/Q_c)}\right], \tag{4.34}$$

where Q_r is given by Equation 4.12 with $Q_\ell = 0$, Q_c is given by Equation 4.14, x is given by Equation 4.28, and ϵ is given by Equation 4.26.

In the limit where $\epsilon \ll 1$ ($Q_i C_C \gg C_P$), we arrive at the following expressions:

$$S_{11}(x) \cong -\frac{Q_r}{Q_c}\frac{1}{1 + 2iQ_r x}, \tag{4.35a}$$

$$S_{21}(x) \cong 1 - \frac{Q_r}{Q_c}\frac{1}{1 + 2iQ_r x}, \tag{4.35b}$$

where it is clear from these equations and from the definition of x that off-resonance, $S_{21} \rightarrow 1$, which corresponds to perfect transmission, and as the frequency approaches the resonant frequency, $S_{21} \rightarrow 0$ limited by Q_r and Q_c (Figure 13).

The analyses of that last two sections shows that a resonator detector is adequately described by the impedance of the resonator $Z_r(\omega)$ and by the transfer function S_{21}. Equations 4.24 and 4.33 are a function of circuit parameters (L,C_C,C_P,R,Z_0) that can be described by empirical parameters (ϵ,ω_0,Q_r,Q_c). Equations 4.27 and 4.35b are a function of these empirical parameters.

4.5 Thermal Response

The resonant frequency of an SNRSPD varies as a function of base temperature. This is due to the change in the population of quasiparticles present in the superconducting film. Heat quanta known as phonons that have an energy greater than twice the superconducting gap energy are able to break apart Cooper pairs. The response of the frequency with respect to a change in base temperature and therefore a change in quasiparticle number can be predicted with a chain-rule approach given by (Mauskopf 2018)

$$\frac{df_0}{dT} = \frac{df_0}{d\sigma_2}\frac{d\sigma_2}{dn_{qp}}\frac{dn_{qp}}{dT}, \tag{4.36}$$

where f_0 is the resonant frequency, σ_2 is the complex conductivity of the NbN nanowire material, n_{qp} is the number density of quasiparticles, and T is the base temperature.

The resonant frequency can be written as

$$f_0 = \frac{1}{2\pi\sqrt{L_K C_T}}, \tag{4.37}$$

where L_K is the kinetic inductance and C_T is the total capacitance of the coupling capacitor and the resonator capacitor. The kinetic inductance is dependent on the complex conductivity in the following fashion:

$$L_K = \frac{1}{\omega_0 \sigma_2 t}, \tag{4.38}$$

where ω_0 is the angular resonant frequency and t is the thickness of the NbN film.

The total conductivity of the NbN nanowire is given in Equation 3.24. For low temperatures where the Cooper pairs dominate the conductivity, $\sigma_2 >> \sigma_1$, such that $\sigma \to \sigma_2$. The first factor of Equation 4.36, $df_0/d\sigma_2$, can then be found to be

$$\frac{df_0}{d\sigma_2} = \frac{d}{d\sigma_2}\left[\frac{1}{2\pi}\left(\frac{C_T}{\omega_0\sigma_2 t}\right)^{-\frac{1}{2}}\right] = \frac{f_0}{2\sigma_2}, \tag{4.39}$$

where this dependence of the resonant frequency on the conductivity indicates that the dependence of the frequency on the base temperature will be dependent on the frequency itself.

Mattis-Bardeen theory gives σ_2 as a function of quasiparticle number density and base temperature as shown in Equation 3.28b. Since $\hbar\omega_0/2kT \to 0$ for ω_0 in the Very High Frequency (VHF) band, σ_2 simplifies to

$$\sigma_2 = \frac{\pi\Delta_0}{\hbar\omega_0}\left(1 - \frac{n_{qp}}{2N_0\Delta_0}\right), \tag{4.40}$$

where, at low temperatures, the number density of quasiparticles is given by Equation 3.15.

The second factor of Equation 4.36, $d\sigma_2/dn_{qp}$, can then be found as

$$\frac{d\sigma_2}{dn_{qp}} = \frac{d}{dn_{qp}}\left[\frac{\pi\Delta_0}{\hbar\omega_0}\left(1 - \frac{n_{qp}}{2N_0\Delta_0}\right)\right] = \frac{-\pi}{2\hbar\omega_0 N_0}, \tag{4.41}$$

where multiplying by a factor of σ_2/σ_2 and taking the limit where $N_0 >> n_{qp}$, we arrive at

$$\frac{d\sigma_2}{dn_{qp}} = \frac{-\sigma_2}{2N_0\Delta_0}, \tag{4.42}$$

where the σ_2 dependence will cancel out when multiplied by $df_0/d\sigma_2$.

The third factor of Equation 4.36, dn_{qp}/dT, can be found as

$$\frac{dn_{qp}}{dT} = \frac{d}{dT}\left[2N_0\sqrt{2\pi kT\Delta_0}e^{-\frac{\Delta_0}{kT}}\right] = n_{qp}\left(\frac{\Delta_0}{kT^2} + \frac{1}{2T}\right), \tag{4.43}$$

and by combining all three factors, we arrive at

$$\frac{df_0}{dT} = -f_0\sqrt{\frac{\pi k}{2\Delta_0 T}}\left(\frac{\Delta_0}{kT} + \frac{1}{2}\right)e^{-\frac{\Delta_0}{kT}}. \tag{4.44}$$

4.6 Optical Response

The usefulness of an astronomical detector is determined by its ability to respond to incident power from photons. This is achieved through the breaking of Cooper pairs by absorbing incident photons of sufficient energy. In the case of SNRSPD devices, we are able to sense this process through a change in resonant frequency. The resonant frequency changes as a function of absorbed power such that (Mauskopf 2018)

$$\frac{df_0}{dP_{abs}} = \frac{df_0}{d\sigma_2}\frac{d\sigma_2}{dn_{qp}}\frac{dn_{qp}}{dP_{abs}}, \tag{4.45}$$

where P_{abs} is the total power absorbed by the nanowire within the quasiparticle lifetime. Noting that the first two factors of Equation 4.45 are given by Equations 4.39 and 4.42, we arrive at

$$\frac{df_0}{d\sigma_2}\frac{d\sigma_2}{dn_{qp}} = \frac{-f_0}{4N_0\Delta_0}. \tag{4.46}$$

If we are in the regime where optically generated quasiparticles dominate the total number of quasiparticles, then the third factor of Equation 4.45 takes the form

$$\frac{dn_{qp}}{dP_{abs}} = \frac{n_{qp}}{2P_{abs}}. \tag{4.47}$$

This results in a dependence of the shift in frequency on the inverse square root of the absorbed power P_{abs} and detector volume Σ given by

$$\frac{df_0}{dP_{abs}} = \frac{-f_0 n_{qp}}{8N_0\Delta_0 P_{abs}} \propto \frac{1}{\sqrt{P_{abs}\Sigma}}, \tag{4.48}$$

where the absorbed photon power P_{abs} is not directly attainable within our experimental setup. One solution is to find an equivalent P_{abs} from thermal response data for the same change in quasiparticle number density n_{qp}.

If we are in the regime where thermally generated quasiparticles dominate the total number of quasiparticles, then the third factor of Equation 4.45 takes the form

$$\frac{dn_{qp}}{dP_{abs}} = \frac{\eta\tau_{qp}}{\Delta_0\Sigma}. \tag{4.49}$$

This results in a dependence of the shift in frequency on the quasiparticle lifetime τ_{qp} and on the inverse of the detector volume Σ given by

$$\frac{df_0}{dP_{abs}} = \frac{-f_0\eta\tau_{qp}}{4N_0\Delta_0^2\Sigma} \propto \frac{\tau_{qp}}{\Sigma}. \tag{4.50}$$

In the cases of both Equations 4.48 and 4.50, the intrinsically small volume of nanowire detectors results in an improvement in optical responsivity over other traditional KID-style detectors.

Given that we know how n_{qp} changes with a change in base temperature, we can find dn_{qp} for a particular shift in resonant frequency df_0 as a function of temperature. Using results for Δ_0 and for Σ, we can determine $\eta P_{abs} \tau_{qp}$. We can then find P_{abs} for a given frequency shift if we assume values for η and τ_{qp}. By adding optical power with a calibrated light source at a constant base temperature until we reach the same df_0 and therefore the same dn_{qp}, we can determine how much optical power was required to cause the shift. In this way, we can calibrate the SNRSPD to measure absorbed power from a source of unknown calibration such as light collected by a telescope from a star.

4.7 Non-Linear Response

The resonant frequency changes as a function of kinetic inductance such that

$$\frac{df_0}{dL_{K0}} = -\frac{1}{2\pi\sqrt{L_{K0}C_T}}\frac{1}{2L_{K0}} = -\frac{f_0}{2L_{K0}}, \tag{4.51}$$

where L_{K0} is the kinetic inductance in the linear regime with no applied current. It can then be deduced that for small changes in the resonant frequency, we obtain corresponding small changes in the kinetic inductance such that

$$dL_K = -\frac{df_0}{f_0} 2L_{K0}, \tag{4.52}$$

where df_0 is the change in the resonant frequency.

For small changes in the kinetic inductance due to an applied current, Equation

4.8 gives

$$dL_K = L_{K0}\left(\frac{dI}{I_*}\right)^2, \tag{4.53}$$

where I is the applied current and I_* is a property of the nanowire material and geometry.

From Equations 4.52 and 4.53:

$$-\frac{df_0}{f_0}2L_{K0} = L_{K0}\left(\frac{dI}{I_*}\right)^2 \tag{4.54}$$

$$\implies \frac{df_0}{dI^2} = -\frac{f_0}{2}\frac{1}{I_*^2}, \tag{4.55}$$

where I_* can be determined by measuring the frequency shift as a function of bias current.

4.8 Power Dissipation and Energy Stored in a Resonator

The amount of the total readout power dissipated in a resonator can be written in terms of the reflection and transmission coefficients given in Equations 4.35a and 4.35b. This is expressed as

$$P_{diss} = P_{readout}(1 - |S_{11}|^2 - |S_{21}|^2) = P_{readout}\left(\frac{2Q_r^2}{Q_iQ_c}\frac{1}{1+4Q_r^2x^2}\right), \tag{4.56}$$

where x is the fractional detuning defined in Equation 4.28.

The energy stored in a resonator is then given as a function of the dissipated power by

$$E_r = \frac{Q_iP_{diss}}{\omega_0} = \frac{2Q_r^2}{Q_c}\frac{1}{1+4Q_r^2x^2}\frac{P_{readout}}{w_0}, \tag{4.57}$$

which can be related to the current in the inductor by the familiar formula for energy stored in the magnetic field, $E_r = LI^2/2$.

Chapter 5

SNRSPD TWO-PIXEL PROTOTYPE

In this chapter, the characterization of an SNRSPD two-pixel prototype is presented. This includes an overview of the experimental apparatus and the measurements taken. From the experimental data, parameters of the SNRSPD devices are determined including kinetic inductance, parasitic resistance, quality factors, band-gap energy, critical temperature, and characteristic current. Additionally, calculations of the quasiparticle number from thermal and non-linear response data are presented.

Following the characterization of the SNRSPD devices, the performance of two detection modes is discussed: i) as a kinetic inductance detector (KID) or ii) as a single-photon detector (SPD). The two superconducting nanowires developed for use as single-photon detectors (SNSPD) are embedded as the inductive (L) component in resonant inductor/capacitor (LC) circuits coupled to a microwave transmission line. The capacitors are low loss commercial chip capacitors and limit the internal quality factor of the resonators to approximately $Q_i = 170$. The resonator quality factor, approximately $Q_r = 23$, is dominated by the coupling to the feedline and limits the detection bandwidth to on the order of 1MHz. When operated in KID mode, the detectors are AC biased with tones at their resonant frequencies of 45.85 and 91.81MHz. In the low-bias, standard KID mode, a single photon produces a hot spot that does not turn an entire section of the line normal but only increases the kinetic inductance. In the high-bias, critical KID mode, a photon event turns a section of the line normal and the resonance is destroyed until the normal region is dissipated. When operated as an SPD in Geiger mode, the resonators are DC biased through cryogenic bias tees and each photon produces a sharp voltage step followed by a ringdown signal at the resonant frequency of the detector which is converted to a standard pulse with an envelope detector. We show that AC biasing in the critical KID mode is inferior to the sensitivity achieved in DC-biased SPD mode due to the small fraction of time spent near the critical current with an AC bias.

5.1 Characterization of Superconducting Nanowire Resonator Single Photon Detectors

5.1.1 Experimental Apparatus

5.1.1.1 Preliminary Setup

In order to prove the concept of an SNRSPD array, preliminary testing was done in a liquid helium Infrared Laboratories, Inc. HD-3 cryogenic dewar and analysis was carried out in AWR Microwave Office. A resonator detector was assembled with two 10pF surface mount device (SMD) capacitors. The resonator was cooled to a bath temperature of $T = 4.2$K. A cryogenically cooled $30dB$ attenuator was used at the RF input of the resonator package and a cryogenically cooled low noise amplifier (LNA) developed at ASU was used to boost the signal with 30dB of power gain at the output with 4K of input referred noise temperature. The full setup is shown as a schematic in Figure 14 and the physical assembly inside the dewar is shown in Figure 15. A model with a parasitic resistance of 12Ω matches the measured resonance curve shown in Figure 16. This resistance is likely due to nano-bridging within the nanowires active area due to oxidization of the material over time. The critical current was found to

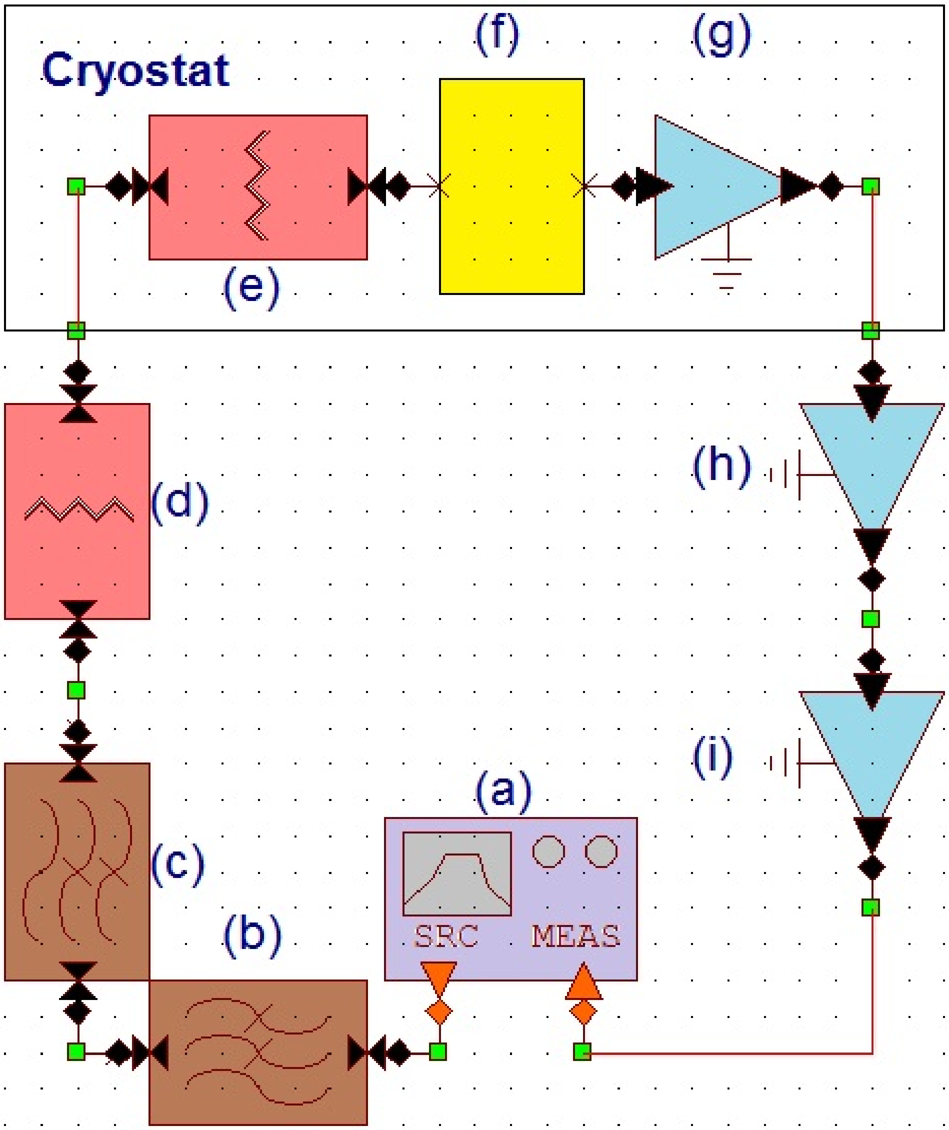

Figure 14: (a) VNA. (b) & (c) 200MHz LPFs. (d) 60dB Attenuator. (e) 30dB Cryogenic Attenuator. (f) SNRSPD Package. (g) 30dB Cryogenic Low Noise Amplifier (LNA). (h) & (i) 40dB Amplifiers.

be abnormally low ($I_C = 1.5\mu$A). At this point, though the concept was proven, the device was considered to be defective and two new devices were connected to the microwave feedline for further testing.

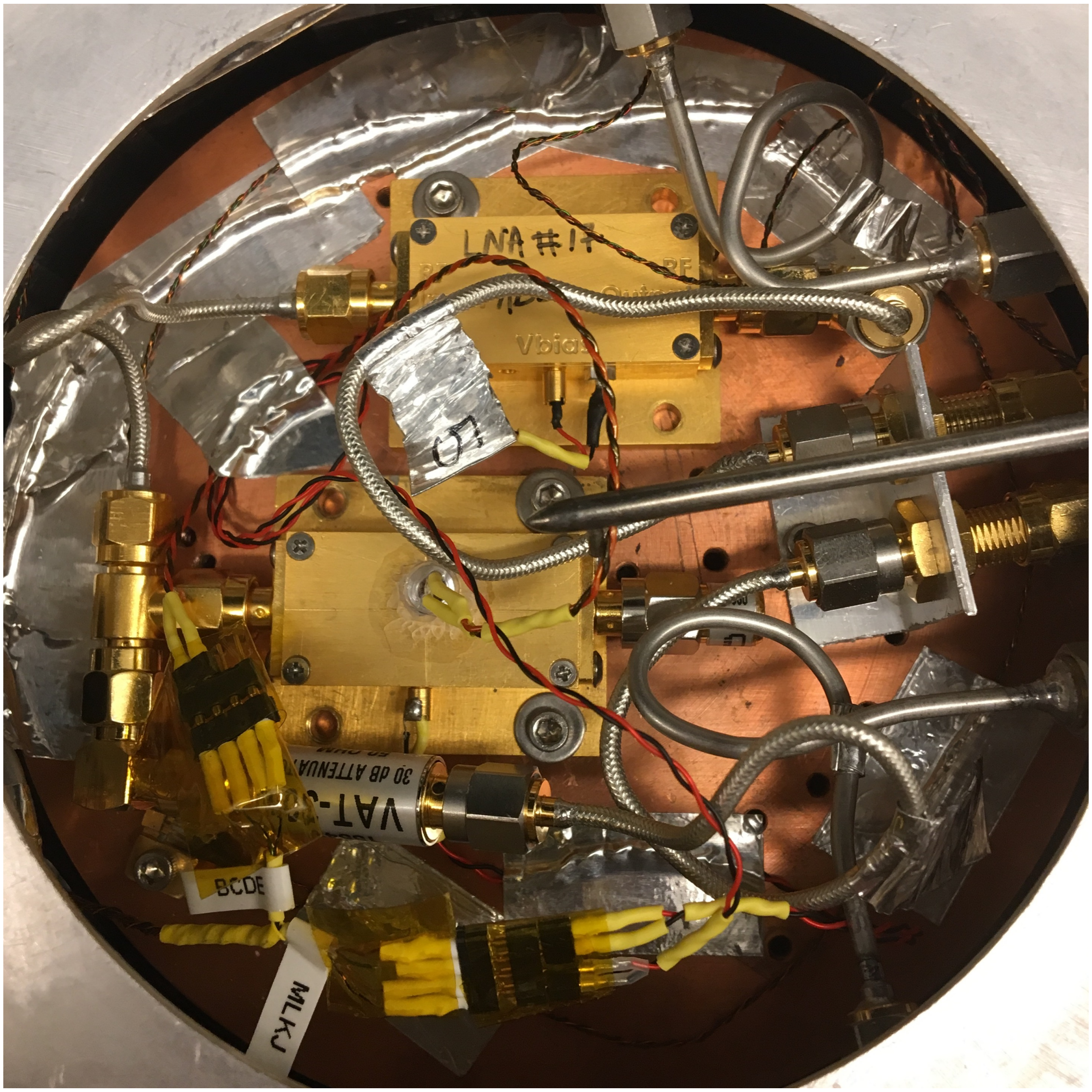

Figure 15: The inside of the liquid helium Infrared Laboratories, Inc. HD-3 cryogenic dewar. The implemented cold 30dB attenuator and ASU cryogenic LNA are connected to the SNRSPD package. A 1300nm central-wavelength LED was situated above the nanowire chip for photon power absorption experiments.

5.1.1.2 Final Setup

In order to better characterize SNRSPD devices, nanowires with critical currents of $I_C \sim 5\mu$A were chosen to be measured. Figure 17a shows the circuit diagram of

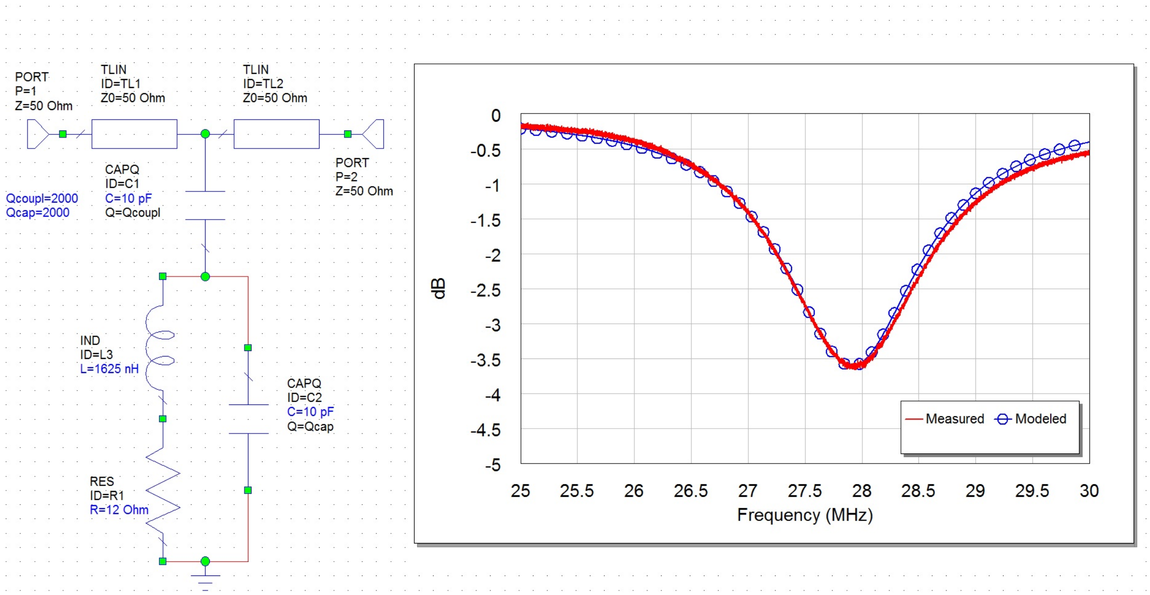

Figure 16: A model was drawn in AWR Microwave office and was matched to the measured resonance curve. An effective series resistance of 12Ω was found to provide a curve that matched the data.

the two devices. The physical assembly is shown in Figure 17b. The central chip contains an array of 32 individual meandering NbN nanowires on a silicon nitride-on-silicon substrate and was fabricated at MIT by the Quantum Nanostructures and Nanofabrication Group. The nanowires consist of serially connected parallel sections with nominal widths of 60nm. The total length of the nanowire is 500μm and the thickness is $\sim$ 4nm.

For each SNRSPD, an SMD coupling capacitor C_C is connected in series with the parallel resonator made up of the nanowire and an SMD capacitor C_P. For the first device, $C_{C1} = 3$pF and $C_{P1} = 1$pF. For the second device, $C_{C2} = 10$pF and $C_{P2} = 10$pF. This concept is similar to that proposed by Doerner et al., where instead of SMD capacitors, interdigital capacitors are used. 50Ω lines lead to input/output ports on each side. Each nanowire is connected to its respective circuit with 25μm

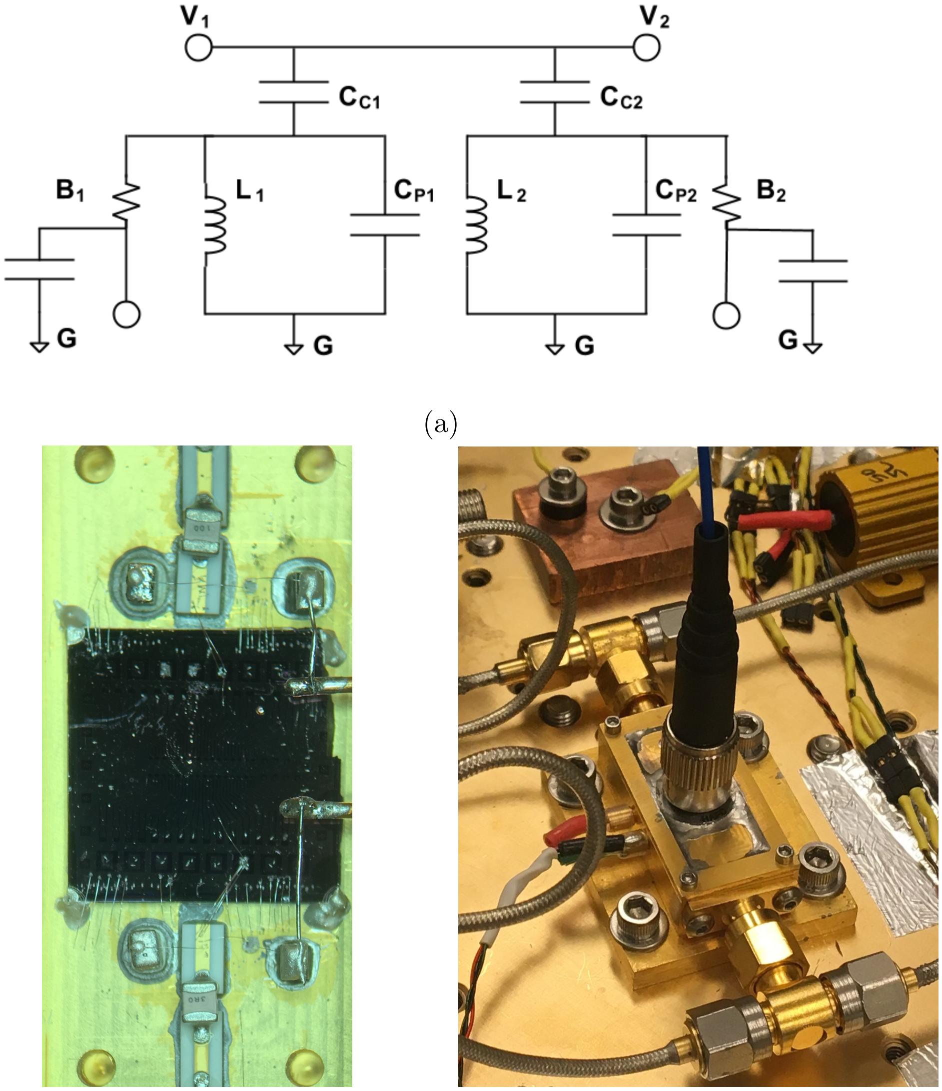

(a)

(b)

(c)

Figure 17: (a) Circuit diagram of two devices on the same feedline. V_1 and V_2 are the input and output ports. L_1 and L_2 are the inductive nanowires. C_{C1} and C_{C2} are the coupling capacitors. C_{P1} and C_{P2} are the parallel capacitors. B_1 and B_2 are bias-tees. G is the common ground. (b) Micro-assembly inside the detector package. (c) Fiber-coupled detectors mounted inside the Sumitomo RP-082 cryostat on the cold-plate.

diameter aluminum wire. A bias tee is also implemented on each side in order to apply a DC bias to the nanowire and probe non-linear effects.

A Sumitomo RP-082 closed-cycle cryogenic cooler was used to cool the resonators to a bath temperature of $T = 2.7$K. A cryogenically cooled 30dB attenuator was used at the RF input of the resonator package and a cryogenically cooled low noise amplifier (LNA) developed at ASU was used to boost the signal with 30dB of power gain at the output with 4K of input referred noise temperature. Figure 17c shows the mounted package coupled to a multi-mode fiber optic cable. A 1.3μm central-wavelength LED is situated above the nanowire chip and was used to apply optical power. The LED was biased with a Keithley 2400 series precision source measurement unit (SMU). The implemented cold attenuator and ASU cryogenic LNA are connected to the SNRSPD package and a temperature sensor is mounted nearby.

The readout system is made up of an Agilent E5072A vector network analyzer (VNA), low pass filters (LPFs), attenuators, and amplifiers as shown in Figure 14. -20dBm is outputted by the VNA which results in -110dBm of power incident on the SNRSPDs. The measurements that follow were carried out with an unvarying -110dBm of power. The low pass filters and attenuators were added to reduce noise. The signals from the SNRSPDs were amplified in order to be distinguishable from the baseline noise.

5.1.2 Critical Temperature

The critical temperature T_C was determined to be 8.5K by heating the coldplate near the device in small steps with a 50Ω resistor. Figure 18 shows the resulting superconducting phase transition. For bulk NbN, the critical temperature is ≈16.2K (Matthias, Geballe, and Compton 1963; Beebe et al. 2016). Bulk values essentially refer to the properties that a material of infinite volume would possess when surface

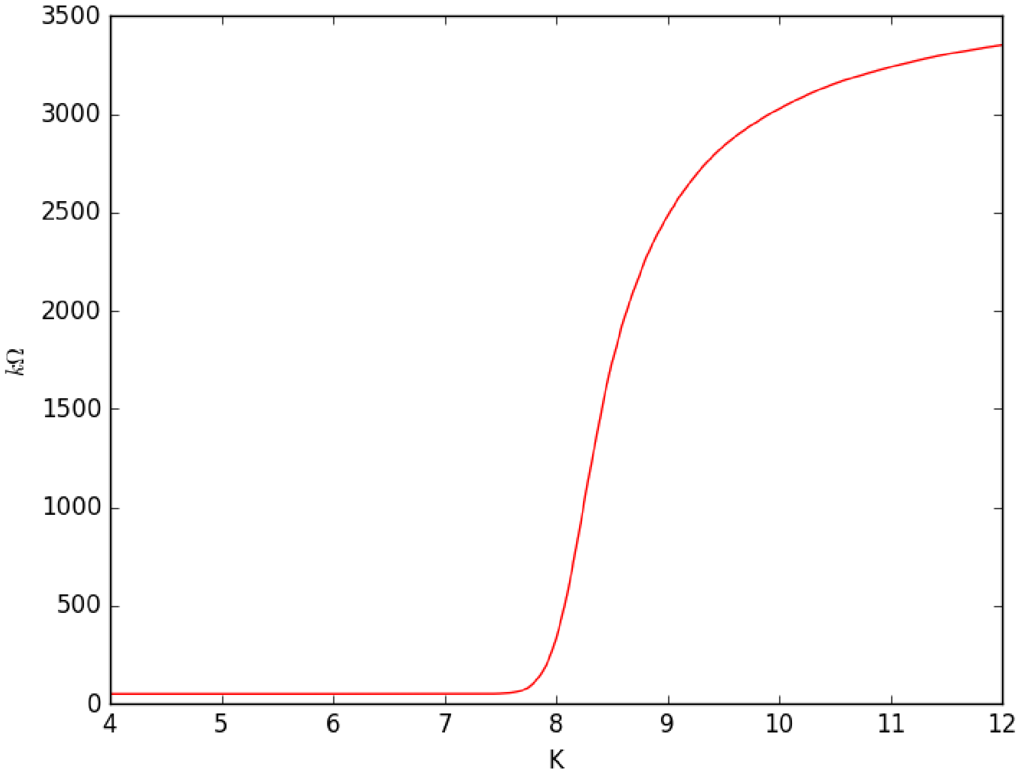

Figure 18: Superconducting phase transition for the nanowires with the critical temperature found to be 8.5K with $\Delta T_C \sim 1$K.

effects are negligible. The film thickness of the NbN nanowire measured here is ≈4nm. In this regime, the bulk value of the critical temperature is modified as a function of film thickness. Our value of $T_C = 8.5$K matches the value reported by Bedorf for a film thickness of ≈3-4nm (Bedorf 2005) and Smirnov et al. for a film thickness of ≈5nm (Smirnov et al. 2016).

Ivry et al. report that superconductivity scales as $dT_C(R_S)$ and is quantifiable as a power law, where d is the film thickness, T_C is the critical temperature, and R_S is the sheet resistance (Ivry et al. 2014). There will also be variance of the critical temperature in separate batches of NbN due to uncertainty in the exact ratio between the niobium and the nitrogen during deposition. This is known as stoichiometry. It has been found that adding an aluminum nitride (AlN) buffer layer to to NbN films increase the critical temperature of the film. For an 8nm film, the critical temperature of NbN increased from 7.3K to 10.5K (Shiino et al. 2010).

5.1.3 Kinetic Inductance

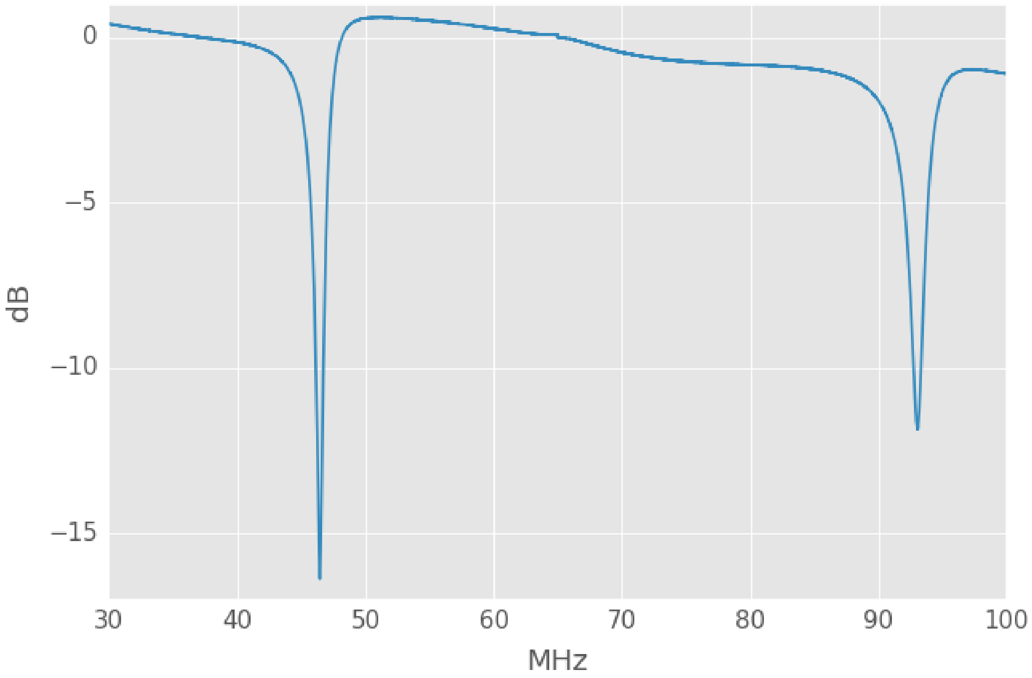

Figure 19: The resonant frequencies 46.5MHz and 93.1MHz are shown for SNRSPD1 and SNRSPD2, respectively. The physical temperature of the package was $T = 2.80$K and the microwave power was at $P = -110$dBm.

The kinetic inductance of the nanowires can be found by rearranging Equation

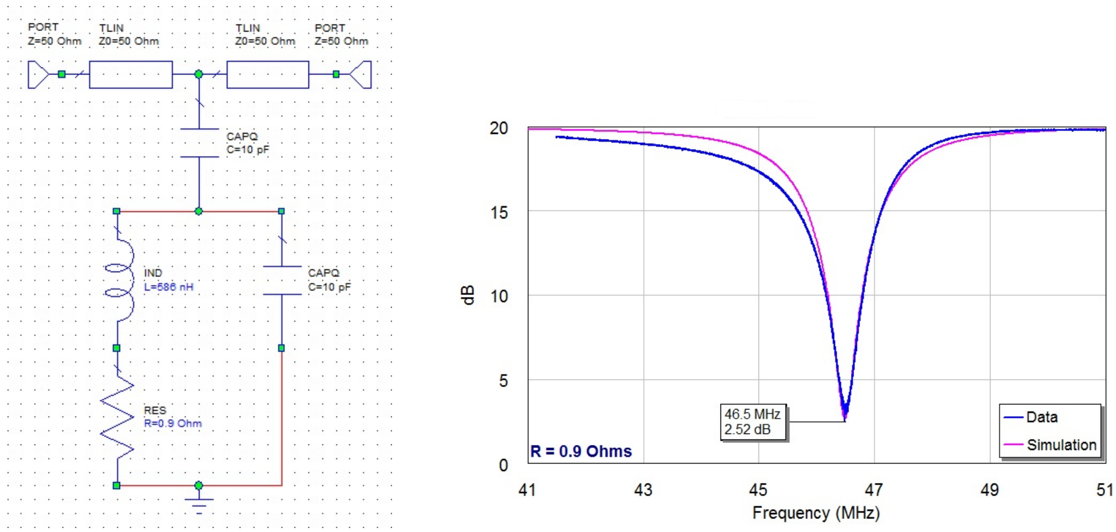

(a) (b)

Figure 20: (a) A schematic of SNRSPD1 made in Microwave Office. An effective series resistor is added in order to tune the resonance depth to find the internal resistance. (b) Raw S_{21} data and the matched simulation curve for SNRSPD1.

4.37 such that

$$L_K = \frac{1}{(2\pi f_0)^2 C_T}, \tag{5.1}$$

where f_0 is the resonant frequency of the pixel of interest as shown in Figure 19 and C_T is the total capacitance of the resonator. For SNRSPD1, the resonant frequency was found to be $f_0 = 46.5\text{MHz}$ and the total capacitance was $C_T = 20\text{pF}$ which gives $L_K = 586\text{nH}$. For SNRSPD2, the resonant frequency was found to be $f_0 = 93.1\text{MHz}$ and the total capacitance was $C_T = 4\text{pF}$ which gives $L_K = 731\text{nH}$.

5.1.4 Parasitic Resistance

An ideal superconductor has zero DC resistance when the device is at a temperature that is less than the critical temperature of the material. As mentioned previously, parasitic resistance can occur in forms such as bridging between meandered segments

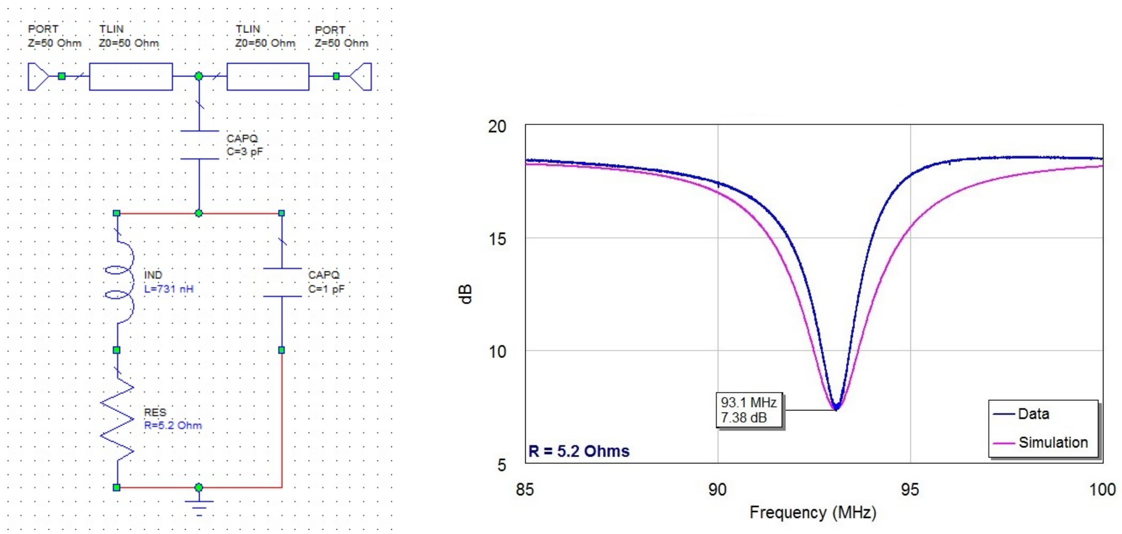

(a) (b)

Figure 21: (a) A schematic of SNRSPD2 made in Microwave Office. An effective series resistor is added in order to tune the resonance depth to find the internal resistance. (b) Raw S_{21} data and the matched simulation curve for SNSPDR2.

of the nanowire due to oxidation of the material or due to fabrication defects. This causes a lowering of the internal quality factor given in Equation 4.18. Figures 20 and 21 show the results of a simulation including an effective series resistance fit to the frequency data. For SNRSPD1, $R = 0.9\Omega$. For SNRSPD2, $R = 5.2\Omega$. The higher resistance for SNRSPD2 may be due to increased oxidization compared to SNRSPD1.

5.1.5 Quality Factors

Quality factors are important parameters for describing how resonators will behave in the presence of incident microwave, thermal, and optical power. Dissipated power and stored energy can be determined with respect to quality factors. An analysis of the quality factors of SNRSPD1 and SNRSPD2 can be done given Equations 4.11, 4.13, and 4.14.

For SNRSPD1: $f_0 = 46.5\text{MHz}$, $\Delta f_{3dB} = 2.00\text{MHz}$, $\omega_0 = 292\text{MHz}$, $L = 586\text{nH}$, $R = 0.9\Omega$, and $C_C = C_P = 10\text{pF}$. The quality factors are then found to be $Q_r = 23.3$, $Q_i = 190$, and $Q_c = 27.4$. For SNRSPD2: $f_0 = 93.1\text{MHz}$, $\Delta f_{3dB} = 2.50\text{MHz}$, $\omega_0 = 585\text{MHz}$, $L = 731\text{nH}$, $R = 5.2\Omega$, $C_C = 3\text{pF}$, and $C_P = 1\text{pF}$. Following the same procedure: $Q_r = 37.2$, $Q_i = 82.2$, and $Q_c = 30.4$. In both cases, the SNRSPD devices are coupling quality factor limited such that $Q_c < Q_i$ and $Q_r \sim Q_c$.

The period over which the resonator loses energy can then be calculated via Equation 4.19. For SNRSPD1, $\tau_r = 159\text{ns}$. For SNRSPD2, $\tau_r = 127\text{ns}$. Equation 4.25 can be used to calculate the dissipative part of the impedance and the reactive part. This is achieved by finding the real and imaginary components of the impedance. For SNRSPD1, $R = Re\{Z_r\} = 3.61\Omega$ and $X = Im\{Z_r\} = -1.90 \times 10^{-2}\Omega$. For SNRSPD2, $R = Re\{Z_r\} = 9.25\Omega$ and $X = Im\{Z_r\} = -3.75 \times 10^{-2}\Omega$.

5.1.6 Thermal Response

Measurements were made of the resonant frequency dependence as a function of base temperature as shown in Figures 22a and 23a. In order to analyze the thermal response, Equation 4.44 can be integrated as follows:

$$\begin{aligned}
&\int \frac{1}{f_0} df_0 = -\int \sqrt{\frac{\pi k}{2\Delta_0 T}} \left(\frac{\Delta_0}{kT} + \frac{1}{2}\right) e^{-\frac{\Delta_0}{kT}} dT \\
&\Rightarrow ln\left(f_0\right) = -\sqrt{\frac{\pi k T}{2\Delta_0}} e^{-\frac{\Delta_0}{kT}} + C \\
&\Rightarrow f_0 = De^{-\sqrt{\frac{\pi kT}{2\Delta_0}} e^{-\frac{\Delta_0}{kT}}},
\end{aligned} \tag{5.2}$$

where C and D are combined constants of integration.

Figures 22b and 23b show the data and the corresponding curve fit with respect to Equation 5.2. As Equation 5.2 is derived via Mattis-Bardeen theory, the curve

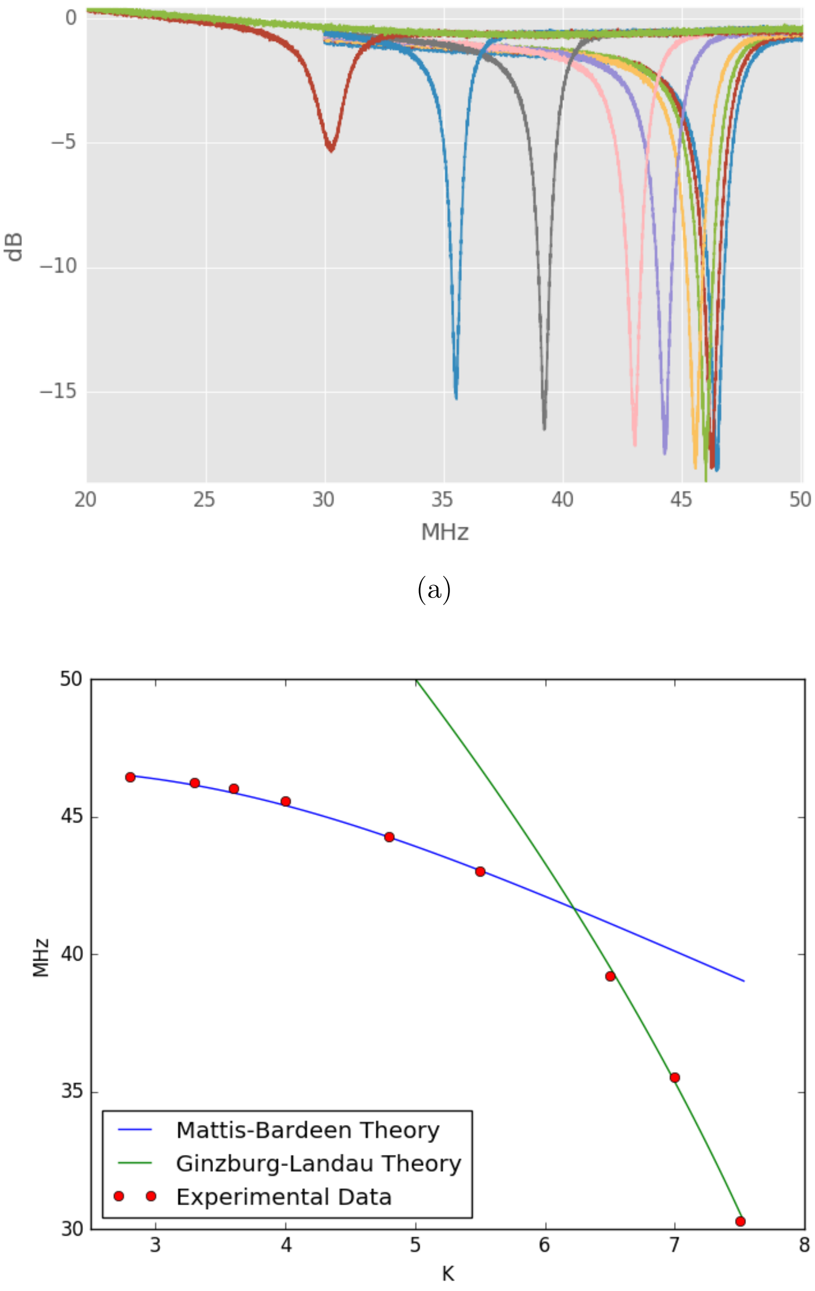

(a)

(b)

Figure 22: (a) S_{21} for varying base temperature values of the SNRSPD1 package. (b) Resonant frequency data as a function of base temperature with a curve fits based on the Mattis-Bardeen and Ginzburg-Landau theories of superconductivity.

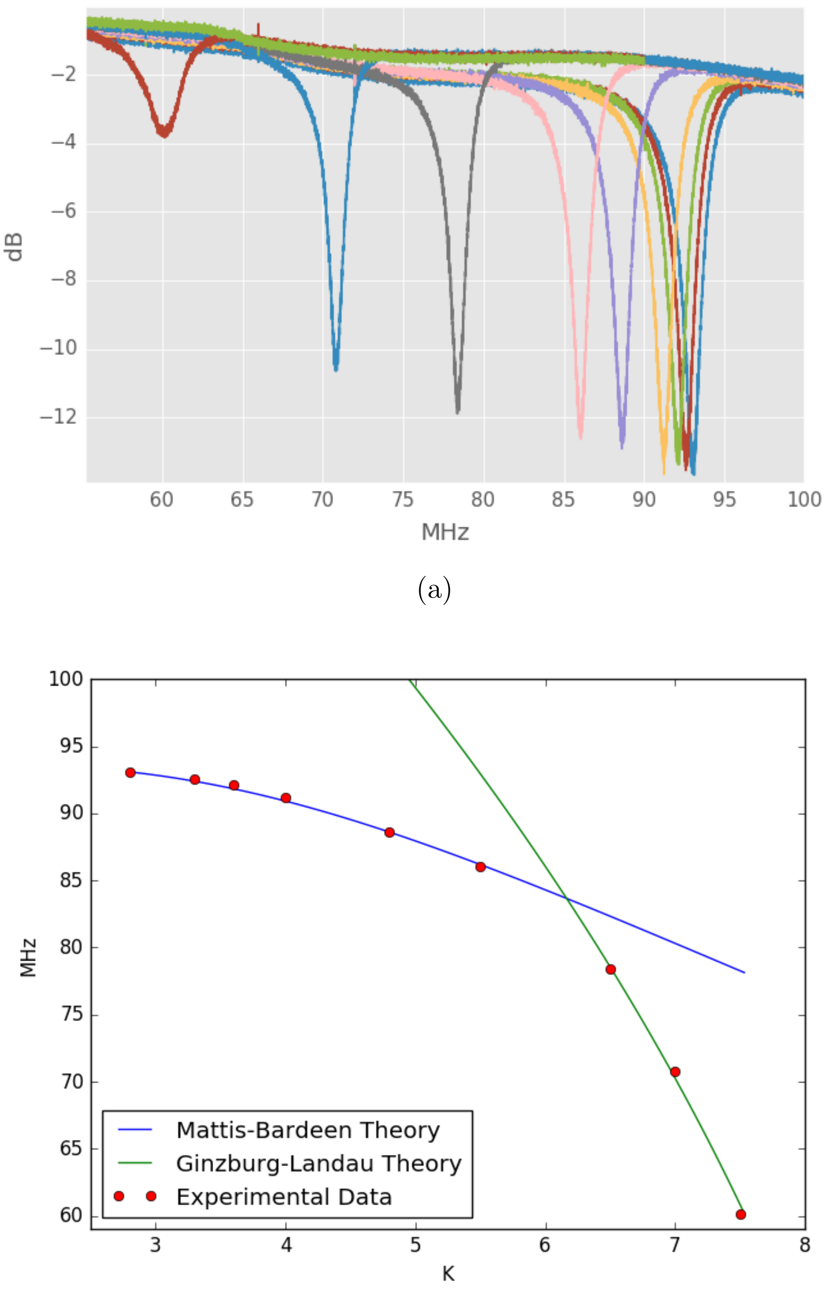

(a)

(b)

Figure 23: (a) S_{21} for varying base temperature values of the SNRSPD2 package. (b) Resonant frequency data as a function of base temperature with a curve fits based on the Mattis-Bardeen and Ginzburg-Landau theories of superconductivity.

is only valid at low temperatures. This is due to the anomalous skin effect upon which the theory is derived, where non-local electric fields effect charge carriers in a non-classical way (Aude 2010). Since the theory is based upon this effect, it breaks down as $T \rightarrow T_C$. The fits for both SNRSPD1 and SNRSPD2 agree with the result of the band-gap energy $\Delta_0 \approx 1.1$meV. Correspondingly, and according to Equation 1.35,

$$\Delta_0 \approx 1.764 k_B T_C, \tag{5.3}$$

such that the critical temperature is given by $T_C \approx 7.15$K.

For temperatures near the critical temperature, the data can be fit with Ginzberg-Landau theory. This is due to the theory being based on the behavior of a system near linear instability (Hohenberg and Krekhov 2015). At the phase transition from the normal state to the superconducting state, a macroscopic quantum wave function can be considered as an order parameter and expanded in order to be equated with the free energy density of the system. Since the theory is only valid near the critical point of the system, it breaks down as $T \rightarrow 0$.

The density of Cooper pairs as a function of temperature in Ginzberg-Landau theory is given by (A. J. Annunziata et al. 2010a)

$$n_{cp}(T) \approx n_{cp}(0) \left(1 - \frac{T}{T_C}\right). \tag{5.4}$$

The ratios of the kinetic inductance and density of Cooper pairs at some temperature T to the corresponding values at zero temperature are inversely related such that $L_K(T)/L_K(0) = n_{cp}(0)/n_{cp}(T)$. We can then write the kinetic inductance as

$$L_K(T) \approx L_K(0) \left(\frac{1}{1 - T/T_C}\right). \tag{5.5}$$

Plugging this into Equation 4.23, we obtain

$$f_0 = \frac{\sqrt{1 - T/T_C}}{2\pi\sqrt{L_K(0)(C_C + C_P)}}. \tag{5.6}$$

Fitting this curve to the data (Figures 22b and 23b), we find that both devices agree with a critical temperature value of $T_C = 9$K. This differs from the result given by Mattis-Bardeen theory and may be due to having a sub-optimal number of data points. Furthermore, we find values for the zero-point kinetic inductance of $L_{K1}(0) = 225$nH and $L_{K2}(0) = 285$nH. These values increase as a function of base temperature.

5.1.7 Non-Linear Kinetic Inductance Response

As discussed previously, the non-linear response of the kinetic inductance can be used to determine the characteristic current I_* for the given nanowire material and geometry. Equation 4.55 shows the relationship between the frequency shift as a function of current and I_*. Measurements were made of the resonant frequency dependence and are shown in Figures 24 and 25, where df_0/dI^2 is the slope of the curve. For SNRSPD1, the slope is $-31.3kHz/\mu\text{A}^2$. For SNRSPD2, the slope is $-65.9kHz/\mu\text{A}^2$. It follows that for $T = 2.80$K, $I_* = 27.3\mu$A for SNRSPD1 and $I_* = 26.6\mu$A for SNRSPD2.

5.1.8 Determination of the Density of States and Number of Quasiparticles

According to Swenson et al. (Swenson et al. 2013), the density of states at the Fermi Energy at a temperature T can be found by equating the scaling energy with the condensation energy of the superconductor:

$$L_K I_*^2 = \frac{1}{2}\Sigma N_0 \Delta_0^2, \tag{5.7}$$

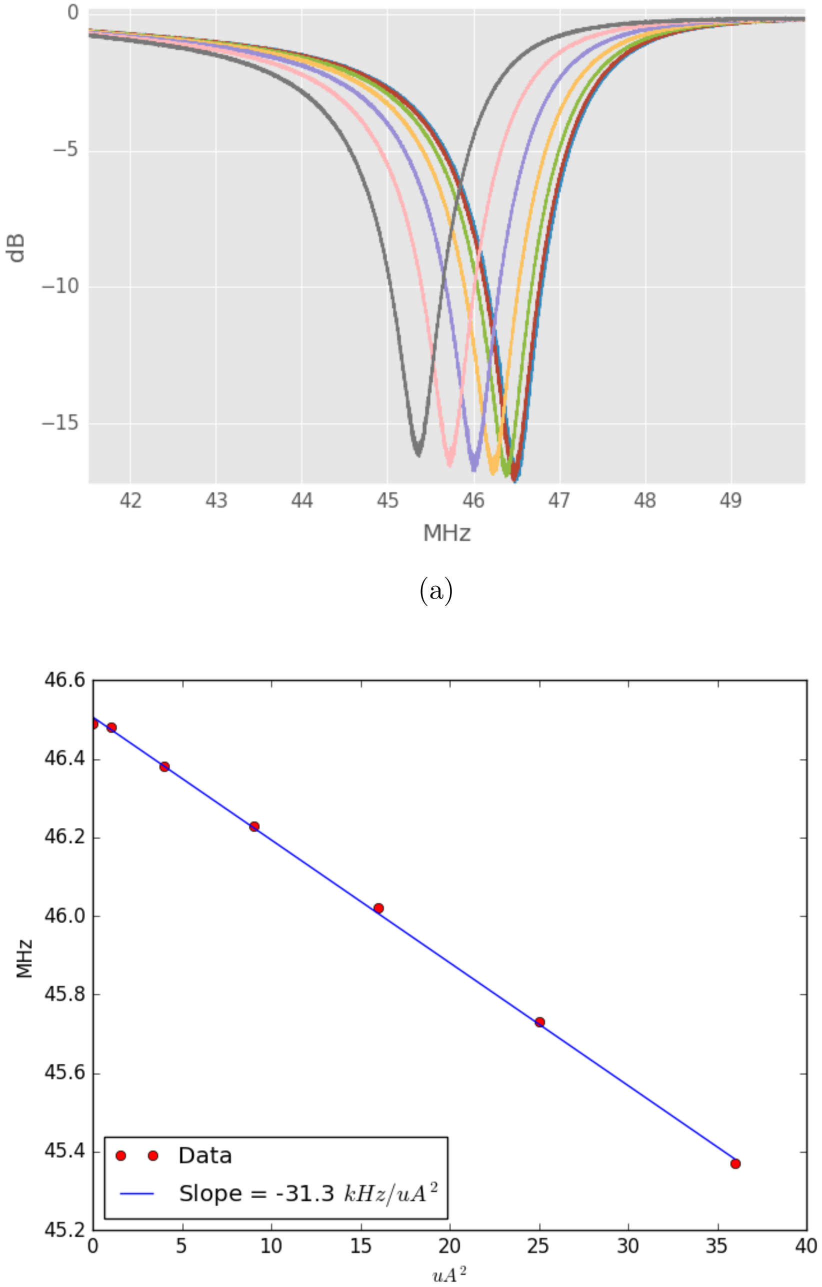

(a)

(b)

Figure 24: (a) S_{21} for varying DC bias values of the SNRSPD1 package. (b) Resonant frequency data as a function of DC bias squared with a linear curve fit.

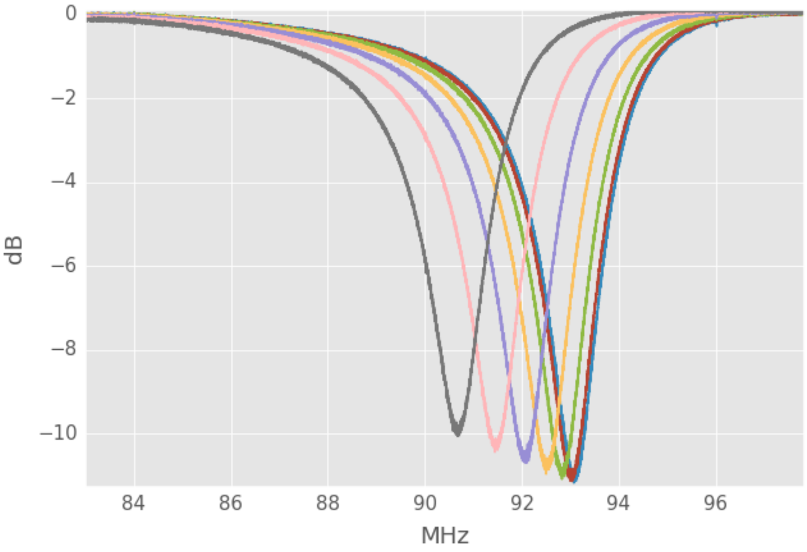

(a)

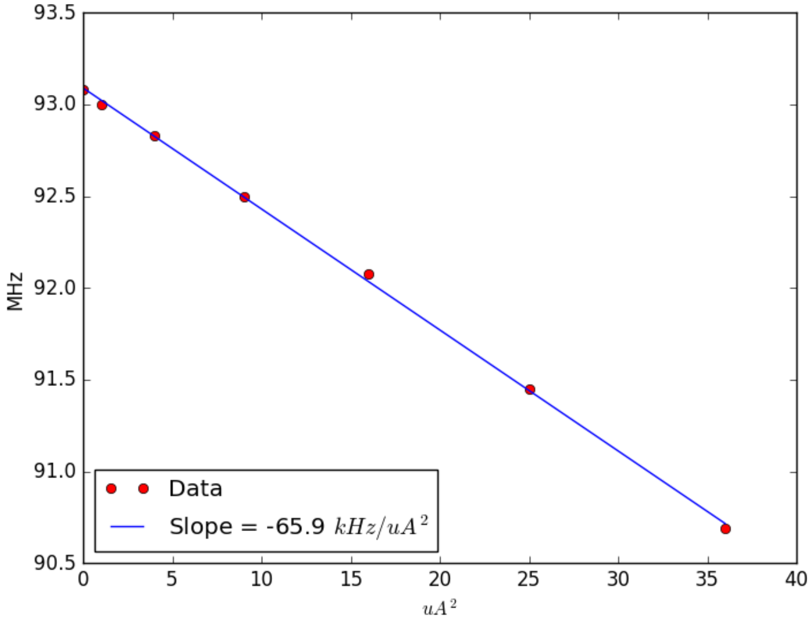

(b)

Figure 25: (a) S_{21} for varying DC bias values of the SNRSPD2 package. (b) Resonant frequency data as a function of DC bias squared with a linear curve fit.

where L_K is the kinetic inductance, I_* is the scaling current, Σ is the volume of the nanowire, and Δ_0 is the band-gap energy. The active surface area of the nanowire was estimated to be $71.65\mu\text{m}^2$ via drawings in Layout Editor. Given a thickness of $\sim$4nm, $\Sigma = 2.866 \times 10^{-19}\text{m}^3$.

Given the results from the previous sections for L_K, I_*, and Δ_0: $N_0 \approx 1.6 \times 10^{10}/\text{eV}/\mu\text{m}^3$ for SNRSPD1 and $N_0 \approx 1.9 \times 10^{10}/\text{eV}/\mu\text{m}^3$ for SNRSPD2. These values are comparable to the value $N_0 \approx 2.25 \times 10^{10}/\text{eV}/\mu\text{m}^3$ found by Smirnov et al. for a 5nm film thickness (Smirnov et al. 2016). The number of quasiparticle excitations as a function of base temperature can then be found with (Doyle et al. 2008)

$$N_{qp} = n_{qp} \times \Sigma, \tag{5.8}$$

where n_{qp} is given by Equation 3.15. Figure 26 shows N_{qp} as a function of base temperature for SNRSPD1 and SNRSPD2. At our operating temperature of 2.8K, $N_{qp} = 1.22 \times 10^5$ quasiparticles for SNRSPD1 and $N_{qp} = 1.44 \times 10^5$ quasiparticles for SNRSPD2.

5.2 Operation of a Superconducting Nanowire in Two Detection Modes: KID and SPD

As we have discussed, SNSPD devices are biased close to the switching current such that a single photon carries enough energy to drive a section of the nanowire normal and produce a countable voltage pulse. To operate an array of SNSPDs with this traditional approach, each device needs to be wired individually from cryogenic temperatures to a room temperature environment. This increases system complexity and heat load on the coldplate, resulting in higher power consumption. Implementing the nanowire in a resonant circuit allows the multiplexing scheme

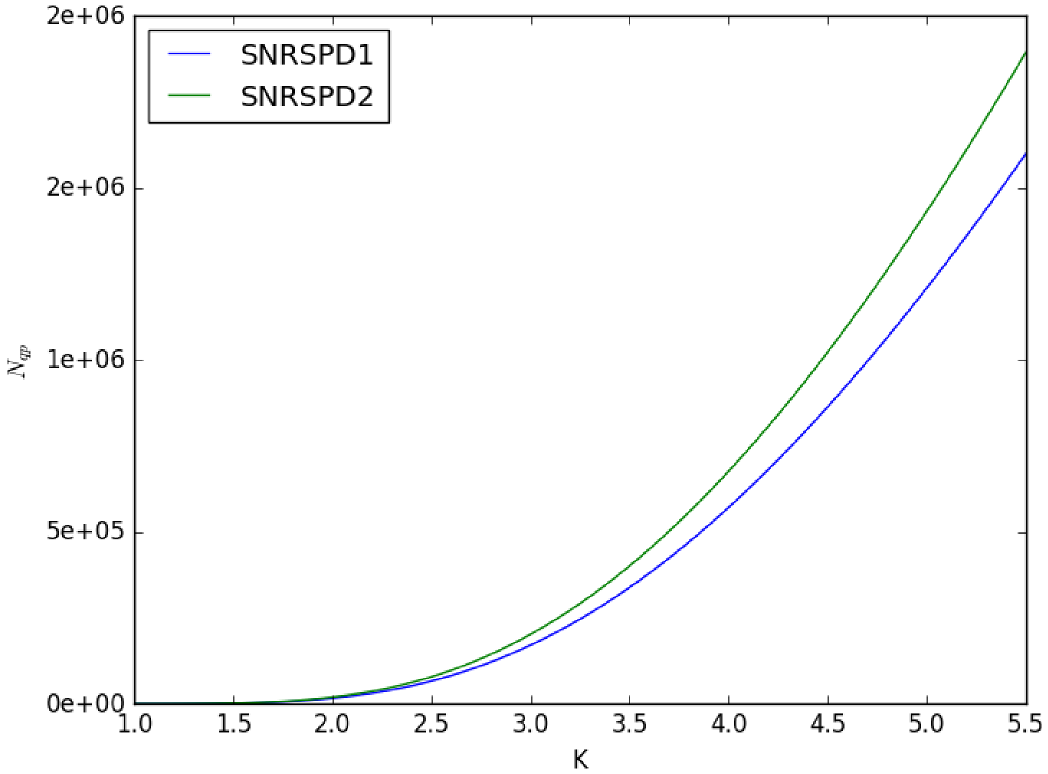

Figure 26: The number of quasi-particles present in the nanowire volume as a function of base temperature for SNRSPD1 and for SNRSPD2.

already well-developed for kinetic inductance detectors (KID) to be used. Since the capacitive portion of the resonant circuit is easily tuned and therefore the resonant frequency is easily varied, the resonant frequency of each pixel can be uniquely read out on the same feedline. Additionally, the resonators can be tuned by varying the dimensions of the nanowire (A. J. Annunziata et al. 2010b).

It is also possible to bias the nanowires with RF-power instead of DC (Doerner et al. 2016). Doerner et al. demonstrated an early two-pixel proof-of-concept for multiplexed SNSPDs biased with RF-power. Their resonant circuits consisted of coupling capacitors in addition to the inductive nanowires. More recently, an RF-biased 16-pixel array was developed and tested by this group. The pixels consisted of an coupling capacitor, a parallel resonator formed with a capacitor and an inductor, and the photo-sensitive nanowire (Doerner et al. 2017).

A time-tagged readout has been developed by coupling SNSPDs in an array with a superconducting delay line (Hofherr et al. 2013). This method involves the use of one bias supply for the whole chain and produces an effective temporal resolution of photon events. Another method for building a nanowire-based imager has been carried out based on a single superconducting nanowire that is read out at both ends (Zhao et al. 2017). This allows for the determination of the location along the wire and the time at which a single photon event occurred.

In this section we consider two modes of SNSPD operation: linear mode and Geiger mode. Linear mode detectors give a response proportional to fluctuations in absorbed power and include calorimeters such as transition edge sensors (TES), and KIDs. Given enough sensitivity and speed, these detectors can resolve individual photons and measure photon energy. Geiger-mode detectors such as photomultipliers or avalanche photodiodes are threshold detectors and produce uniform pulses in response to absorption of photons. We operate the nanowire in a resonant LC circuit as a KID (linear mode) with low-AC readout power and high-AC readout power. We also operate the nanowire with a DC current bias embedded in the resonant circuit and convert the ringing signal to a standard, countable pulse (Geiger mode).

5.2.1 Experimental Apparatus

A 1.3μm LED situated above the package with a copper bracket (Figure 27) was used to apply optical power and was biased with a Keithley 2400 series precision source

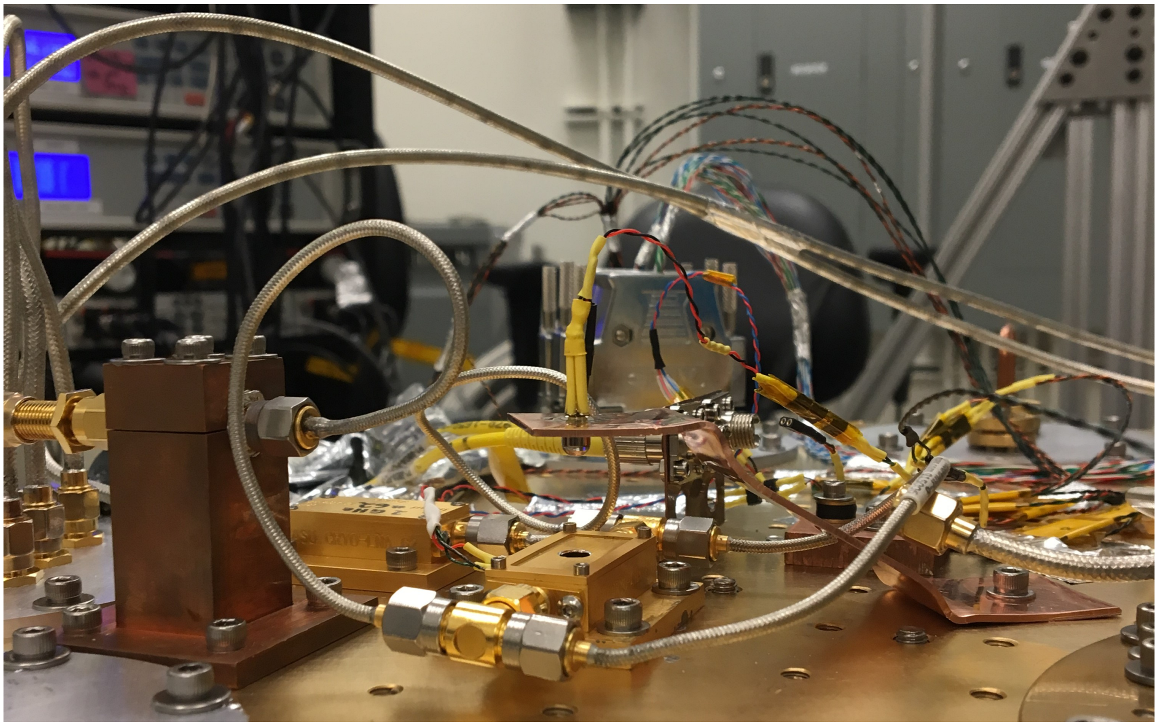

Figure 27: Free-space coupled detectors mounted inside the Sumitomo RP-082 cryostat on the coldplate.

measurement unit (SMU). The microwave response of the devices were read out with an Agilent E5072A vector network analyzer (VNA). In Geiger mode, the devices were biased with a temperature stabilized, battery operated, precision, constant current source made at ASU. The waveforms (Figure 28) were recorded using a Tektronix TDS 7104 oscilloscope and the pulses were counted using a Tektronix FCA 3100 frequency counter. Figure 29 shows how the experiment was set up outside and inside the cryostat.

5.2.2 Operation in Linear Mode

5.2.2.1 Standard Kinetic Inductance Detector

When operated in KID mode, the detectors are AC biased with tones at their resonant frequencies of 45.85 and 91.81MHz. We investigated the effect of two regimes of AC biasing. The first regime was a standard, low-current bias of the nanowire such that the critical current is never exceeded. In this regime, the nanowire remains superconducting under optical loading. The incident photons break Cooper pairs and a change in kinetic inductance results in a shift of the resonant frequency as shown in Figure 30a. A shift of 94 ± 7.51Hz/mA of LED current was measured. Above a few mA, the LED current is proportional to the emitted power.

Using the measured frequency shift, we can estimate the absorbed optical power by dividing by the responsivity as

$$\frac{df}{dP_{abs}} = \frac{df}{dN_{qp}} \frac{dN_{qp}}{dP_{abs}}, \tag{5.9}$$

where df is the frequency shift, dP_{abs} is the absorbed optical power, and dN_{qp} is the number of quasiparticles.

The shift in frequency due to a change in quasiparticle number density is given by (Gao et al. 2012)

$$\frac{df}{dN_{qp}} \cong \frac{-\alpha f_0}{4N_0\Delta_0} \frac{1}{\Sigma} \left(1 + \sqrt{\frac{2\Delta_0}{\pi k T}}\right), \tag{5.10}$$

where f_0 is the resonant frequency, $\alpha = 1$ is the kinetic inductance fraction, N_0 is the density of states at the Fermi level, Δ_0 is the band-gap energy, Σ is the volume of the superconducting nanowire, and T is the base temperature. For $f_0 = 45.87$MHz, $N_0 = 2.55 \times 10^{10}/\text{eV}/\mu\text{m}^3$ (Smirnov et al. 2016), $\Delta_0 = 1.1$meV, $\Sigma = 0.2866\mu\text{m}^3$, and $T = 2.7$K, the frequency shift with respect to the generation of a single quasiparticle is -4Hz/qp. The change in quasiparticle number density as a function of absorbed power is given as

$$\frac{dN_{qp}}{dP_{abs}} = \frac{\eta \tau_0}{\Delta_0}, \tag{5.11}$$

where η is the internal quasiparticle generation efficiency for absorbed optical power and τ_0 is the characteristic time constant of the material. τ_0 is estimated to be ~250ps-1.3ns based on the time it takes for the energy deposited by the absorbed photon to escape the nanowire (Smirnov et al. 2016). This relaxation time arises from the process of quasiparticle recombination into Cooper pairs and phonons. The phonons have the energy of the superconducting gap such that if they do not thermalize then the net effect should be to effectively increase the energy relaxation time to the phonon escape time modified by positive electrothermal feedback. For $\eta \sim 0.5$ and $\Delta_0 = 1.1$meV, the total number of quasiparticles changes by $\sim 1 - 6 \times 10^{-7}$/qp/eV.

The shift in resonant frequency as a function of absorbed power is then given as

$$\frac{df}{dP_{abs}} \approx 6 - 24 \times 10^{-7} \frac{\text{Hz}}{\text{eV s}}, \tag{5.12}$$

where since the measured shift is 94Hz/mA, the absorbed power per mA is $0.4 - 2 \times 10^{8}$eV/mA/s. Each photon at the the operating wavelength of 1.3μm has an energy of ~ 0.95eV such that for the standard KID mode we arrive at a photon absorption rate per mA of LED current of

$$\Gamma_{stan} \approx 0.4 - 2 \times 10^{8} \frac{\text{photons/s}}{\text{mA}}. \tag{5.13}$$

5.2.2.2 Critical Kinetic Inductance Detector

The second regime of operation was a high-current bias of the nanowire. In this regime, the resonant frequency is not only shifted, but the signal also changes in amplitude as shown in Figure 30b. This effect is due to the averaging of two states of the resonator. The first state is when the AC bias amplitude is below the critical current and the incident photons act only to change the kinetic inductance and shift the resonant frequency. The second state is a normal state that occurs when a photon acts to drive the nanowire normal as the AC amplitude approaches the critical current.

The fraction of time spent in the normal state can be determined by analyzing the dependence of the change in amplitude of the resonance on the change in current in the LED. For LED currents from 0 to 50mA, the resonator amplitude rises from ~ -16.00dB to ~ -15.93dB. This corresponds to amplitude scale factors of 0.15848 and 0.15977, respectively. Performing the weighted average,

$$0.15977 = \frac{t_{norm}}{T} + 0.15848\Big(1 - \frac{t_{norm}}{T}\Big), \tag{5.14}$$

where t_{norm} is the time spent in the normal state and T is the total time of the measurement, the fractional time spent in the normal state was found to be 3×10^{-5}/mA. The pulse recovery time is approximately 200ns so that the photon count rate where an incident photon causes the resonator to switch to the normal state for the critical KID mode is

$$\Gamma_{crit} \approx 150\frac{\text{photons/s}}{\text{mA}}. \tag{5.15}$$

This corresponds to a detection efficiency of approximately 4×10^{-6} of the absorbed photons as estimated from the frequency shift.

5.2.3 Operation in Geiger Mode

When operated as an SPD in Geiger mode, the resonators were DC-biased through cryogenic bias tees and each photon produced a sharp voltage step followed by a ringdown signal at the resonant frequency of the detector. This signal was converted to a standard pulse with an envelope detector.

Geiger mode detection of photons has a few key advantages over linear mode operation, with one being the availability of higher operating temperatures. SNSPD devices need to satisfy the requirement of operating below the critical temperature of the material they are fabricated from. For NbN, this critical temperature can be as high as 16 K (Suzuki, Baba, and Anayama 1987). KIDs generally require sub-Kelvin operating temperatures in order to be sensitive enough to overcome the inherent noise in the superconducting film.

Another advantage of Geiger mode is the existence of an in-built noise filter in the form of the threshold detection of photons with a given energy. Also, an in-built amplification of the single photon signal is brought about by the cascading effect of the hotspot into a normal region of metal. It is therefore more straightforward to detect single photons in this mode.

At a fixed temperature, the detectors were biased with DC and were illuminated by a 1.3μm LED. When a photon is incident on the nanowire, a fast voltage step occurs. Since the nanowire is embedded in a resonant circuit, the signal rings down at the resonant frequency of the detector as shown in Figure 31a. The pulses that ring down were rectified with an analog circuit and converted to a standard pulse with an envelope detector. These pulses were counted with a frequency counter and the resulting count rate as a function of LED power is shown in Figure 31d for a device DC bias of 5μA. The photon count rate per mA of LED current for SPD mode is determined to be

$$\Gamma_{SPD} \approx 10^6 \frac{\text{photons/s}}{\text{mA}}. \tag{5.16}$$

This corresponds to a detection efficiency of approximately 2.5% of the absorbed photons.

5.2.4 Discussion

In this section, we have investigated three modes of detection: standard KID, critical KID, and SPD. The frequency shifts for the low-current bias and the high-current bias KID modes were approximately the same. The predominant effect of the high-current bias was a decrease in amplitude as the power incident on the device was increased. This indicates that some of the time the resonator was switching to normal and transmitting the AC signal.

The relative efficiency of AC bias mode to DC bias mode can be estimated by calculating the average of the product of the time-dependent AC current with the corresponding current dependent count rate. In the case where the internal quantum efficiency is a very steep function of current near the critical current, this can be approximated as an effective fraction of time where the current is above the threshold for efficient photon detection.

The bias currents used in this investigation for single photon counting in critical KID mode and SPD mode were approximately 95% of the critical current. We note that these bias currents may not have been optimal for sensitivity and that further experimentation should be executed in order to definitively declare superior sensitivity with a DC bias. However, in our analysis, when compared to DC biasing in SPD mode, AC biasing in critical KID mode had a much lower quantum efficiency due to the small fraction of time spent near the critical current of the superconducting nanowire. We therefore concluded that it was desirable to focus our future efforts on the multiplexing of nanowire arrays with a DC bias. These efforts are discussed in Chapter 6.

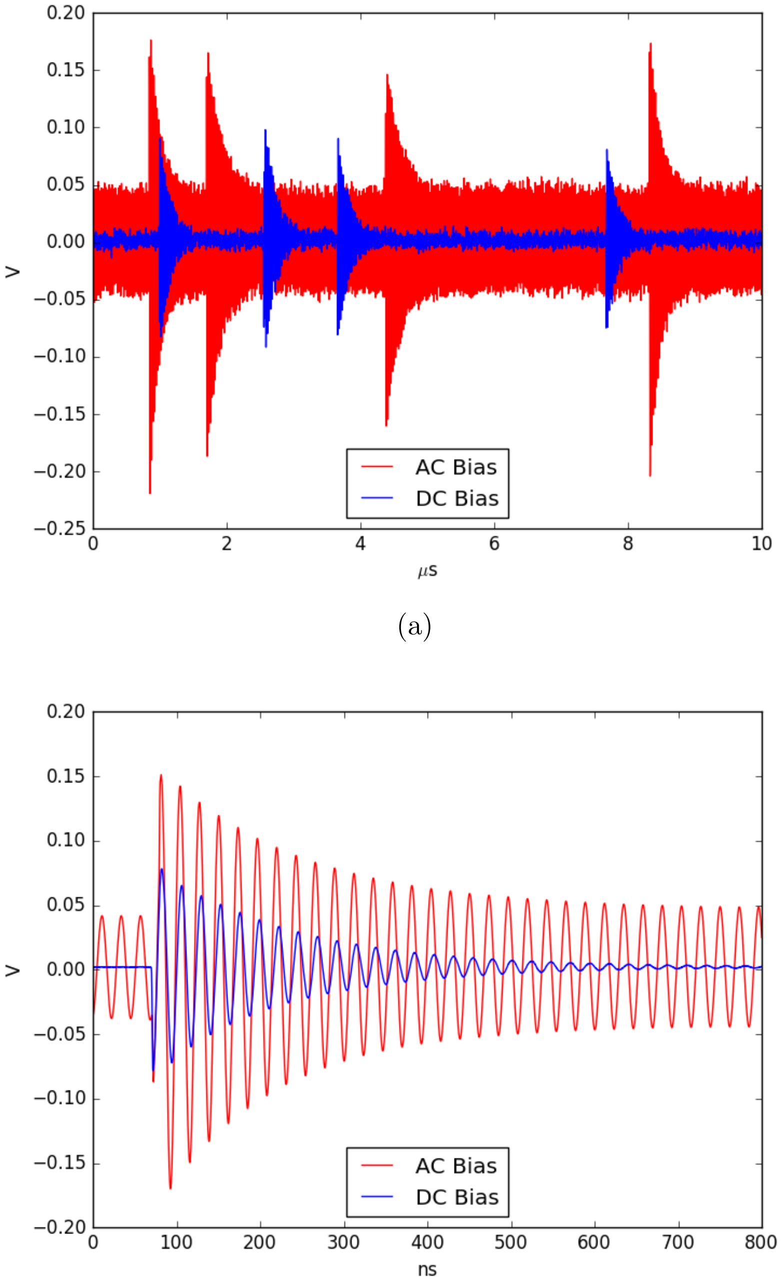

(a)

(b)

Figure 28: (a) Snapshot of the AC (red) and DC (blue) single photon pulses in a 10 μs span recorded on the oscilloscope. Due to a lower quantum efficiency, the required AC bias is greater than the required DC bias to achieve the same rate of pulse events. (b) Averaged single photon pulses.

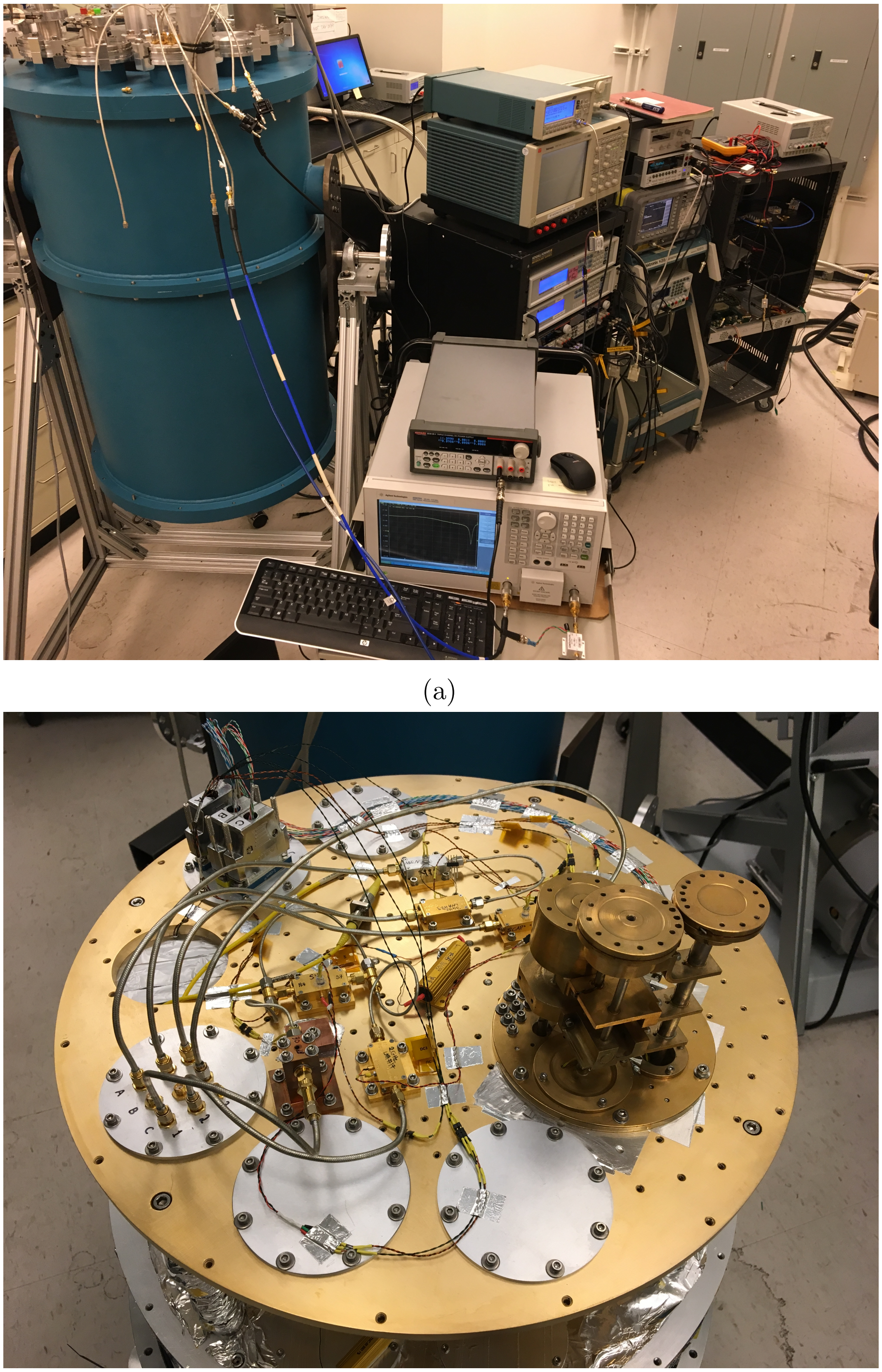

(a)

(b)

Figure 29: (a) Typical experimental setup for counting photons and measuring S-parameters. (b) Assembled RF circuit on the coldplate.

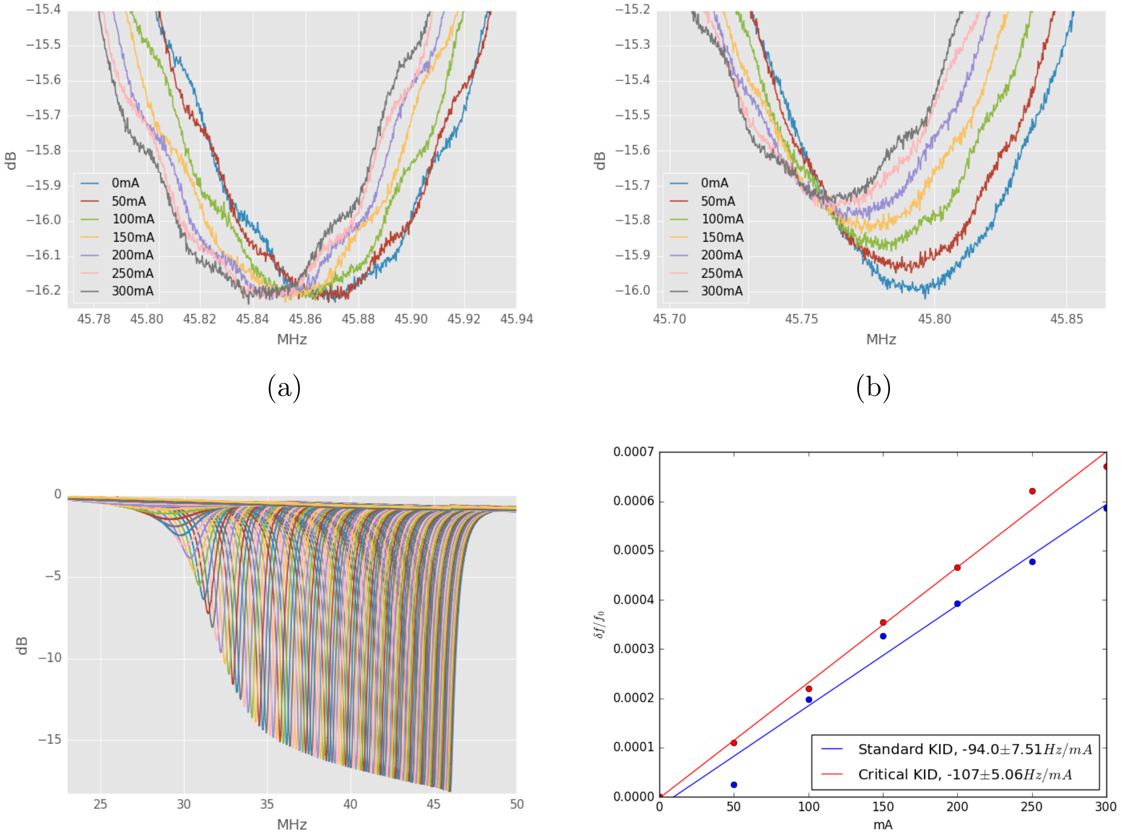

(a) (b)

(c) (d)

Figure 30: (a) S_{21} resonance shift as a function of LED current for the standard KID mode. (b) S_{21} resonance shift as a function of LED current for the critical KID mode. (c) Thermal response of the transmission from the superconducting state at 2.7K to the normal state. (d) Shifts of 94.0 ± 7.51Hz/mA and 107 ± 5.06Hz/mA are measured for the standard KID and critical KID mode.

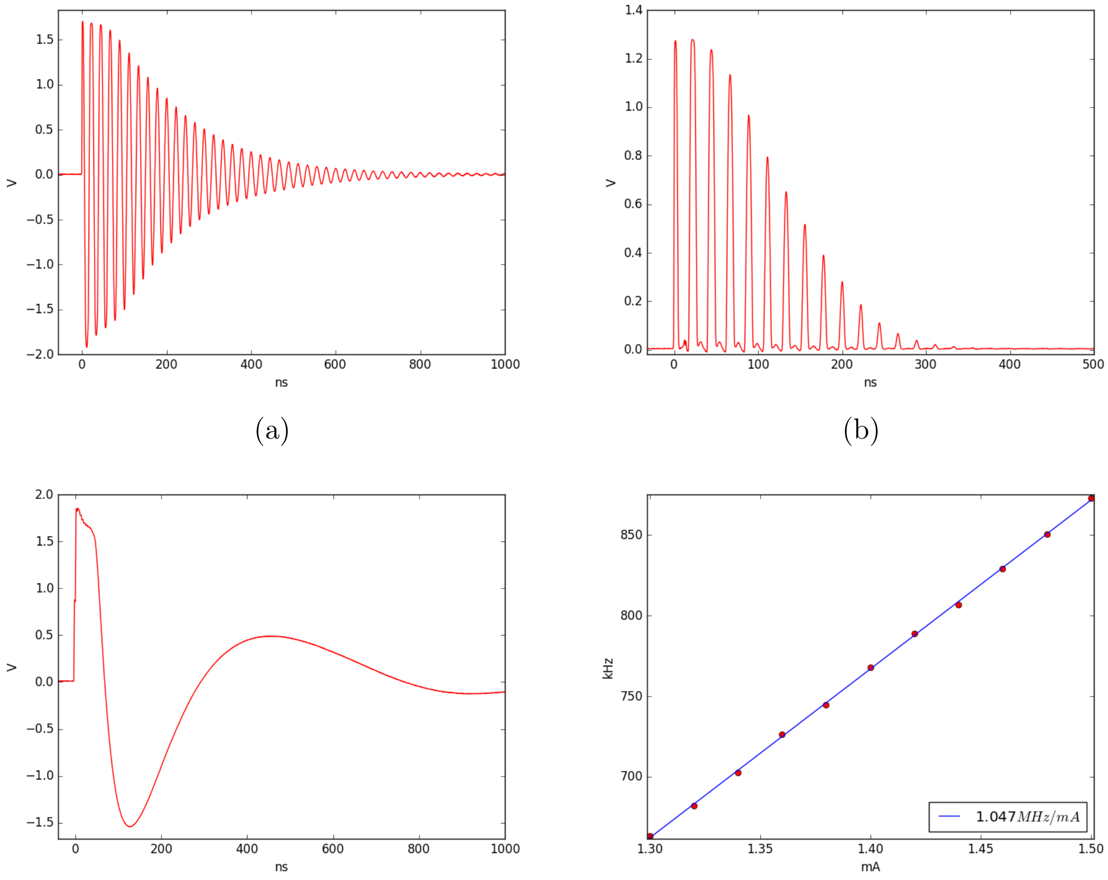

(a) (b)

(c) (d)

Figure 31: (a) Amplified and averaged waveform produced by a single-photon incident on the nanowire and traveling through the 10pF coupling capacitor. (b) Rectified waveform produced by a diode. (c) Filtered pulse produced by an RC-circuit. (d) Count rate as a function of LED current bias.

Chapter 6

DEVELOPMENT OF AN SNRSPD IMAGER ARRAY

In this chapter, we describe simulations of a DC-biased, frequency-multiplexed readout of superconducting nanowire single photon detectors (SNSPD) in Advanced Design System (ADS), LTspice, and Sonnet. We address issues of latching for designs with low capacitance, interdigital capacitors. We suggest a solution to latching involving a parallel-plate capacitor design. A multiplexing factor of 100 is achievable with a total count rate of > 5MHz. This readout could enable a 10000-pixel array for astronomy or optical communications. Additionally, we present a prototype array design based on lumped element components. An early implementation of the array is presented.

6.1 Simulations of a DC-Biased Frequency Multiplexed Nanowire Array

6.1.1 Motivation

Superconducting nanowire devices are useful for applications that require fast detection of photons. As previously discussed, one difficulty with SNSPDs is that they are not easily multiplexed for reading out large imaging arrays. A solution is multiplexing in the frequency-domain. This can be achieved by embedding the nanowires as the inductive components of resonant circuits that are embedded along a single transmission line. It was shown in Chapter 5 that AC biasing is inferior to the sensitivity achieved by DC biasing due to the small fraction of time spent near the critical current with an AC bias.

6.1.2 Concept

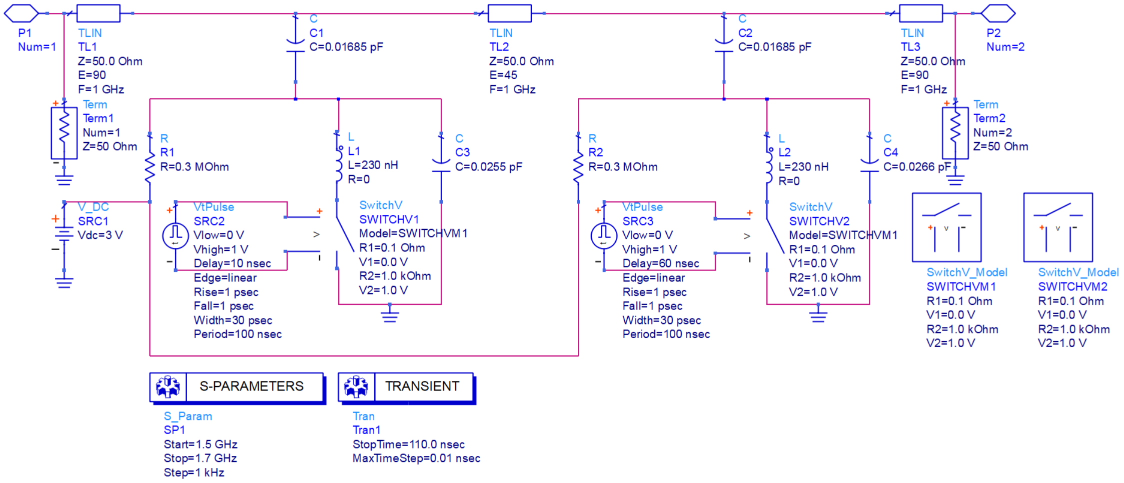

Figure 32: ADS layout of two SNRSPD pixels.

We have simulated a two-pixel, DC-biased array of frequency multiplexed SNSPDs in Advanced Design System (ADS) as shown in Figure 32. Both nanowires were modeled as ideal 230nH inductors. Both coupling capacitors were 0.01685pF. The parallel capacitors were 0.0255 and 0.0266pF. These superconducting nanowire resonator single photon detectors (SNRSPD) can be DC-biased with 10μA of current along a single line with a 3V source and 0.3MΩ resistors in series with each pixel. In this simulation, the resonant frequencies were 1.592 and 1.612GHz ($\Delta f_0 = 20$MHz) as shown in Figure 33a.

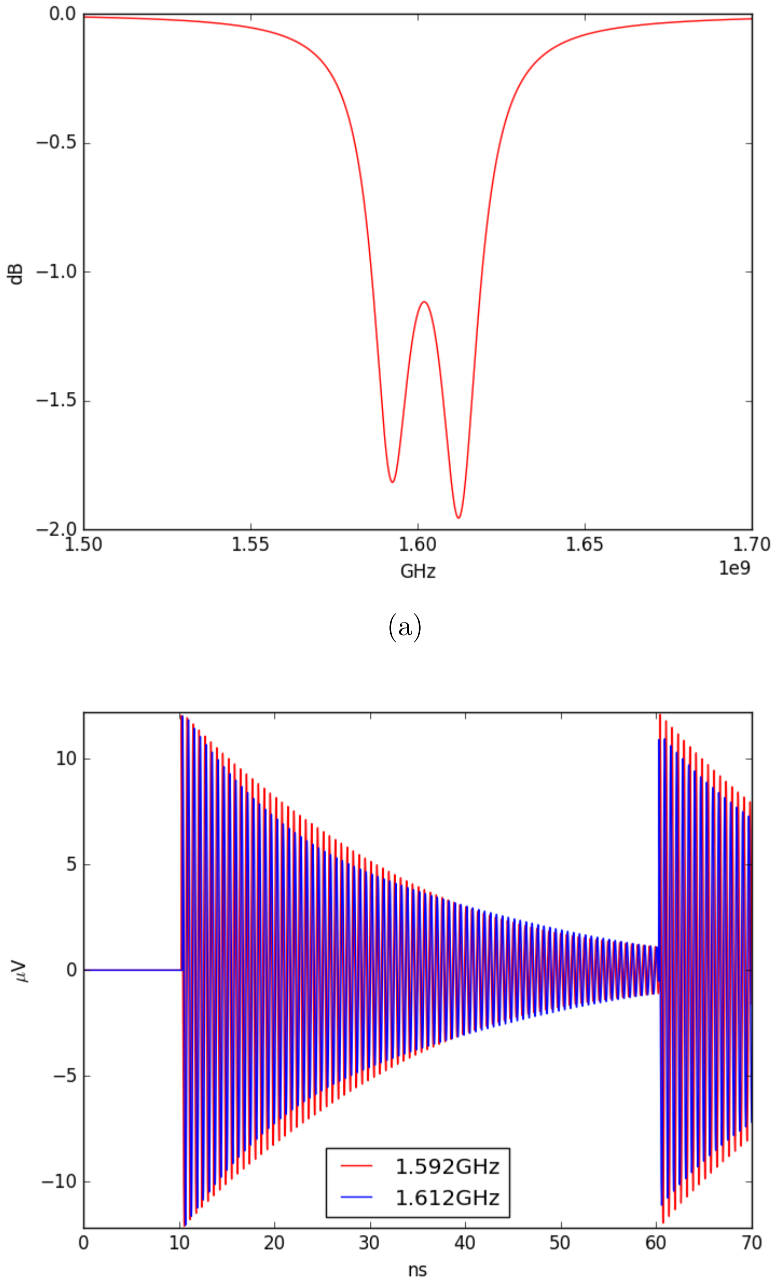

(a)

(b)

Figure 33: (a) ADS simulation of two pixels showing resonances at 1.592 and 1.612GHz. (b) The ringing transient pulses of the two pixels.

In the superconducting state there is applied DC, but zero voltage. When a photon is incident on the nanowire, there is a sharp voltage pulse with a ringdown signal at the resonant frequency of the resonator that was hit as shown in Figure 33b. This response was simulated in ADS with a voltage controlled switch that switched between resistances of 0.1Ω and $1\mathrm{k}\Omega$, which is the resistance that an incident photon in the presence of DC is expected to produce by driving a section of the nanowire normal through hot-spot production and the exceeding of the critical current. The rise and fall times of the pulses were set to 1ps. The width of the pulses were set to 30ps.

This setup allows for the multiplexing of SNSPDs because we are conditioning the pulse shapes from each detector to be unique in ringdown frequency. These unique signals reveal where each photon hit along the array. With all of the pixels on the same transmission line and amplifiers on either end, the arrival time of each photon can be determined.

6.1.3 Sonnet Design & Simulation

We have simulated a proof-of-concept, 16-pixel array of frequency-multiplexed SNSPDs in Sonnet. The nanowires were made of 4nm thick NbN with a kinetic inductance of $L_K = 55.0\mathrm{pH}/\Box$. The interdigital capacitors were made of a lossless planar metal. The substrate was made of 500μm thick Sapphire with a dielectric constant of 11.5 along the z-axis. The resonant frequencies ranged from $1.814 - 2.134$GHz with an average separation of $\Delta f_0 = 22$MHz.

The interdigital coupling capacitor was designed with a finger width of 250nm and a length of 3.680μm. The interdigital parallel capacitor was designed with a finger width of 250nm and a length of 7.360μm. The gap width was 250nm for both

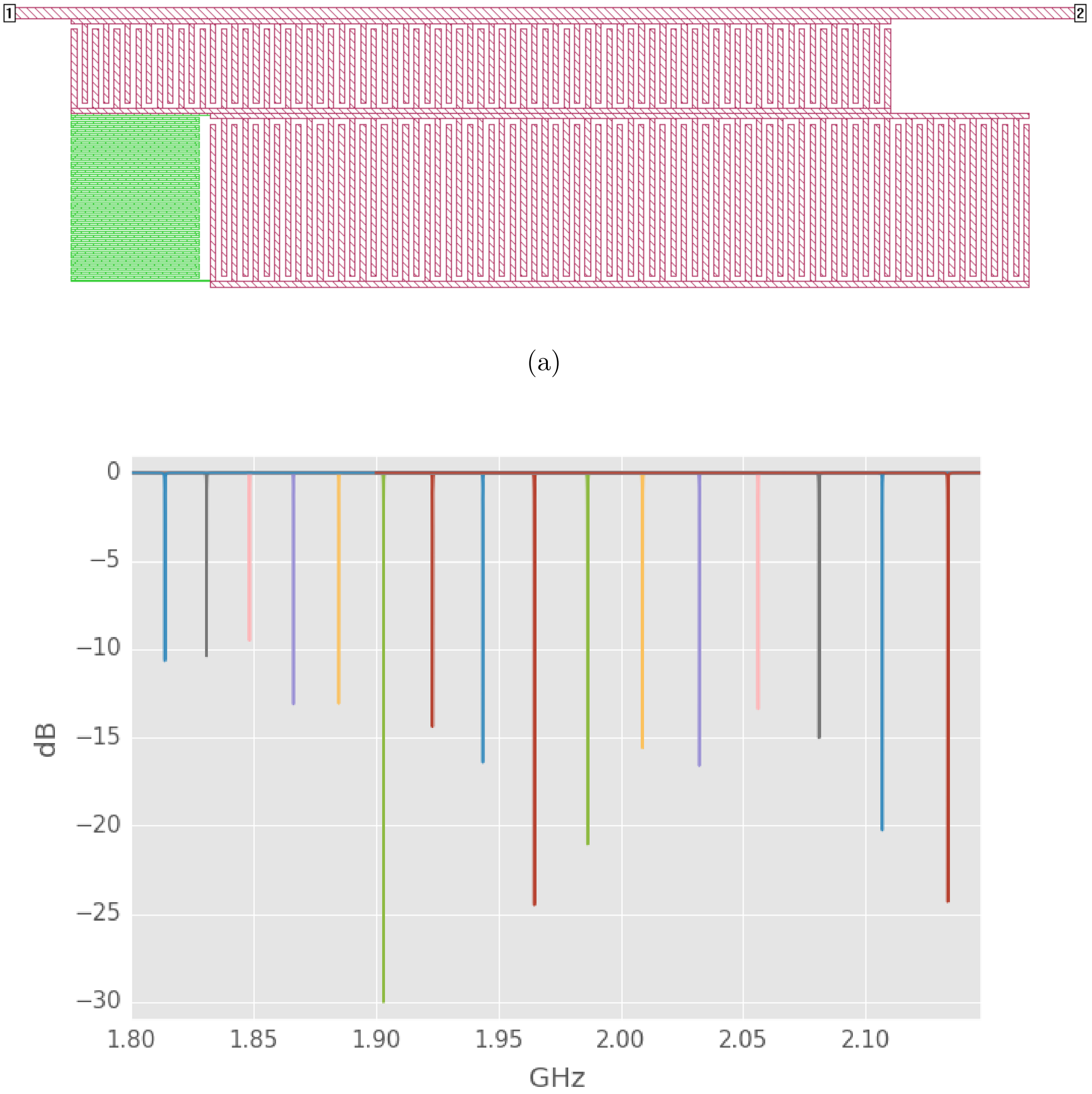

(a)

(b)

Figure 34: (a) Sonnet layout of the pixel that produces a resonance at 2.134GHz. The nanowire is green and the interdigital capacitors are purple. (b) The resonances of each pixel in the 16-pixel array.

capacitors. To tune the resonant frequencies to be separated by ~ 22MHz, the number of fingers of the coupling capacitor and the parallel resonator capacitor was sequentially reduced by two. Effects from the fringing fields prevented a design that is easily tuned by omitting one finger at a time. This configuration allows for a 100-pixel array in the span of $1 - 3$GHz. This frequency span may be shortened by implementing a fractional finger cutting scheme.

Given a fixed nanowire inductance and a variable parallel capacitor, the addition of a coupling capacitor allows for the adjustment of the coupling Q and the resonant frequency independent of each other. If we are coupling Q dominated, then the total Q can be adjusted to accommodate a desired resonance bandwidth. The bandwidth determines the ringdown time of the single photon pulses. As the bandwidth increases, the ringdown time becomes smaller. Therefore, the bandwidth limits the maximum achievable count rate of each detector.

The ringdown time is given as

$$\tau_{ring} = \frac{Q_r}{2\pi f_0}, \tag{6.1}$$

where Q_r is the resonator quality factor and f_0 is the resonant frequency. Astronomical applications require count rates on the order of 1MHz. In order to achieve a count rate of $1 - 5$MHz, an upper-bound ringdown time of $\tau_{ring} = 200$ns is required. This ringdown time corresponds to a resonance bandwidth of 5MHz. For resonators with resonant frequencies from $f_0 = 1 - 3$GHz, this corresponds to $Q_r = 1257 - 3770$. This range of quality factors can be achieved by scaling the coupling capacitor appropriately.

6.1.4 The Problem of Latching

The above analysis did not account for latching within our design and a model developed in LTspice (Berggren et al. 2018) shows that it latches. Latching occurs because there is no alternate DC path for the current in the nanowire when it goes normal. Whether it latches or not depends on if there is somewhere for the DC current to be stored while the nanowire becomes superconducting again. Implementing a large capacitor will act like a lower shunt impedance that will prevent latching. If the capacitor is big enough it will permit charge to be temporarily stored on it long enough for the nanowire to reset.

It has been found that a count rate of 500MHz is possible with a nanowire inductance of 125nH, a capacitor size of ∼0.75pF, and 2.5kΩ resistor. A 0.75pF interdigital capacitor (∼1cm^2) is unreasonably large with respect to an array of nanowires. Since we need relatively low Q, we may use a parallel plate capacitor with superconducting contacts and a silicon dioxide insulator (400nm thickness) to achieve a capacitance of 0.75pF with $\epsilon = 3.9$. This would result in $A_{cap} = 100 \times 100\mu\text{m}^2$.

6.1.5 Readout Development

A possible hardware implementation for an array in the span of 1-3GHz would use a two-channel 2 GSPS analogue-to-digital converter (ADC), microwave filters and splitters, a Schmitt trigger, and an FPGA development board with an RF input. A reflectionless filter would be used as a diplexer to split the low frequency oscillatory component from the high frequency rising edge. The oscillatory signal will be sent to the ADCs for frequency demultiplexing while the rising edge will be sent to the low jitter RF input of the FPGA for time tagging. After leaving the high-pass filter port of the diplexer the rising edge is sent to a Schmitt trigger to extend the pulse to meet the setup and hold requirements of the FPGA. For the low-pass signal, another splitter (or diplexer) will be used to split the signal between the two ADCs. With bandpass filters from 1-2 and 2-3 GHz the ADCs will be sampling in Nyquist zones 2 and 3. Combining the information gained from these three inputs will provide high timing resolution along with a capability of reading out large arrays.

A preliminary firmware design would implement a matched filter, a parallel fast Fourier transform (FFT), a threshold detector, a TDC, and a data packetizer. The matched filter would allow the low passed signal envelope to be used in signal discrimination and reduce the amplitude of out of band signals. After passing through the matched filter, a parallel FFT of length equal to twice the number of pixels will sample the data and deliver an update of each frequency bin every clock cycle. The magnitude squared of each frequency bin is calculated using a piecewise approximation of a squaring function (hardware efficient). The positive and negative frequency bins are added. A decision block will determine which bin has the largest magnitude every cycle. This output will be latched into the data packetizer along with the output from the time-to-digital converter (TDC) channel then sent to the data acquisition computer. To keep the high timing resolution of the pulse's rising edge, a TDC would also be implemented in the FPGA. Calibrated delay lines would provide the highest resolution possible.

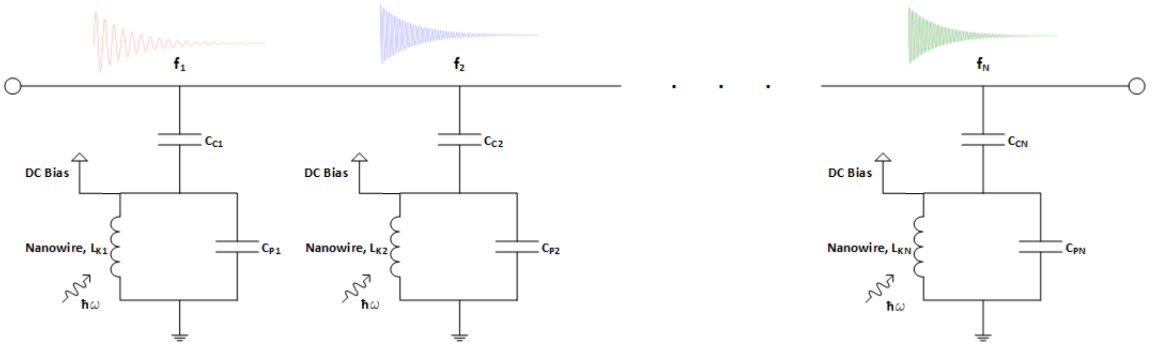

Figure 35: Diagram of SNRSPD array circuits. Incident photons of energy $\hbar\omega$ in conjunction with a common DC bias between pixels on the same feedline results in a frequency multiplexed readout with unique signatures based on designed varying resonant frequencies alone the line.

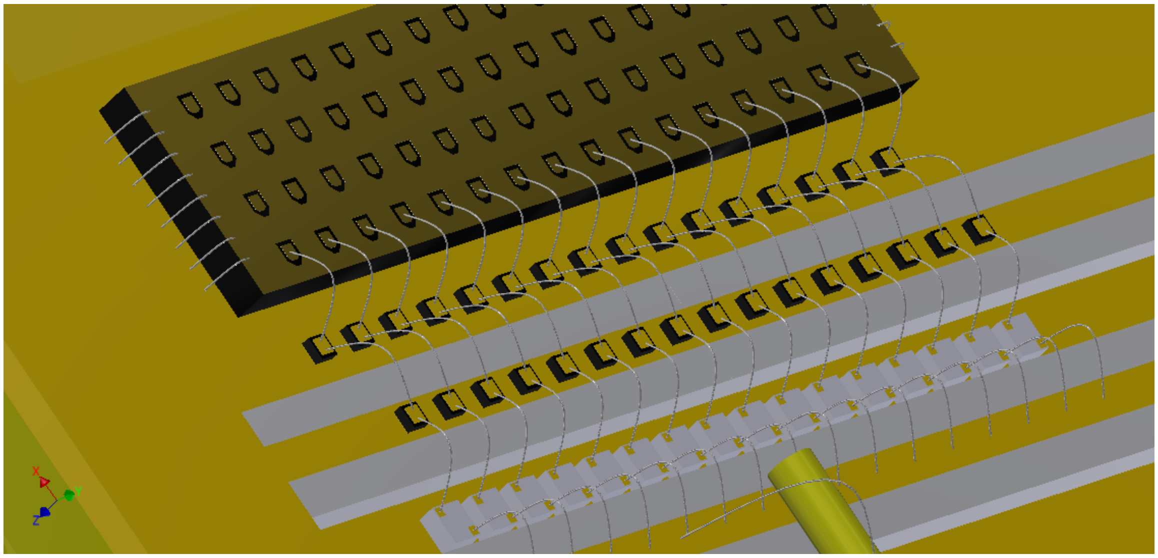

Figure 36: Autodesk Inventor drawing showing the the 16-pixel array. A pin connected to a 50Ω line is used to feed current to each SNRSPD using lumped element resistors. Each SNRSPD has two associated capacitors.

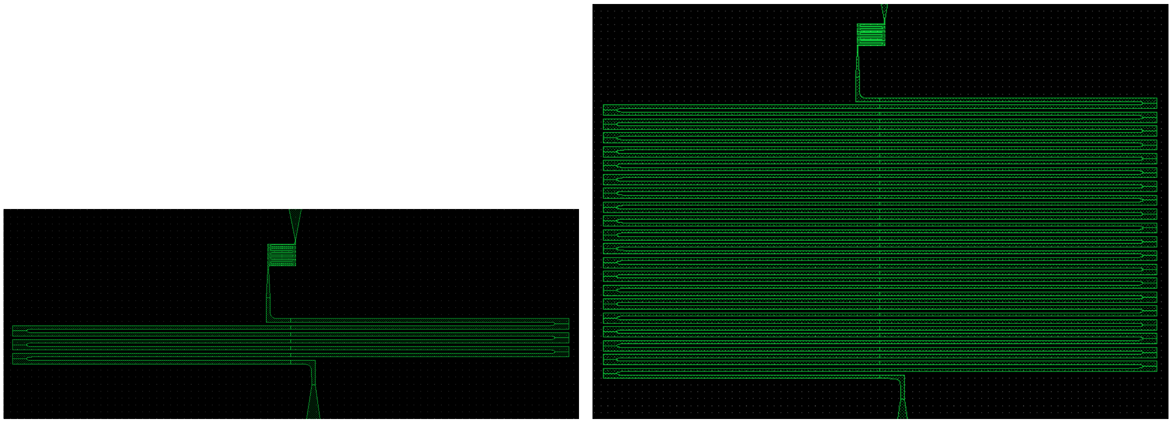

(a) (b)

Figure 37: Drawings of the nanowire and serial inductor for the lowest and highest inductances in the array: (a) ∼110nH (b) ∼521nH. The nanowires are consistently ∼35nH across the array.

6.2 Implementation of a DC-Biased Frequency Multiplexed Nanowire Array with Surface Mount Device Components

6.2.1 Setup

6.2.1.1 SNRSPD Package

A prototype with large, lumped element capacitors (∼pF) was developed to test the concept of DC-biased frequency-multiplexed SNSPD devices. Figure 35 shows a diagram of the prototype layout. Figure 36 shows an assembly drawn in Autodesk Inventor with a preliminary design for the prototype. To source current to the devices, a 50Ω line is attached to a DC pin via an aluminum 1mil bond wires. Sixteen 2.5kΩ

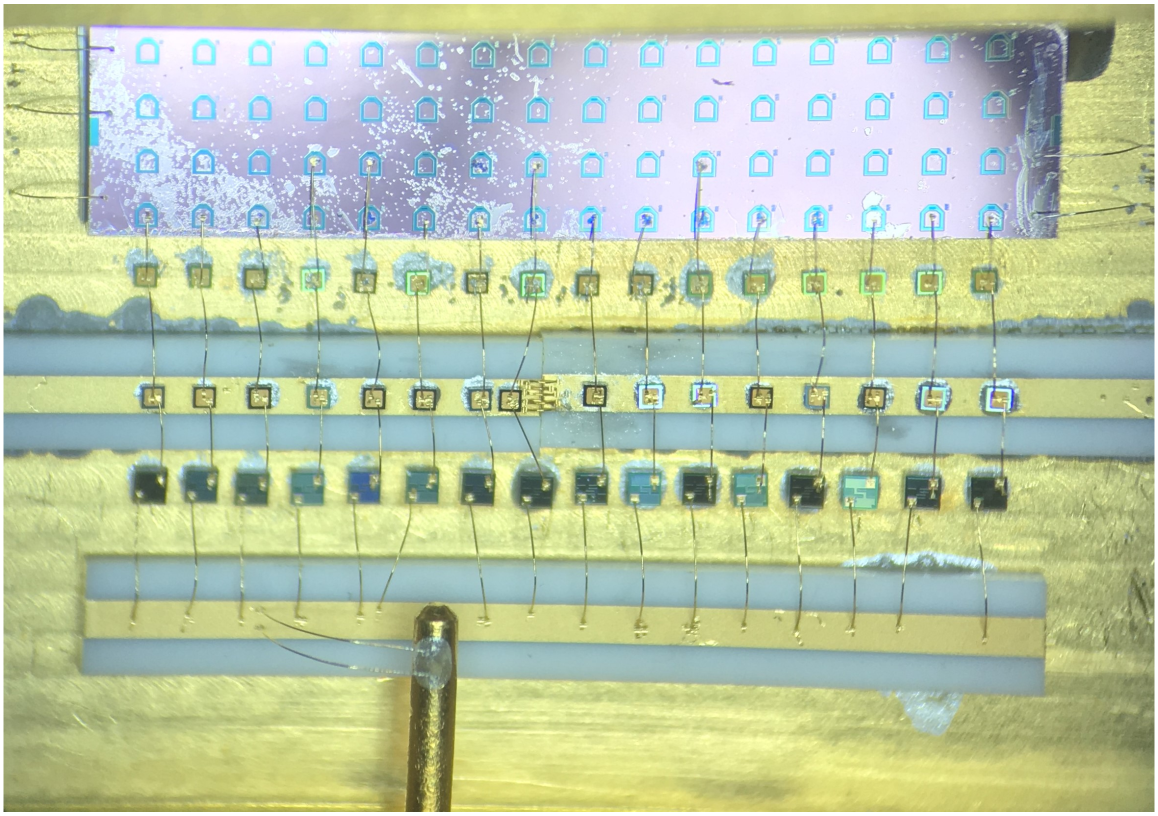

Figure 38: Assembled SNRSPD array circuits. DC is sourced from the pin at the bottom. 16 devices are connected in parallel each with a 2.5kΩ resistor, a 1.8pF coupling capacitor, and a 6.8pF parallel capacitor. A 50Ω line is implemented in order to readout the microwave response.

resistors are attached to the line with bond wires and are sequentially attached to 1.8pF coupling capacitors. The coupling capacitors are attached to 6.8pF resonator capacitors. The capacitors are Skyworks lumped element capacitors.

To avoid fabrication defects, the nanowires were made to be $\sim$100nm wide with a film thickness of $\sim$350nm. The resulting inductance was $\sim$80pH/$\square$. To vary the inductance of each pixel, the nanowire length remained constant and a serial inductor of varying length was added to each nanowire line (Figure 37). The nanowires were situated along a linear array with $200 \times 200 \mu\text{m}^2$ bonding pads. The chip contained four additional and identical rows of nanowires for redundancy. Future chips will contain unique nanowires at each pixel location. Figure 38 shows the assembled circuits. The inductance ranged from ∼110nH to ∼521nH in each row. This should result in resonant frequencies ranging from ∼74.9MHz to ∼161MHz based on Equation 4.23.

6.2.1.2 Cryostat Mount

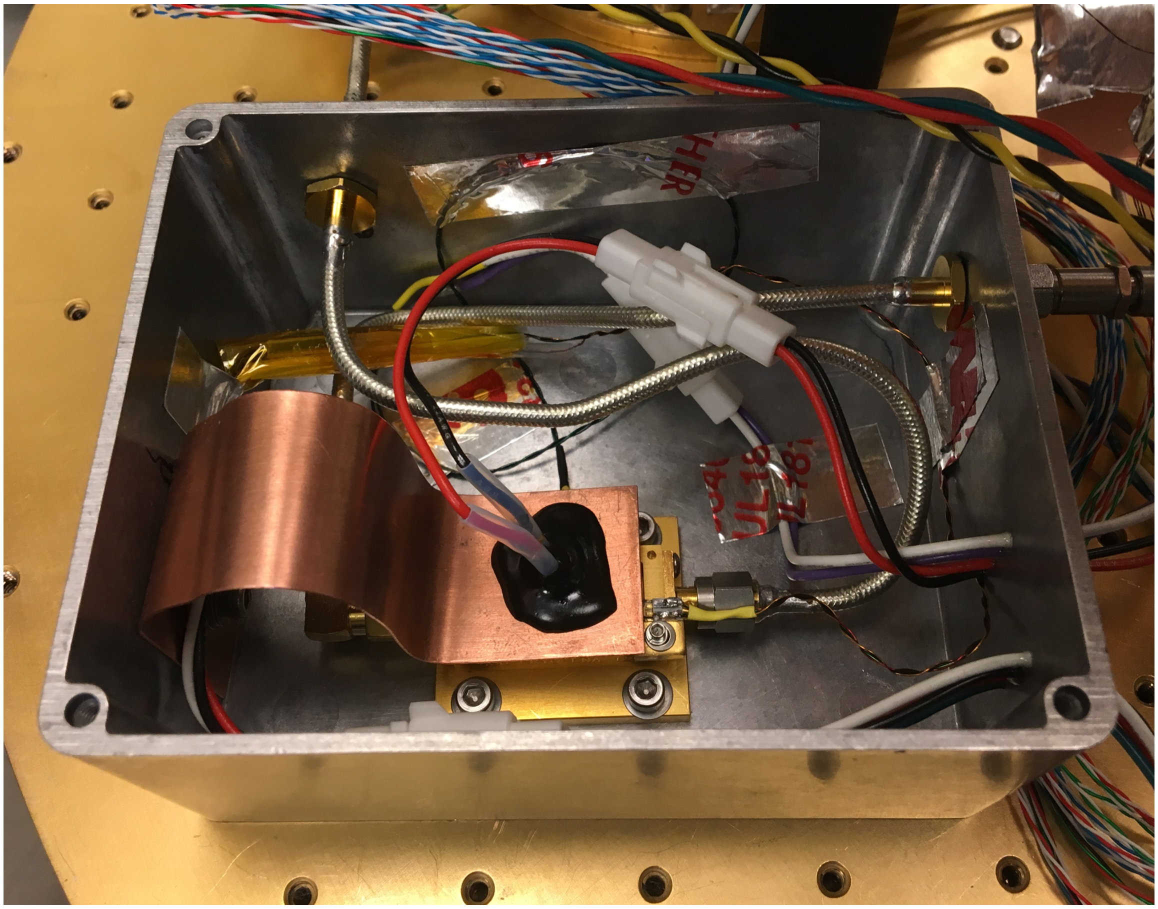

Figure 39: The SNRSPD package was mounted inside a Hammond box on the coldplate. A temperature sensor is bolted directly to the package. A 1300nm LED was situated above the package for direct photon coupling in free space.

Figure 39 and Figure 40 show the SNRSPD package mounted inside a Hammond

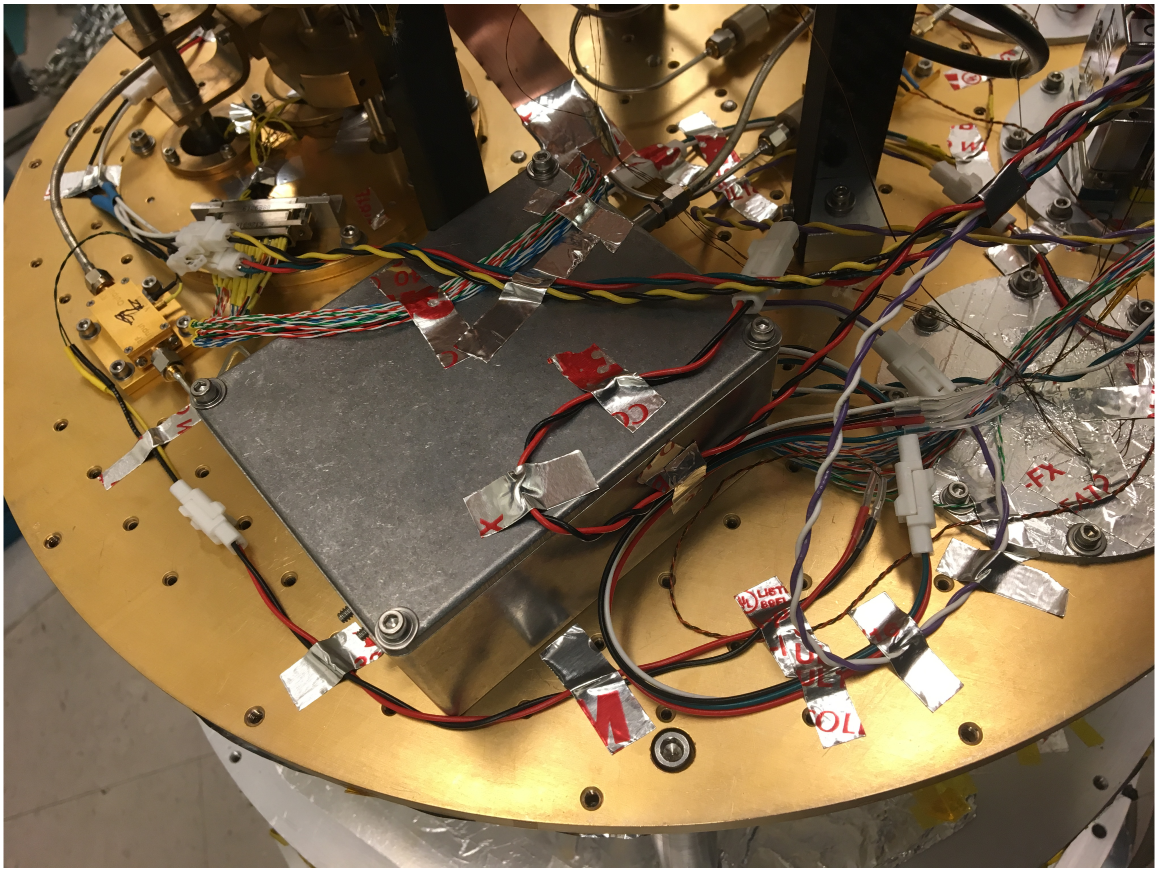

Figure 40: The Hammond box containing the SNRSPD package was mounted on the coldplate with a cryogenic 30dB attenuator on the input and a 30dB 10MHz-2GHz LNA on the output.

box that is bolted to the coldplate of the cryostat. This precaution was taken to shield from stray radiation from other experiments taking place simultaneously during the cryogenic experimental run. While the Hammond box was a beneficial addition, it created an issue with the proximity of the LED to the SNRSPD package. During measurements, this caused the region around the package to heat up. Further experiments should implement a setup with the LED situated further from the package to avoid thermal effects.

6.2.2 Response Measurements

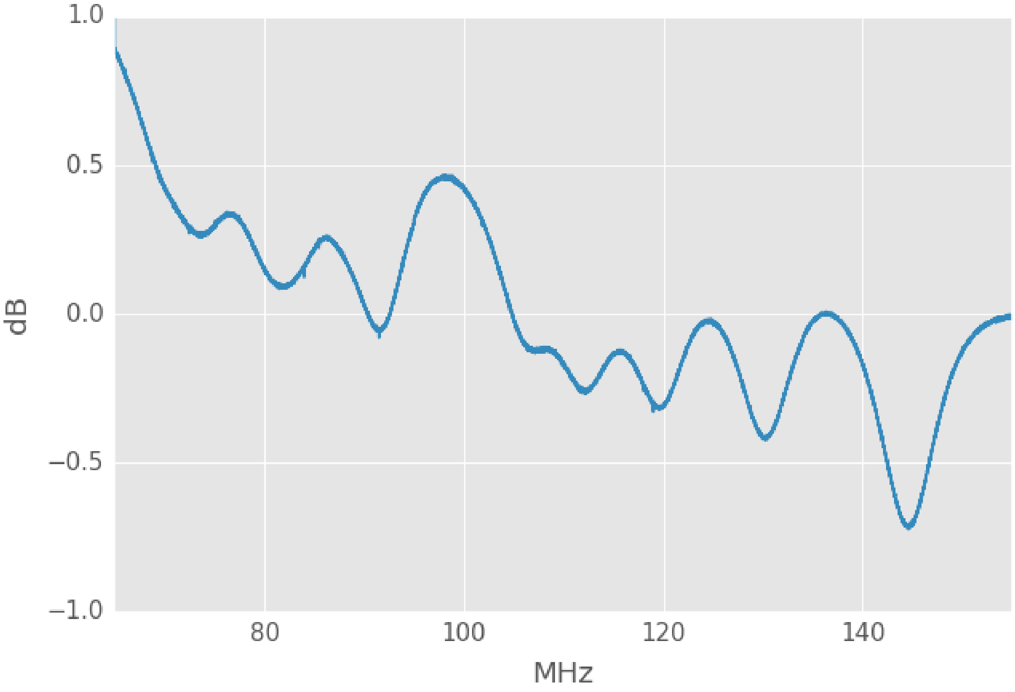

Figure 41: Averaged microwave response of the SNRSPD array with -100dBm of AC power incident on the package. The resonances ranged from ∼73.4MHz to ∼144.5MHz.

The microwave response of the array shows that the depths of the resonances for the current configuration are on the order of half a dB. Figure 41 shows the data for a base temperature of ∼3.5K.

The time domain response (Figure 42) shows that the pulses range from ∼8.2ns to ∼16ns. This corresponds to resonant frequencies at and between ∼62.5MHz to ∼122MHz. The ringdown frequency of the measured single photon pulses roughly correspond to the the expected resonant frequencies.

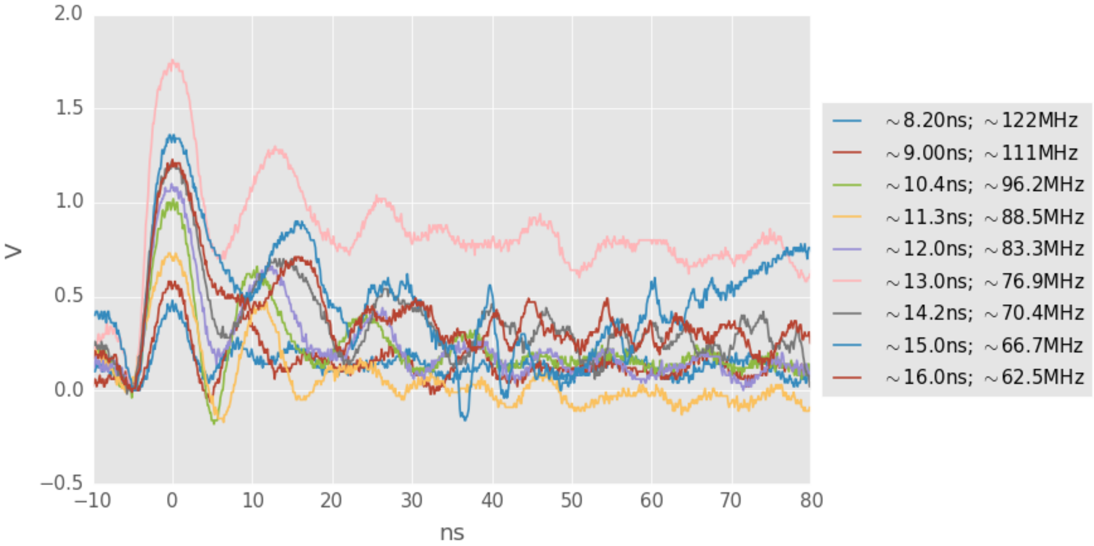

Figure 42: Transient responses of the SNRSPD array with a 45μA DC bias incident on the package.

6.2.3 Simulations

6.2.3.1 LTspice Schematic & Parameters

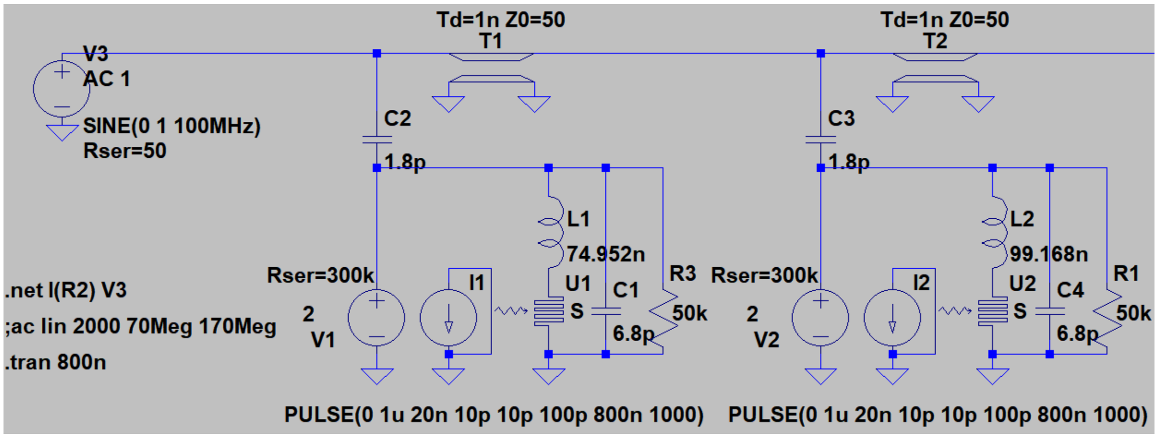

```
.net I(R2) V3
;ac lin 2000 70Meg 170Meg
.tran 800n
```

Figure 43: LTspice layout showing 2 of the 16 pixels.

Figure 43 shows the LTspice layout used to simulate the response of the SNRSPD array. The nanowires had parameters $T_{BASE} = 3.5\text{K}$ and $L = 35\text{nH}$. The serial inductors varied from ∼75nH to ∼486nH. The resistors were varied between 2.5kΩ, 10kΩ, 30kΩ, and 50kΩ.

6.2.3.2 Pre-Measurement Simulations

The concept was developed with an optimization of the maximum count rate. This was achieved by minimizing the decay time of the transient. Low Q resonances were obtained by using 2.5kΩ resistors attached to the resonators. Figure 44 shows the expected pulses from the lowest and highest frequency pixel.

6.2.3.3 Post-Measurement Simulations

In order to better understand the measurement results, the frequency domain response was simulated and compared to the experimental data. The data was comparable to the simulated response. It is likely that small errors in fabrication and the subsequent estimated inductances led to the discrepancies in the spread of the frequencies as shown in Figure 45.

Figure 46 shows the simulated transfer functions for 2.5kΩ, 10kΩ, 30kΩ, and 50kΩ resistors. Figure 47 shows the expected pulses for the same resistance variation. Based on the simulations, 50kΩ resistors will provide for much higher Q resonances, but will severely limit the count rate. The count rate per pixel was maximized with the 2.5kΩ resistor variation with a predicted count rate of ∼20MHz for the last pixel in

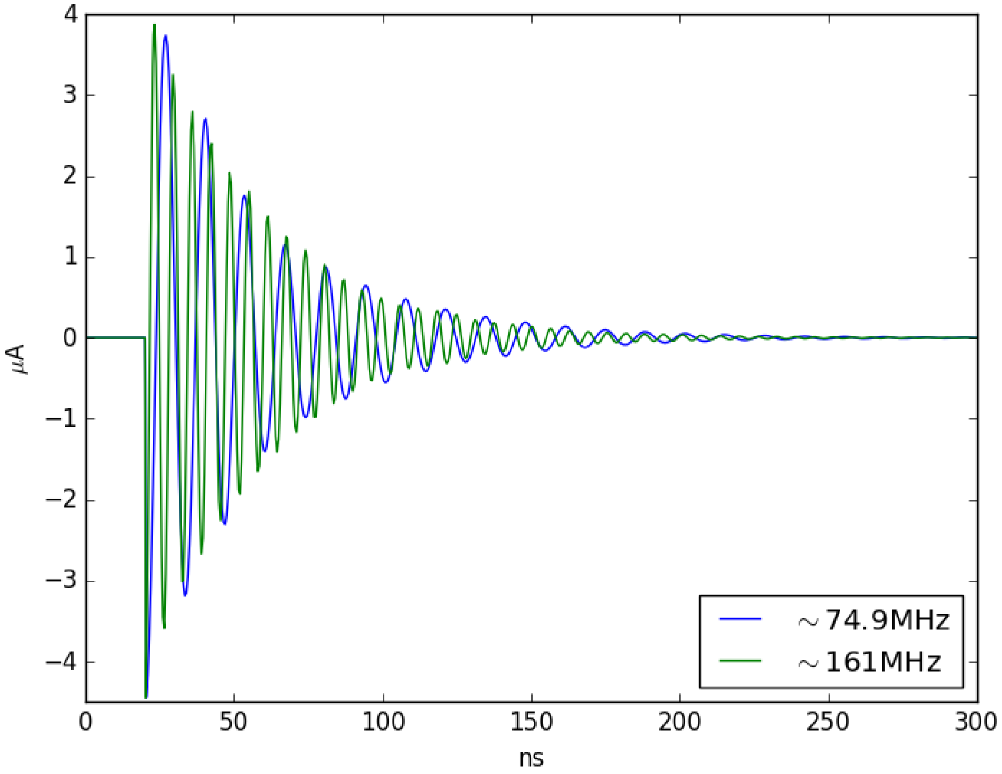

Figure 44: Simulated transient response of the first and last pixel in the SNRSPD array with 2.5kΩ resistors.

the array given a match to the simulations. With 50kΩ resistors, the predicted count rate is ∼3MHz.

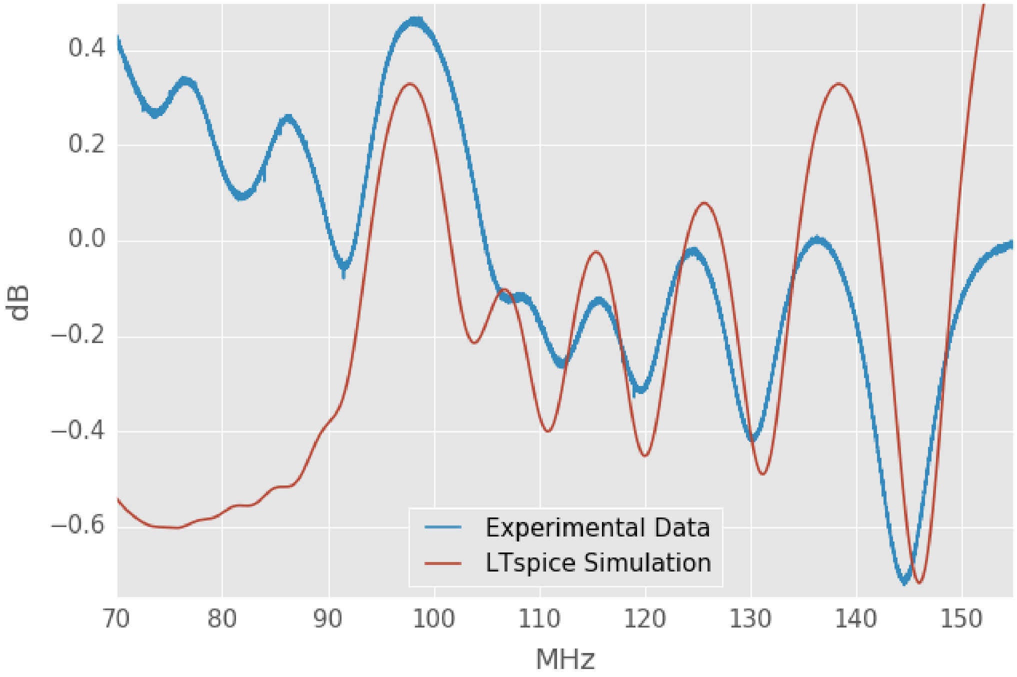

Figure 45: Simulated microwave response of the SNRSPD array with 2.5kΩ resistors compared with experimental data.

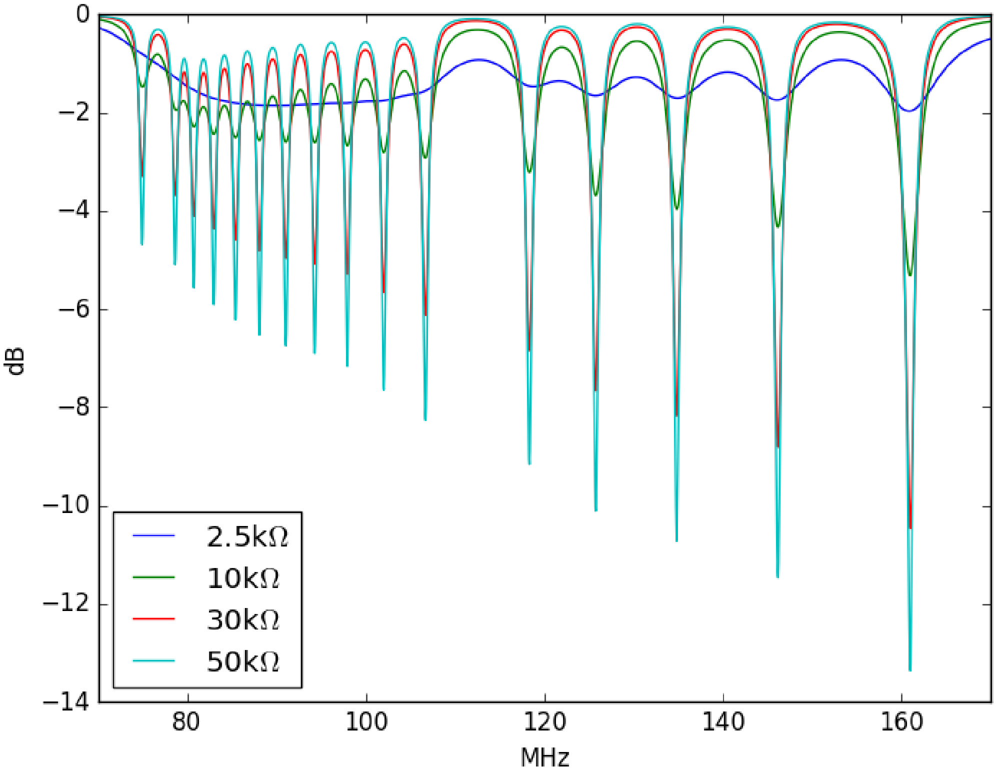

Figure 46: Simulated microwave responses of the SNRSPD array with 2.5kΩ, 10kΩ, 30kΩ, and 50kΩ resistors.

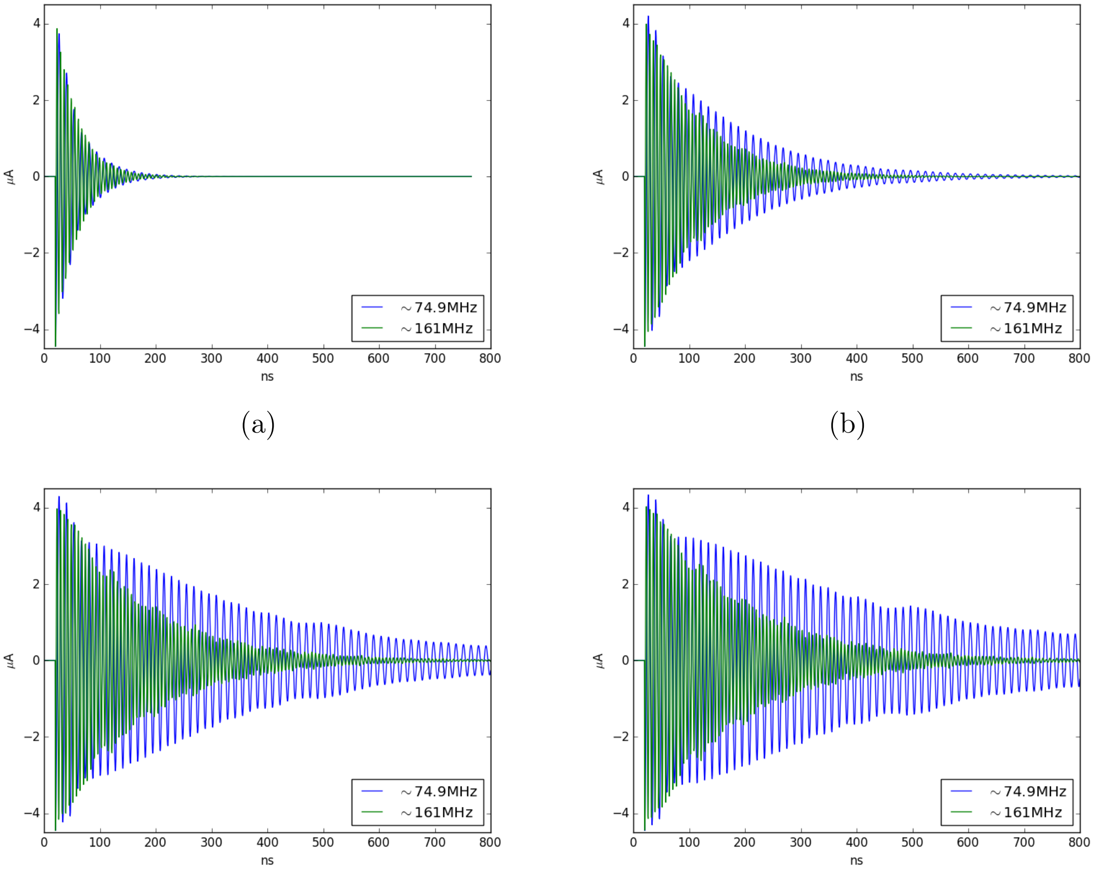

(a)

(b)

(c)

(d)

Figure 47: Simulated transient responses of the first and last pixel in the SNRSPD array for 2.5kΩ, 10kΩ, 30kΩ, and 50kΩ resistors.

Chapter 7

CONCLUSION

This chapter concludes our discussion on the development of superconducting nanowire single photon technologies for advanced applications. We began this dissertation with a short consideration of the properties and behaviors of a single photon. We followed up with a brief history of single photon detectors including PMTs, KIDs, and SNSPD devices. Next, we provided an overview of four advanced applications that SNSPD devices may be used for. These applications included intensity interferometry, the fast imaging of exoplanet signals, deep space optical communication, and quantum information.

Before delving into our investigation of developing SNSPD devices to be suitable for these applications, we reviewed the fundamentals of superconductivity theory and the physics of superconducting films that drive the mechanisms we studied. These mechanisms were elaborated on in the context of resonator theory with respect to superconducting nanowire devices. We reviewed all of the necessary formulations required for the analysis of the devices presented in this dissertation.

We next went over characterization of an SNRSPD two-pixel prototype. We found values for the kinetic inductance $L_K = 586,\ 731$nH, parasitic resistance $R = 0.9\Omega,\ 5.2\Omega$, quality factors $Q_r = 23.3,\ 37.2$ and $Q_i = 190,\ 82.2$ and $Q_c = 27.4,\ 30.4$, critical temperature $T_C \approx 8.5$K, and characteristic current $I_* = 27.3,\ 26.6\mu$A of each pixel. For these nanowires, we found that the band-gap energy is $\Delta_0 \approx 1.1$meV and that the density of states at the Fermi energy is $N_0 \sim 10^{10}/\text{eV}/\mu\text{m}^3$. Furthermore, we found values for the number of quasiparticles present in the material $N_{qp} \sim 10^5$

quasiparticles at 2.8K. With respect to operational modes of the two-pixel prototype, we found that a high AC bias in KID mode is inferior for photon counting experiments compared to operation in a DC-biased SPD mode due to the small fraction of time spent near the critical current with an AC bias. We found a photon count rate of $\Gamma_{KID} = 150$ photons/s/mA in a critically biased KID mode and a photon count rate of $\Gamma_{SPD} = 10^6$ photons/s/mA in SPD mode.

We discussed the simulations of a DC-biased, frequency-multiplexed readout of SNSPD devices in ADS, LTspice, and Sonnet. We find that a multiplexing factor of 100 is achievable with a total count rate of > 5MHz and are confident that this readout could enable a 10000-pixel array to be used for advanced applications such as exoplanet imaging or quantum communications. Finally, we presented a prototype array design based on lumped element components along with data from an early implementation of the array designed to have 16 pixels in the frequency range of 74.9MHz to 161MHz. Future development of this technology will involve following through with the testing of the 16-pixel array with varying values of the biasing resistors. Higher resistance values, while lowering the maximum count rate achievable, will provide for more well defined signals to work with in the prototyping stage. A final implementation of the presented DC-biased, frequency-multiplexed SNSPD array will require the full resonant circuit of each pixel to be fabricated on a single chip along a single feedline for optimum efficiency and maximized detector quality.

REFERENCES

Adami, C., and N. J. Cerf. 1999. "Quantum Computation with Linear Optics." In *Quantum Computing and Quantum Communications,* edited by Colin P. Williams, 391–401. Berlin, Heidelberg: Springer Berlin Heidelberg.

Allen, James S. 1939. "The Detection of Single Positive Ions, Electrons and Photons by a Secondary Electron Multiplier." *Phys. Rev.* 55 (10): 966–971. doi:10.1103/PhysRev.55.966.

Annett, J.F. 2004. *Superconductivity, Superfluids and Condensates.* Oxford Master Series in Physics. OUP Oxford. https://books.google.com/books?id=WZcXmBrZIc8C.

Annunziata, A. J. 2010. "Single-Photon Detection, Kinetic Inductance, and Non-Equilibrium Dynamics in Niobium and Niobium Nitride Superconducting Nanowires." PhD diss., Yale University.

Annunziata, A. J., D. F. Santavicca, L. Frunzio, G. Catelani, M. J. Rooks, A. Frydman, and D. E. Prober. 2010a. "Tunable superconducting nanoinductors." *Nanotechnology* 21, 445202 (November): 445202. doi:10.1088/0957-4484/21/44/445202. arXiv: 1007.4187 `[cond-mat.supr-con]`.

Annunziata, Anthony J, Daniel F Santavicca, Luigi Frunzio, Gianluigi Catelani, Michael J Rooks, Aviad Frydman, and Daniel E Prober. 2010b. "Tunable superconducting nanoinductors." *Nanotechnology* 21 (44): 445202. http://stacks.iop.org/0957-4484/21/i=44/a=445202.

Aude, Diana Prado Lopes. 2010. "Modeling superconductors using surface impedance techniques." PhD diss., Massachusetts Institute of Technology.

Baek, Burm, Lijun Ma, Alan Mink, Xiao Tang, and Sae Woo Nam. 2009. "Detector performance in long-distance quantum key distribution using superconducting nanowire single-photon detectors," vol. 7320, doi:10.1117/12.818793.

Baldwin, Jason, Christopher A. Haniff, C. D. Mackay, and P. J. Warner. 1986. "Closure phase in high-resolution optical imaging." *Nature* 320:595–597.

Bardeen, J., L. N. Cooper, and J. R. Schrieffer. 1957a. "Microscopic Theory of Superconductivity." 106 (April): 162–164. doi:10.1103/PhysRev.106.162.

———. 1957b. "Theory of Superconductivity." *Physical Review* 108 (December): 1175–1204. doi:10.1103/PhysRev.108.1175.

Bardeen, John. 1958. “Two-Fluid Model of Superconductivity.” *Phys. Rev. Lett.* 1 (11): 399–400. doi:10.1103/PhysRevLett.1.399.

Baselmans, J., S. J. C. Yates, R. Barends, Y. J. Y. Lankwarden, J. R. Gao, H. Hoevers, and T. M. Klapwijk. 2008. “Noise and Sensitivity of Aluminum Kinetic Inductance Detectors for Sub-mm Astronomy.” *Journal of Low Temperature Physics* 151 (1): 524–529. doi:10.1007/s10909-007-9684-3.

Bedorf, S. H. 2005. “Development of Ultrathin Niobium Nitride and Niobium Titanium Nitride Films for THz Hot-Electron Bolometers.” PhD diss., Universitat zu Koln.

Beebe, Melissa R., Douglas B. Beringer, Matthew C. Burton, Kaida Yang, and R. Alejandra Lukaszew. 2016. “Stoichiometry and thickness dependence of superconducting properties of niobium nitride thin films.” *Journal of Vacuum Science & Technology A* 34 (2): 021510. doi:10.1116/1.4940132. eprint: https://doi.org/10.1116/1.4940132.

Beijersbergen, M.W., R.P.C. Coerwinkel, M. Kristensen, and J.P. Woerdman. 1994. “Helical-wavefront laser beams produced with a spiral phaseplate.” *Optics Communications* 112 (5): 321–327. doi:https://doi.org/10.1016/0030-4018(94)90638-6.

Bennett, Charles H., and Gilles Brassard. 1984. “Quantum cryptography: Public key distribution and coin tossing.” *Theor. Comput. Sci.* 560.

Berggren, Karl K, Qing-Yuan Zhao, Nathnael Abebe, Minjie Chen, Prasana Ravindran, Adam McCaughan, and Joseph C Bardin. 2018. “A superconducting nanowire can be modeled by using SPICE.” *Superconductor Science and Technology* 31 (5): 055010. http://stacks.iop.org/0953-2048/31/i=5/a=055010.

Bessell, M. S. 1979. “UBVRI photometry. II - The Cousins VRI system, its temperature and absolute flux calibration, and relevance for two-dimensional photometry.” *pasp* 91 (October): 589–607. doi:10.1086/130542.

Biswas, Srinivasan, Piazzolla, and Hoppe. 2018. “Deep space optical communications,” vol. 10524, doi:10.1117/12.2296426.

Bohr, Niels. 1928. “The Quantum Postulate and the Recent Development of Atomic Theory.” *Nature* 121:580–590.

Born, M. 1926. “Zur Quantenmechanik der Stoßvorgänge.” *Zeitschrift fur Physik* 37 (December): 863–867. doi:10.1007/BF01397477.

Bose. 1924. “Plancks Gesetz und Lichtquantenhypothese.” *Zeitschrift fur Physik* 26 (December): 178–181. doi:10.1007/BF01327326.

Bottom, Michael, Garreth Ruane, and Dimitri Mawet. 2017. “Noise-weighted Angular Differential Imaging.” *Research Notes of the AAS* 1 (1): 30. http://stacks.iop.org/2515-5172/1/i=1/a=30.

Buckel, W. 1991. *Superconductivity: Fundamentals and Applications.* VCH. https://books.google.com/books?id=BhhRAAAAMAAJ.

Campins, H., G. H. Reike, and M. J. Lebofsky. 1984. “Absolute Calibration of Photometry at 1 through 5 μm.” In *Bulletin of the American Astronomical Society,* 16:941. baas. September.

Chauvin, G., A.-M. Lagrange, C. Dumas, B. Zuckerman, D. Mouillet, I. Song, J.-L. Beuzit, and P. Lowrance. 2004. “A giant planet candidate near a young brown dwarf* - Direct VLT/NACO observations using IR wavefront sensing.” *A&A* 425 (2): L29–L32. doi:10.1051/0004-6361:200400056.

Che, George. 2018. “Advancements in Kinetic Inductance Detector, Spectrometer, and Amplifier Technologies for Millimeter-Wave Astronomy.” PhD diss.

Chen, SiJing, DengKuan Liu, LiXing You, YongLiang Wang, LongQing Qiu, XiaoMing Xie, MianHeng Jiang, et al. 2013. “Superconducting nanowire single-photon detection system and demonstration in quantum key distribution.” *Chinese Science Bulletin* 58, no. 10 (April): 1145–1149. doi:10.1007/s11434-013-5698-1.

Cooper, Leon N. 1956. “Bound Electron Pairs in a Degenerate Fermi Gas.” *Phys. Rev.* 104 (4): 1189–1190. doi:10.1103/PhysRev.104.1189.

Day, P. K., H. G. LeDuc, B. A. Mazin, A. Vayonakis, and J. Zmuidzinas. 2003. “A broadband superconducting detector suitable for use in large arrays.” *Nature* 425 (October): 817–821. doi:10.1038/nature02037.

Di Paolo, F. 2000. *Networks and Devices Using Planar Transmissions Lines.* Taylor & Francis. https://books.google.com/books?id=z9CsA1ZvwW0C.

Dickinson, R. 1985. “A comparison of 8.415-, 32.0- and 565646-GHz deep space telemetry links” (November).

Dirac, P. A. M. 1926. “On the Theory of Quantum Mechanics.” *Proceedings of the Royal Society of London Series A* 112 (October): 661–677. doi:10.1098/rspa.1926.0133.

Doerner, S., A. Kuzmin, S. Wuensch, I. Charaev, F. Boes, T. Zwick, and M. Siegel. 2017. "Frequency-multiplexed bias and readout of a 16-pixel superconducting nanowire single-photon detector array." *Appl. Phys. Lett.* 111 (3): 032603. doi:10.1063/1.4993779. eprint: http://dx.doi.org/10.1063/1.4993779.

Doerner, S., A. Kuzmin, S. Wuensch, K. Ilin, and M. Siegel. 2016. "Operation of Superconducting Nanowire Single-Photon Detectors Embedded in Lumped-Element Resonant Circuits." *IEEE Transactions on Applied Superconductivity* 26, no. 3 (April): 1–5. doi:10.1109/TASC.2016.2525995.

Donati, O, P Missiroli, and G Pozzi. 1973. "An Experiment on Electron Interference," 41 (May): 639–644.

Doyle, S. 2008. "Lumped Element Kinetic Inductance Detectors." PhD diss., Cardiff University.

Doyle, S., P. Mauskopf, J. Naylon, A. Porch, and C. Duncombe. 2008. "Lumped Element Kinetic Inductance Detectors." *Journal of Low Temperature Physics* 151 (April): 530–536. doi:10.1007/s10909-007-9685-2.

Dravins, D., T. Lagadec, and P. D. Nuñez. 2015. "Stellar Intensity Interferometry over Kilometer Baselines: Optical aperture synthesis with electronically connected telescopes." *IAU General Assembly* 22, 2233727 (August): 2233727.

Drude, P. 1900a. "Zur Elektronentheorie der Metalle." *Annalen der Physik* 306 (3): 566–613. doi:10.1002/andp.19003060312.

———. 1900b. "Zur Elektronentheorie der Metalle; II. Teil. Galvanomagnetische und thermomagnetische Effecte." *Annalen der Physik* 308 (11): 369–402. doi:10.1002/andp.19003081102.

Dzifa Akua Parrianen, Josie, Andreas Papageorgiou, Simon Doyle, and Enzo Pascale. 2018. "Modelling the Performance of Single-Photon Counting Kinetic Inductance Detectors" (January).

Eibenberger, Sandra, Stefan Gerlich, Markus Arndt, Marcel Mayor, and Jens Tuxen. 2013. "Matter-wave interference of particles selected from a molecular library with masses exceeding 10 000 amu." *Phys. Chem. Chem. Phys.* 15 (35): 14696–14700. doi:10.1039/C3CP51500A.

Einstein, Albert. 1905. "Concerning an heuristic point of view toward the emission and transformation of light." *Annalen Phys.* 17:132–148.

Einstein, Albert. 1924. “Quantentheorie des einatomigen idealen Gases.” *Sitzungsberichte der Preußischen Akademie der Wissenschaften* Physikalisch-mathematische Klasse:261–267.

Ekert, Artur K. 1991. “Quantum cryptography based on Bell’s theorem.” *Phys. Rev. Lett.* 67 (6): 661–663. doi:10.1103/PhysRevLett.67.661.

Elkins-Tanton, L. T., E. Asphaug, J. Bell, D. Bercovici, B. G. Bills, R. P. Binzel, W. F. Bottke, et al. 2014. “Journey to a Metal World: Concept for a Discovery Mission to Psyche.” In *Lunar and Planetary Science Conference,* 45:1253. Lunar and Planetary Science Conference. March.

Fermi, Enrico. 1926. “Zur Quantelung des idealen einatomigen Gases. (German) [On the quantization of an ideal monatomic gas]” [in German]. 36, nos. 11–12 (November): 902–912. doi:https://doi.org/10.1007/BF01400221.

Figer, Aull, Schuette, Hanold, Kolb, and Lee. 2011. “Silicon single photon imaging detectors,” vol. 8155, doi:10.1117/12.898570.

Figer, Lee, Hanold, Aull, Gregory, and Schuette. 2011. “A photon-counting detector for exoplanet missions,” vol. 8151, doi:10.1117/12.893655.

Finnemore, D. K., T. F. Stromberg, and C. A. Swenson. 1966. “Superconducting Properties of High-Purity Niobium.” *Phys. Rev.* 149 (1): 231–243. doi:10.1103/PhysRev.149.231.

Foellmi, C. 2009. “Intensity interferometry and the second-order correlation function $g^{(2)}$ in astrophysics.” *Astronomy and Astrophysics* 507 (December): 1719–1727. doi:10.1051/0004-6361/200911739.

Foreman-Mackey, Daniel, David W. Hogg, Dustin Lang, and Jonathan Goodman. 2013. “emcee: The MCMC Hammer.” *Publications of the Astronomical Society of the Pacific* 125 (925): 306. http://stacks.iop.org/1538-3873/125/i=925/a=306.

Gao, J. 2008. “The Physics of Superconducting Microwave Resonators.” PhD diss., California Institute of Technology.

Gao, J., M. R. Vissers, M. O. Sandberg, F. C. S. da Silva, S. W. Nam, D. P. Pappas, D. S. Wisbey, et al. 2012. “A titanium-nitride near-infrared kinetic inductance photon-counting detector and its anomalous electrodynamics.” *Applied Physics Letters* 101 (14): 142602. doi:10.1063/1.4756916. eprint: https://doi.org/10.1063/1.4756916.

Gisin, Nicolas, Grégoire Ribordy, Wolfgang Tittel, and Hugo Zbinden. 2002. "Quantum cryptography." *Rev. Mod. Phys.* 74 (1): 145–195. doi:10.1103/RevModPhys.74.145.

Glauber, Roy J. 1963. "Coherent and Incoherent States of the Radiation Field." *Phys. Rev.* 131 (6): 2766–2788. doi:10.1103/PhysRev.131.2766.

Goban, A., C.-L. Hung, S.-P. Yu, J. D. Hood, J. A. Muniz, J. H. Lee, M. J. Martin, et al. 2014. "Atom-light interactions in photonic crystals." Article, *Nature Communications* 5 (May). http://dx.doi.org/10.1038/ncomms4808.

Grangier, P., G. Roger, and A. Aspect. 1986. "Experimental Evidence for a Photon Anticorrelation Effect on a Beam Splitter: A New Light on Single-Photon Interferences." *EPL (Europhysics Letters)* 1 (4): 173. http://stacks.iop.org/0295-5075/1/i=4/a=004.

Griffiths, David J. 2004. *Introduction to Quantum Mechanics (2nd Edition).* 2nd. Pearson Prentice Hall, April. http://www.amazon.com/exec/obidos/redirect?tag=citeulike07-20%5C&path=ASIN/0131118927.

Hadfield, Robert H. 2009. "Single-photon detectors for optical quantum information applications." *Nature Photonics* 3, no. 12 (December): 696–705. doi:10.1038/nphoton.2009.230.

Hanbury Brown, R. 1956. "A Test of a New Type of Stellar Interferometer on Sirius." *Nature* 178 (November): 1046–1048. doi:10.1038/1781046a0.

Haniff, Christopher A., C. D. Mackay, David J. Titterington, Devinderjit S Sivia, Jason Baldwin, and P. J. Warner. 1987. "The first images from optical aperture synthesis." *Nature* 328:694–696.

Hofherr, M., M. Arndt, K. Il'in, D. Henrich, M. Siegel, J. Toussaint, T. May, and H. G. Meyer. 2013. "Time-Tagged Multiplexing of Serially Biased Superconducting Nanowire Single-Photon Detectors." *IEEE Transactions on Applied Superconductivity* 23, no. 3 (June): 2501205–2501205. doi:10.1109/TASC.2013.2245935.

Hofherr, M., D. Rall, K. Ilin, M. Siegel, A. Semenov, H.-W. Hübers, and N. A. Gippius. 2010. "Intrinsic detection efficiency of superconducting nanowire single-photon detectors with different thicknesses." *Journal of Applied Physics* 108 (1): 014507. doi:10.1063/1.3437043. eprint: https://doi.org/10.1063/1.3437043.

Hohenberg, P.C., and A.P. Krekhov. 2015. "An introduction to the Ginzburg–Landau theory of phase transitions and nonequilibrium patterns." An introduction to the Ginzburg–Landau theory of phase transitions and nonequilibrium patterns, *Physics Reports* 572:1–42. doi:https://doi.org/10.1016/j.physrep.2015.01.001.

Hooke, R. 1672. "Mr Isaac Newtons Answer to some Considerations [of Robert Hooke] upon his doctrine of Light and Colors."

———. 1678. *Lectures de Potentia Restitutiva, Or of Spring Explaining the Power of Springing Bodies.* [Cutlerian lecture. John Martyn. https://books.google.com/books?id=LAtPAAAAcAAJ.

Ivry, Yachin, Chung-Soo Kim, Andrew E. Dane, Domenico De Fazio, Adam N. McCaughan, Kristen A. Sunter, Qingyuan Zhao, and Karl K. Berggren. 2014. "Universal scaling of the critical temperature for thin films near the superconducting-to-insulating transition." *Phys. Rev. B* 90 (21): 214515. doi:10.1103/PhysRevB.90.214515.

Jenkins, Francis A., and Harvey Elliott White. 1950. *Fundamentals of optics / by Francis A. Jenkins and Harvey E. White* [in English]. 2nd ed. xi, 647 p. McGraw-Hill New York.

Jennewein, Thomas, Marco Barbieri, and Andrew G. White. 2011. "Single-photon device requirements for operating linear optics quantum computing outside the post-selection basis." *Journal of Modern Optics* 58 (3-4): 276–287. doi:10.1080/09500340.2010.546894. eprint: https://doi.org/10.1080/09500340.2010.546894.

Kalas, Paul, James R. Graham, Eugene Chiang, Michael P. Fitzgerald, Mark Clampin, Edwin S. Kite, Karl Stapelfeldt, Christian Marois, and John Krist. 2008. "Optical Images of an Exosolar Planet 25 Light-Years from Earth." *Science* 322 (5906): 1345–1348. doi:10.1126/science.1166609. eprint: http://science.sciencemag.org/content/322/5906/1345.full.pdf.

Kaplan, S. B., C. C. Chi, D. N. Langenberg, J. J. Chang, S. Jafarey, and D. J. Scalapino. 1976. "Quasiparticle and phonon lifetimes in superconductors." *Phys. Rev. B* 14 (11): 4854–4873. doi:10.1103/PhysRevB.14.4854.

Kaxiras, Efthimios. 2003. *Atomic and Electronic Structure of Solids.* Cambridge University Press. http://www.amazon.com/Atomic-Electronic-Structure-Efthimios-Kaxiras/dp/0521523397.

Kiepenheuer, K. O. 1937. "Über Zählrohre für das sichtbare Spektralgebiet." *Zeitschrift für Physik* 107, no. 3 (March): 145–152. doi:10.1007/BF01330356.

Knill, E, R Laflamme, and G Milburn. 2001. "A scheme for efficient quantum computation with linear optics," 409 (February): 46–52.

Kok, Pieter, W. J. Munro, Kae Nemoto, T. C. Ralph, Jonathan P. Dowling, and G. J. Milburn. 2007. "Linear optical quantum computing with photonic qubits." *Rev. Mod. Phys.* 79 (1): 135–174. doi:10.1103/RevModPhys.79.135.

Kolb, K., and D. F. Figer. 2015. "GM-APD imaging arrays for direct imaging of exoplanets." In *2015 IEEE Aerospace Conference,* 1–9. March. doi:10.1109/AERO.2015.7119268.

Lafrenière, David, Christian Marois, René Doyon, Daniel Nadeau, and Étienne Artigau. 2007. "A New Algorithm for Point-Spread Function Subtraction in High-Contrast Imaging: A Demonstration with Angular Differential Imaging." *The Astrophysical Journal* 660 (1): 770. http://stacks.iop.org/0004-637X/660/i=1/a=770.

Lavery, Martin P. J., David J. Robertson, Gregorius C. G. Berkhout, Gordon D. Love, Miles J. Padgett, and Johannes Courtial. 2012. "Refractive elements for the measurement of the orbital angular momentum of a single photon." *Opt. Express* 20, no. 3 (January): 2110–2115. doi:10.1364/OE.20.002110.

Leach, Jonathan, Miles Padgett, Stephen M Barnett, Sonja Franke-Arnold, and Johannes Courtial. 2002. "Measuring the Orbital Angular Momentum of a Single Photon," 88 (July): 257901.

Lo, Hoi-Kwong, Sandu Popescu, and Tim Spiller, eds. 2002. *Introduction to Quantum Computation Information.* River Edge, NJ, USA: World Scientific Publishing Co., Inc.

Lynton, E.A. 1962. *Superconductivity.* Methuen's monographs on physical subjects. Methuen. https://books.google.com/books?id=KyCzrQEACAAJ.

Mamajek, E. E. 2005. "A Moving Cluster Distance to the Exoplanet 2M1207b in the TW Hydrae Association." *APJ* 634 (December): 1385–1394. doi:10.1086/468181. eprint: astro-ph/0507416.

Mandel, L., and E. Wolf. 1965. "Coherence Properties of Optical Fields." *Rev. Mod. Phys.* 37 (2): 231–287. doi:10.1103/RevModPhys.37.231.

Mandel, Leonard. 1959. "Fluctuations of Photon Beams: The Distribution of the Photo-Electrons." *Proceedings of the Physical Society* 74 (3): 233. http://stacks.iop.org/0370-1328/74/i=3/a=301.

Mandel, Leonard. 1999. "Quantum effects in one-photon and two-photon interference." *Rev. Mod. Phys.* 71 (2): S274–S282. doi:10.1103/RevModPhys.71.S274.

Marois, Doyon, Nadeau, Racine, Riopel, Vallée, and Lafrenière. 2005. "TRIDENT: An Infrared Differential Imaging Camera Optimized for the Detection of Methanated Substellar Companions." *PASP* 117 (July): 745–756. doi:10.1086/431347. eprint: astro-ph/0504652.

Marois, Lafrenière, Doyon, Macintosh, and Nadeau. 2006. "Angular Differential Imaging: A Powerful High-Contrast Imaging Technique." *The Astrophysical Journal* 641 (1): 556. http://stacks.iop.org/0004-637X/641/i=1/a=556.

Matthias, B. T., T. H. Geballe, and V. B. Compton. 1963. "Superconductivity." *Rev. Mod. Phys.* 35 (1): 1–22. doi:10.1103/RevModPhys.35.1.

Mattis, D. C., and J. Bardeen. 1958. "Theory of the Anomalous Skin Effect in Normal and Superconducting Metals." *Phys. Rev.* 111 (2): 412–417. doi:10.1103/PhysRev.111.412.

Mauskopf, P.D. 2018. "Transition Edge Sensors and Kinetic Inductance Detectors in Astronomical Instruments." *to appear in PASP.*

Mazin, B. 2004. "Microwave kinetic inductance detectors." PhD diss., California Institute of Technology.

Mazin, Bumble, Day, Eckart, Golwala, Zmuidzinas, and Harrison. 2006. "Position sensitive x-ray spectrophotometer using microwave kinetic inductance detectors." *Applied Physics Letters* 89, 222507 (22). doi:http://dx.doi.org/10.1063/1.2390664.

Mazin, Day, Le Duc, and Zmuidzinas. 2001. "Multiplexable kinetic inductance detectors." http://cds.cern.ch/record/867246.

McCaughan, Adam. 2017. "Readout architectures for superconducting nanowire single photon detectors," 31 (December).

Molina-Terriza, Gabriel, Juan P. Torres, and Lluis Torner. 2001. "Management of the Angular Momentum of Light: Preparation of Photons in Multidimensional Vector States of Angular Momentum." *Phys. Rev. Lett.* 88 (1): 013601. doi:10.1103/PhysRevLett.88.013601.

Natarajan, C. M., M. G. Tanner, and R. H. Hadfield. 2012. "Superconducting nanowire single-photon detectors: physics and applications." *Superconductor Science Tech-*

nology 25, no. 6, 063001 (June): 063001. doi:10.1088/0953-2048/25/6/063001. arXiv: 1204.5560 `[quant-ph]`.

Neumann, Gerhard, J. F. Cavanaugh, D. B. Coyle, John McGarry, D. E. Smith, X. Sun, Matt Torrence, T. W. Zagwodski, and M. T. Zuber. 2008. "Laser Ranging at Interplanetary Distances."

Newton, I. 1672. "Robert Hooke's Critique of Newton's Theory of Light and Colors."

Pfleegor, R. L., and L. Mandel. 1967. "Interference of Independent Photon Beams." *Phys. Rev.* 159 (5): 1084–1088. doi:10.1103/PhysRev.159.1084.

———. 1968. "Further Experiments on Interference of Independent Photon Beams at Low Light Levels∗†." *J. Opt. Soc. Am.* 58, no. 7 (July): 946–950. doi:10.1364/JOSA.58.000946.

Pilyavsky, Genady, Philip Mauskopf, Nathan Smith, Edward Schroeder, Adrian Sinclair, Gerard Van Belle, Natalie Hinkel, and Paul Scowen. 2017. "Single-Photon Intensity Interferometry (SPIIFy): Utilizing Available Telescopes" (February).

Pippard, A.B. 1953. "The coherence concept in superconductivity." *Physica* 19 (1): 765–774. doi:https://doi.org/10.1016/S0031-8914(53)80085-6.

Pittman, T, Bryan Jacobs, and J Franson. 2004. "Quantum Computing using Linear Optics," 25 (July).

Planck, Max. 1900. "Zur Theorie des Gesetzes der Energieverteilung im Normalspektrum. (German) [On the Theory of Distribution of Energy in the Normal Spectrum]" [in German]. 2, no. 17 (December): 237–245. http://web.ihep.su/dbserv/compas/src/planck00b/eng.pdf;%20http://web.ihep.su/owa/dbserv/hw.part2?s_c=PLANCK+1900B.

Quillen, Alice C. 2006. "Predictions for a planet just inside Fomalhaut's eccentric ring." *Monthly Notices of the Royal Astronomical Society: Letters* 372 (1): L14–L18. doi:10.1111/j.1745-3933.2006.00216.x. eprint: /oup/backfile/content_public/journal/mnrasl/372/1/10.1111/j.1745-3933.2006.00216.x/2/372-1-l14.pdf.

Rayleigh, Lord. 1879. "XXXI. Investigations in optics, with special reference to the spectroscope." *The London, Edinburgh, and Dublin Philosophical Magazine and Journal of Science* 8 (49): 261–274. doi:10.1080/14786447908639684. eprint: https://doi.org/10.1080/14786447908639684.

Rohlf, J.W. 1994. *Modern Physics from a to Z0.* John Wiley & Sons, Inc.

Schlaerth, J., A. Vayonakis, P. Day, J. Glenn, J. Gao, S. Golwala, S. Kumar, et al. 2008. "A Millimeter and Submillimeter Kinetic Inductance Detector Camera." *Journal of Low Temperature Physics* 151 (3): 684–689. doi:10.1007/s10909-008-9728-3.

Schneider, D. P., J. E. Gunn, and J. G. Hoessel. 1983. "CCD photometry of Abell clusters. I - Magnitudes and redshifts for 84 brightest cluster galaxies." *apj* 264 (January): 337–355. doi:10.1086/160602.

Schrödinger, E. 1926. "An Undulatory Theory of the Mechanics of Atoms and Molecules." *Physical Review* 28 (December): 1049–1070. doi:10.1103/PhysRev.28.1049.

Shibata, Hiroyuki, Kaoru Shimizu, Hiroki Takesue, and Yasuhiro Tokura. 2013. "Superconducting Nanowire Single-Photon Detector with Ultralow Dark Count Rate Using Cold Optical Filters." *Applied Physics Express* 6 (7): 072801. http://stacks.iop.org/1882-0786/6/i=7/a=072801.

Shiino, Tatsuya, Shoichi Shiba, Nami Sakai, Tetsuya Yamakura, Ling Jiang, Yoshinori Uzawa, Hiroyuki Maezawa, and Satoshi Yamamoto. 2010. "Improvement of the critical temperature of superconducting NbTiN and NbN thin films using the AlN buffer layer." *Superconductor Science and Technology* 23 (4): 045004. http://stacks.iop.org/0953-2048/23/i=4/a=045004.

Smirnov, K. V., A. V. Divochiy, Yu. B. Vakhtomin, M. V. Sidorova, U. V. Karpova, P. V. Morozov, V. A. Seleznev, A. N. Zotova, and D. Yu. Vodolazov. 2016. "Rise time of voltage pulses in NbN superconducting single photon detectors." *Applied Physics Letters* 109 (5): 052601. doi:10.1063/1.4960533. eprint: https://doi.org/10.1063/1.4960533.

Smith, J. 1985. "Ka-Band (32-GHz) Downlink Capability for Deep Space Communications" (October).

Stipčević, M., H. Skenderović, and D. Gracin. 2010. "Characterization of a novel avalanche photodiode for single photon detection in VIS-NIR range." *Optics Express* 18 (August): 17448. doi:10.1364/OE.18.017448. arXiv: 1004.0441 `[physics.ins-det]`.

Suzuki, Mitsumasa, Masahiro Baba, and Takeshi Anayama. 1987. "Critical Magnetic Fields of Superconducting NbN Films Prepared by Reactive Sputtering." *Japanese Journal of Applied Physics* 26 (S3-2): 947. http://iopscience.iop.org/1347-4065/26/S3-2/947.

Swenson, L. J., P. K. Day, B. H. Eom, H. G. Leduc, N. Llombart, C. M. McKenney, O. Noroozian, and J. Zmuidzinas. 2013. “Operation of a titanium nitride superconducting microresonator detector in the nonlinear regime.” *Journal of Applied Physics* 113, no. 10 (March): 104501–104501. doi:10.1063/1.4794808. arXiv: 1305.4281 `[cond-mat.supr-con]`.

Takemoto, Kazuya, Yoshihiro Nambu, Toshiyuki Miyazawa, Yoshiki Sakuma, Tsuyoshi Yamamoto, Shinichi Yorozu, and Yasuhiko Arakawa. 2015. “Quantum key distribution over 120 km using ultrahigh purity single-photon source and superconducting single-photon detectors.” Article, *Scientific Reports* 5 (September). http://dx.doi.org/10.1038/srep14383.

Tentrup, Tristan B. H., Thomas Hummel, Tom A. W. Wolterink, Ravitej Uppu, Allard P. Mosk, and Pepijn W. H. Pinkse. 2017. “Transmitting more than 10 bit with a single photon.” *Opt. Express* 25, no. 3 (February): 2826–2833. doi:10.1364/OE.25.002826.

Tinkham, Michael. 1996. *Introduction to Superconductivity.* McGraw-Hill Inc.

Tooley, M.H. 2006. *Electronic Circuits: Fundamentals and Applications.* Elsevier. https://books.google.com/books?id=8fuppV9O7xwC.

Tretyakov, D. B., A. V. Kolyako, A. S. Pleshkov, V. M. Entin, I. I. Ryabtsev, and I. G. Neizvestny. 2016. “Quantum key distribution in single-photon communication system.” *Optoelectronics, Instrumentation and Data Processing* 52, no. 5 (September): 453–461. doi:10.3103/S8756699016050071.

Valivarthi, R., I. Lucio-Martinez, A. Rubenok, P. Chan, F. Marsili, V. B. Verma, M. D. Shaw, et al. 2014. “Efficient Bell state analyzer for time-bin qubits with fast-recovery WSi superconducting single photon detectors.” *Opt. Express* 22, no. 20 (October): 24497–24506. doi:10.1364/OE.22.024497.

Van Duzer, T., and C.W. Turner. 1981. *Principles of superconductive devices and circuits.* Elsevier. https://books.google.com/books?id=rBpRAAAAMAAJ.

Vardulakis, G, S Withington, D J Goldie, and D M Glowacka. 2008. “Superconducting kinetic inductance detectors for astrophysics.” *Measurement Science and Technology* 19 (1): 015509. http://stacks.iop.org/0957-0233/19/i=1/a=015509.

Wernis, Rebecca A. 2013. “Characterizing a resonator bolometer array.” PhD diss., Caltech. http://resolver.caltech.edu/CaltechTHESIS:05312013-022124797.

Wiesner, Stephen. 1983. "Conjugate Coding." *SIGACT News* (New York, NY, USA) 15, no. 1 (January): 78–88. doi:10.1145/1008908.1008920.

Wilson, Lesh, and Yan. 1993. "GOPEX: a laser uplink to the Galileo spacecraft on its way to Jupiter," vol. 1866, doi:10.1117/12.149251.

Wolf, E. 1958. "Reciprocity Inequalities, Coherence Time and Bandwidth in Signal Analysis and Optics." *Proceedings of the Physical Society* 71 (2): 257. http://stacks.iop.org/0370-1328/71/i=2/a=315.

Yamashita, Miki, Makise, Qiu, Terai, Fujiwara, Sasaki, and Wang. 2011. "Origin of intrinsic dark count in superconducting nanowire single-photon detectors." *Applied Physics Letters* 99 (16): 161105. doi:10.1063/1.3652908.

Yamashita, Miki, Qiu, Fujiwara, Sasaki, and Wang. 2010. "Temperature Dependent Performances of Superconducting Nanowire Single-Photon Detectors in an Ultralow-Temperature Region." *Applied Physics Express* 3 (10): 102502. http://stacks.iop.org/1882-0786/3/i=10/a=102502.

Young, Thomas. 1802. "The Bakerian Lecture: On the Theory of Light and Colours." *Philosophical Transactions of the Royal Society of London* 92:12–48. http://www.jstor.org/stable/107113.

Zhang, Jin, W. Slysz, A. Verevkin, O. Okunev, G. Chulkova, A. Korneev, A. Lipatov, G. N. Gol'tsman, and R. Sobolewski. 2003. "Response time characterization of NbN superconducting single-photon detectors." *IEEE Transactions on Applied Superconductivity* 13, no. 2 (June): 180–183. doi:10.1109/TASC.2003.813675.

Zhao, Q., D. Zhu, N. Calandri, A. Dane, A. McCaughan, F. Bellei, H. Wang, D. Santavicca, and K. Berggren. 2017. "Single-photon imager based on a superconducting nanowire delay line." Article, *Nat. Photon.* 11, no. 4 (April): 247–251. http://dx.doi.org/10.1038/nphoton.2017.35.

Zmuidzinas, Jonas. 2012. "Superconducting Microresonators: Physics and Applications." *Annual Review of Condensed Matter Physics* 3 (1): 169–214. doi:10.1146/annurev-conmatphys-020911-125022. eprint: https://doi.org/10.1146/annurev-conmatphys-020911-125022.

APPENDIX I: HARMONIC OSCILLATOR

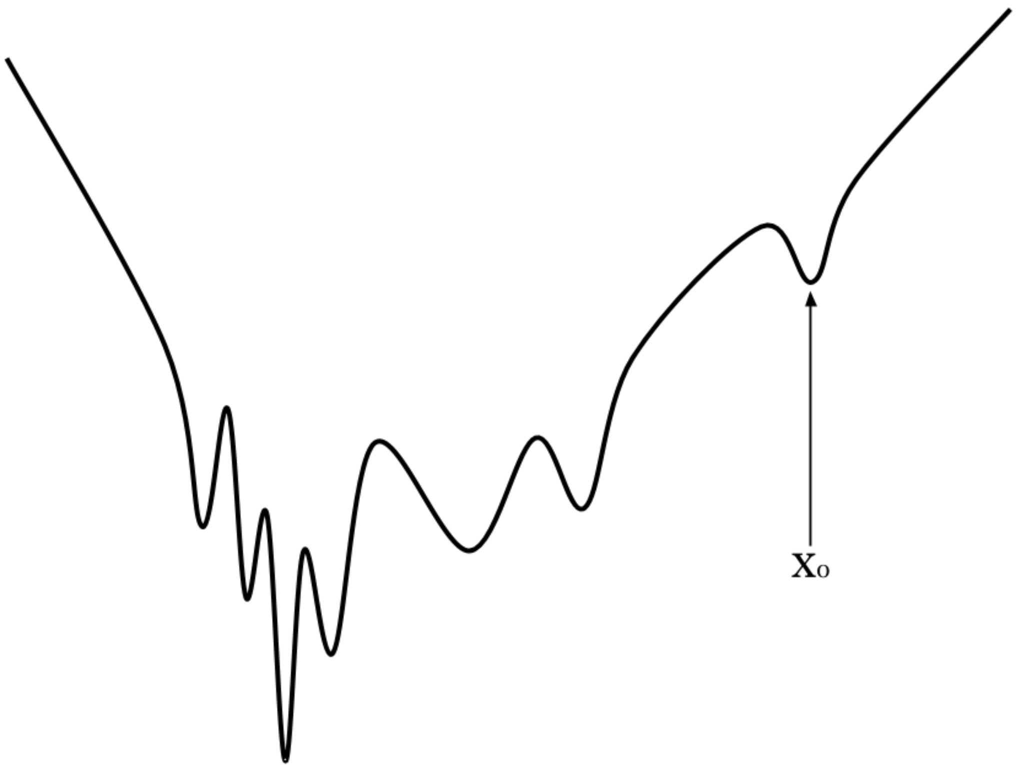

Figure 48: Arbitrary potential with the point x_0 corresponding to an approximately parabolic region.

The harmonic oscillator system will be of importance to our analysis of the radiation field. Here we follow the algebraic derivation of the quantum states in one dimension as demonstrated in *Introduction to Quantum Mechanics* (Griffiths 2004).

Consider the arbitrary potential function in the Figure 48. The harmonic oscillator potential is a good approximation to arbitrary potentials near the regions of vanishing derivatives. These regions are considered to be approximated parabolic. Consider the Taylor Series expansion of the potential function about the point x_0 given by

$$V(x) \cong V(x_0) + V'(x_0)[x - x_0] + \frac{V''(x_0)}{2}[x - x_0]^2 + \cdots , \tag{1}$$

where the first term is a constant that has no bearing on the compulsion of the particle to following simple harmonic motion and the second term vanishes since x_0 is a local minimum. Terms that are of higher order than the third term have contributions approaching zero.

We are left with a term of the following form:

$$\frac{V''(x_0)}{2}[x - x_0]^2 \rightarrow \frac{1}{2}kx^2, \tag{2}$$

where $V''(x_0) \rightarrow k$ is a constant factor characteristic of the system and $x_0 = 0$ is the equilibrium position such that x is the displacement from this position. This potential gives rise to Hooke's Law given by (Hooke 1678)

$$F = -\nabla V = -kx. \tag{3}$$

Via Newton's Second Law, we have:

$$-kx = m\frac{d}{dt}x, \tag{4}$$

where $\omega^2 \equiv k/m$ and ω is the angular frequency.

Applying the Schrödinger equation (Schrödinger 1926) to Equation 2, we get

$$\left\{-\frac{\hbar^2}{2m}\frac{d^2}{dx^2} + \frac{1}{2}m\omega^2 x^2\right\}|\psi\rangle = E\,|\psi\rangle\,, \tag{5}$$

where ψ is the wave function of the harmonic oscillator system that describes its probability amplitude and E is the energy of the system. Dividing by a factor of 2m and substituting in the momentum operator $\hat{p}$ and the Hamiltonian operator $\hat{H}$ we obtain

$$\frac{1}{2m}\left\{\hat{p}^2 + (m\omega x)^2\right\} = \hat{H}\,|\psi\rangle\,. \tag{6}$$

This can be written in terms of two operators given by

$$\hat{a} \equiv \frac{1}{\sqrt{2m}}\left(\frac{\hbar}{i}\frac{d}{dx} - im\omega x\right) \tag{7a}$$

$$\hat{a}^\dagger \equiv \frac{1}{\sqrt{2m}}\left(\frac{\hbar}{i}\frac{d}{dx} + im\omega x\right), \tag{7b}$$

where $\hat{a}$ and $\hat{a}^\dagger$ do not commute. Due to this, we can apply them sequentially to an arbitrary function of in order to discover their effect:

$$\hat{a}\hat{a}^\dagger f = \frac{1}{2m}\left(\frac{\hbar}{i}\frac{d}{dx} - im\omega x\right)\left(\frac{\hbar}{i}\frac{d}{dx} + im\omega x\right) f \tag{8a}$$

$$= \frac{1}{2m}\left[\left(\frac{\hbar}{i}\frac{d}{dx}\right)^2 + (m\omega x)^2 + \hbar m\omega\right] f. \tag{8b}$$

This implies that operating with $\hat{a}^\dagger\hat{a}$ results in an extra factor of $\hbar\omega/2$:

$$\hat{a}\hat{a}^\dagger = \frac{1}{2m}\left[\left(\frac{\hbar}{i}\frac{d}{dx}\right)^2 + (m\omega x)^2\right] + \frac{1}{2}\hbar\omega. \tag{9}$$

Equation 6 then becomes

$$\left(\hat{a}\hat{a}^\dagger - \frac{1}{2}\hbar\omega\right)\left|\psi\right\rangle = E\left|\psi\right\rangle. \tag{10}$$

Similarly, if the operators are applied in the opposite order Equation 6 becomes

$$\left(\hat{a}^\dagger\hat{a} + \frac{1}{2}\hbar\omega\right)\left|\psi\right\rangle = E\left|\psi\right\rangle. \tag{11}$$

Consider $\hat{a}$ acting on the wave function such that

$$\left(\hat{a}^\dagger\hat{a} + \frac{1}{2}\hbar\omega\right)\hat{a}^\dagger\left|\psi\right\rangle = \left(\hat{a}^\dagger\hat{a}\hat{a}^\dagger + \frac{1}{2}\hbar\omega\hat{a}^\dagger\right)\left|\psi\right\rangle = \hat{a}^\dagger\left(\hat{a}\hat{a}^\dagger + \frac{1}{2}\hbar\omega\right)\left|\psi\right\rangle, \tag{12}$$

where inserting Equation 10 results in

$$\hat{a}^\dagger\left(\hat{a}\hat{a}^\dagger - \frac{1}{2}\hbar\omega + \hbar\omega\right)\left|\psi\right\rangle = (E + \hbar\omega)\hat{a}^\dagger\left|\psi\right\rangle. \tag{13}$$

Similarly, $\hat{a}$ is a solution with energy $E - \hbar\omega$. Then, $\hat{a}^\dagger$ is an energy raising operator and $\hat{a}$ is an energy lowering operator. We know have the ability to add or subtract a quanta of energy (e.g. a photon) from the radiation field.

$\hat{a}\hat{a}^\dagger$ is a number operator. By applying $\hat{a}\hat{a}^\dagger = \hat{n}$ to a state vector, the resulting eigenvalue is the number of photons, n, in the associated field:

$$\hat{n}\left|\psi\right\rangle = n\left|\psi\right\rangle, \tag{14}$$

where the energy associated with each value of n is given by

$$E_n = \hbar\omega\left(n + \frac{1}{2}\right). \tag{15}$$

The wave function $|\psi\rangle$ can be found by applying the annihilation operator to the ground state $|0\rangle$. Since we know that a state with energy less than zero is prohibited, we obtain

$$\begin{aligned}
&\hat{a}\,|0\rangle = 0 && \text{(16a)}\\
&\Rightarrow \frac{1}{\sqrt{2m}}(\hat{p} - im\omega x)\,|0\rangle = 0\\
&\Rightarrow \left(\hbar\frac{d}{dx} + m\omega x\right)|0\rangle = 0\\
&\Rightarrow \int \frac{d\,|0\rangle}{|0\rangle} = -\int \frac{m\omega x}{\hbar}dx\\
&\Rightarrow \ln|0\rangle = -\frac{m\omega x^2}{2\hbar} + C_0\\
&\Rightarrow |0\rangle = A_0 \exp\left(-\frac{m\omega x^2}{2\hbar}\right),
\end{aligned}$$

where A_0 is an overall constant that can be obtained by normalizing the wave function. Using the fact that the photon must exist somewhere in space, we obtain

$$\begin{aligned}
&\int_{-\infty}^{\infty} \left||0\rangle\right|^2 dx = 1 && \text{(17a)}\\
&\Rightarrow |A_0|^2 \int_{-\infty}^{\infty} \exp\left(-\frac{m\omega x^2}{\hbar}\right) dx = 1\\
&\Rightarrow A_0 = \left(\frac{m\omega}{\hbar\pi}\right)^{\frac{1}{4}}\\
&\Rightarrow |0\rangle = \left(\frac{m\omega}{\hbar\pi}\right)^{\frac{1}{4}} \exp\left(-\frac{m\omega x^2}{2\hbar}\right),
\end{aligned}$$

where we can apply the creation operator to the ground state n times to obtain any state $|n\rangle$. Moreover, the lowering and raising operators can be applied to any state $|n\rangle$ to obtain the corresponding raised or lowered state with the following normalized equations:

$$\hat{a}^\dagger \left|n\right\rangle = \sqrt{n+1} \left|n+1\right\rangle \tag{18a}$$

$$\hat{a} \left|n\right\rangle = \sqrt{n} \left|n-1\right\rangle . \tag{18b}$$

APPENDIX II: PRELIMINARY MEASUREMENTS WITH SCONTEL SNSPD DEVICES

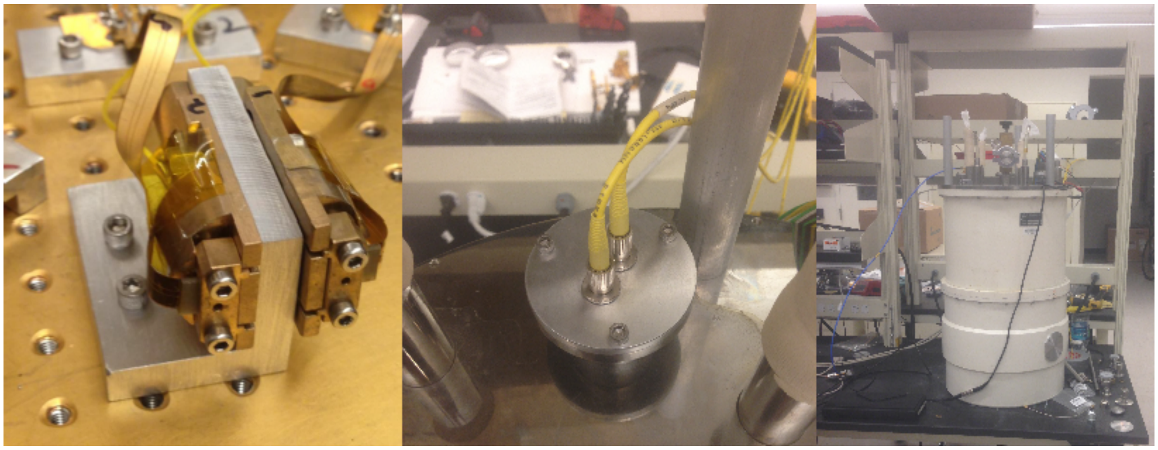

Figure 49: The leftmost picture shows the SCONTEL SNSPD devices mounted on the 4K stage. The middle picture shows the hermetic fiber optic feedthrough. The rightmost picture shows the Janis Research Co., Inc. LN2/LHe cryostat.

Two SNSPD devices made by SCONTEL were received from Cardiff University in May 2014. They were mounted inside a liquid helium cryostat. A hermetic fiber optic feedthrough was designed in Autodesk Inventor to provide light to the nanowires. Figure 49 shows the detectors, the feedthrough, and the cryostat.

The first step we took was to characterize one of the detectors to determine its critical temperature. We took IV curves (Figure 50a) for small steps in temperature along the superconducting transition by current biasing the SNSPD and reading out the voltage across the device. From this data, R(T), α, P(T), and G were determined.

Resistance as a function of base temperature is found via the slope of each of the IV curves and the temperature coefficient is found via $\alpha = \frac{1}{R}\frac{dR}{dT}$ and is plotted along with R(T) in Figure 51b. The superconducting phase transition is clearly evident with the critical temperature found to be 9.65K and $\Delta T_C \sim 0.6$K.

If we plot R versus I_{bias} for multiple temperatures in ΔT_C, we can extract the I_{bias} that it took at each chosen temperature to reach the same resistance along the

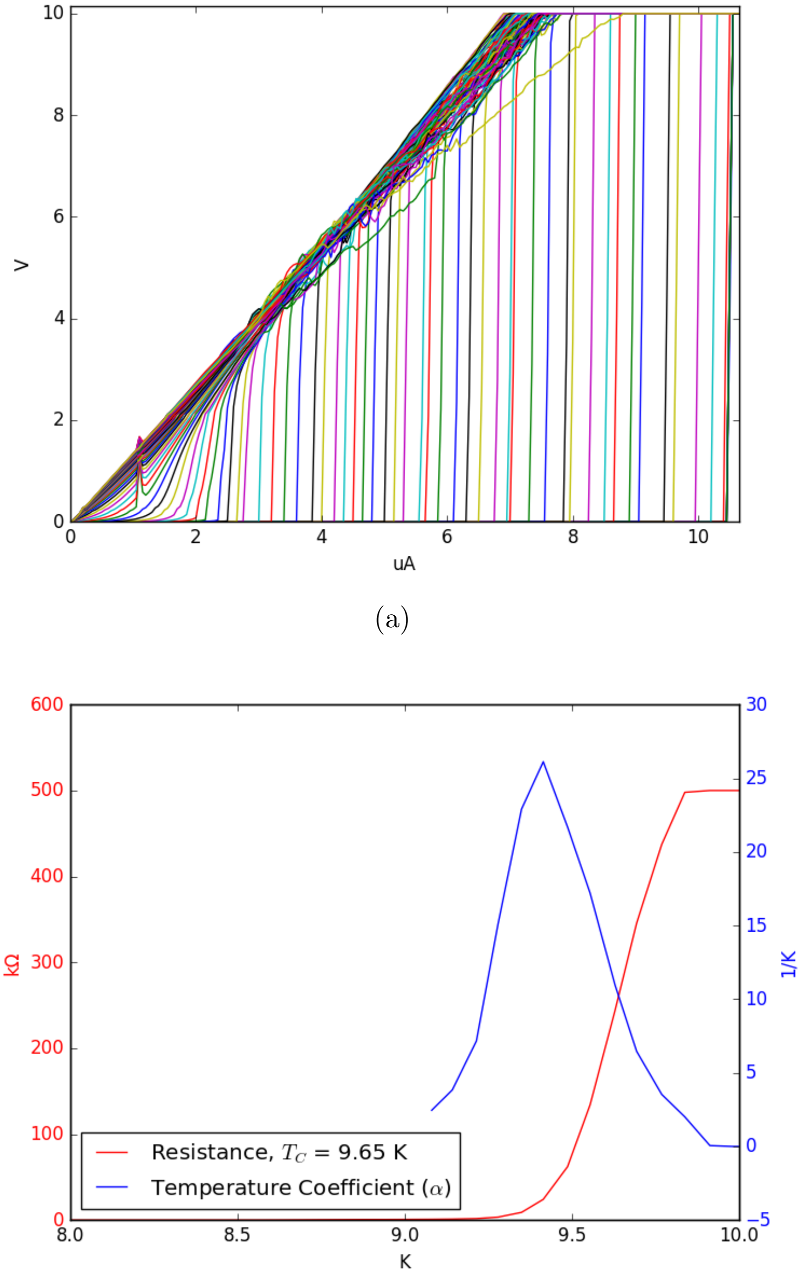

(a)

(b)

Figure 50: (a) IV curves as a function of base temperature. (b) Superconducting transition and temperature coefficient.

transition. We chose 50kΩ for the resistance (10% of the normal resistance). Figure 51a shows the IV curves used for this analysis.

As the base temperature increases, the I_{bias} required to reach 50 kΩ decreases, so the required power decreases as shown in Figure 51b. Plotting power versus the base temperature yields the thermal conductance, G, via dP/dT. We obtain G = 382.2nW/K.

Most of the cool-downs that we did were aimed at measuring the count rate at different wavelengths ranging from the optical to the NIR. A thermal source was coupled to a monochromator and photon counts were measured as a function of bias current. The setup is shown in Figure 52. Figure 53 shows an example of single photon pulses. Figure 54 shows the photon counts for varying wavelengths.

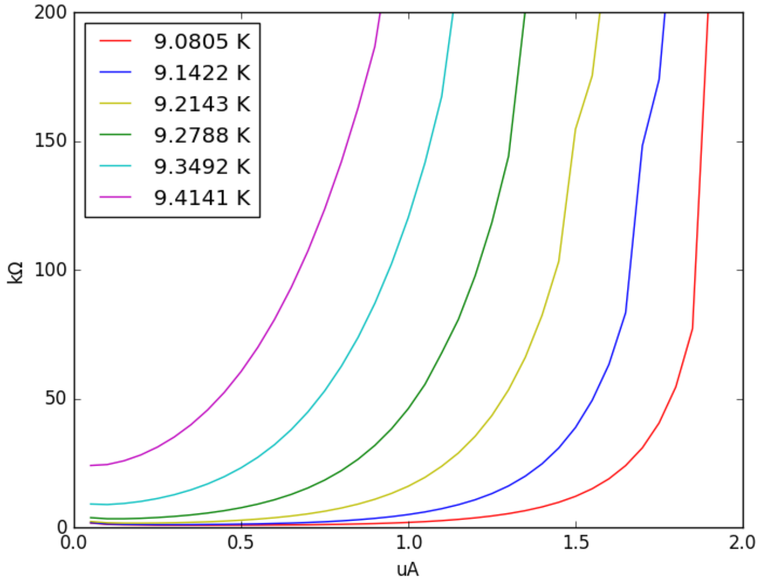

(a)

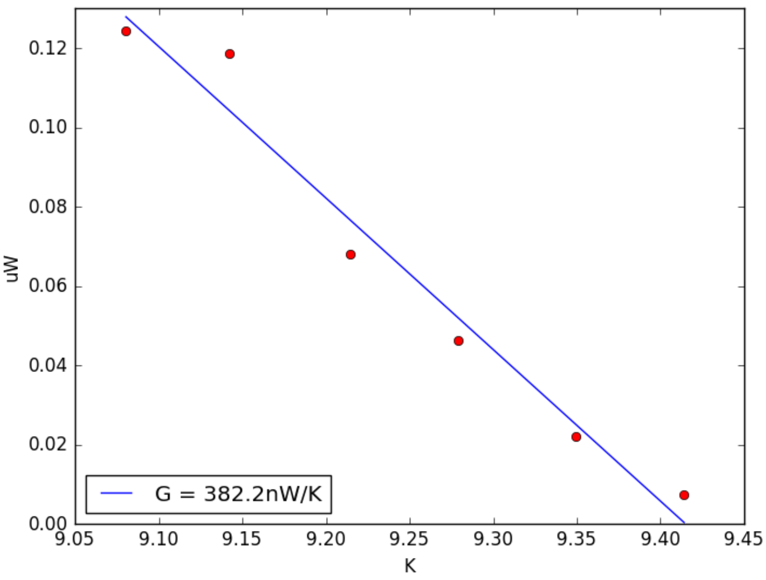

(b)

Figure 51: (a) Resistance as a function of bias current and (b) power as a function of base temperature for points along the superconducting phase transition.

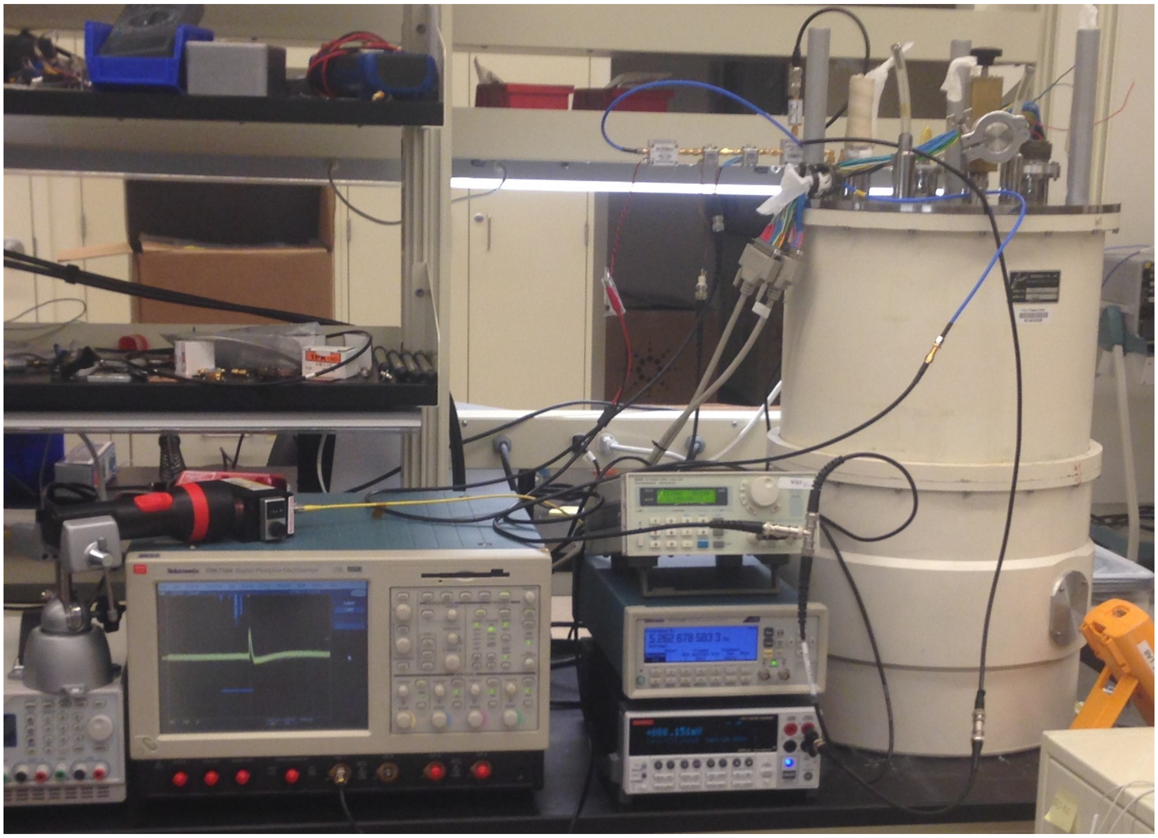

Figure 52: Experimental setup for counting single photon pulses. An incandescent source was fed into a monochromator. A fiber optic cable feeds the filtered light into the cryostat and onto the nanowire. The pulses are observed on the oscilloscope and counted with a frequency counter.

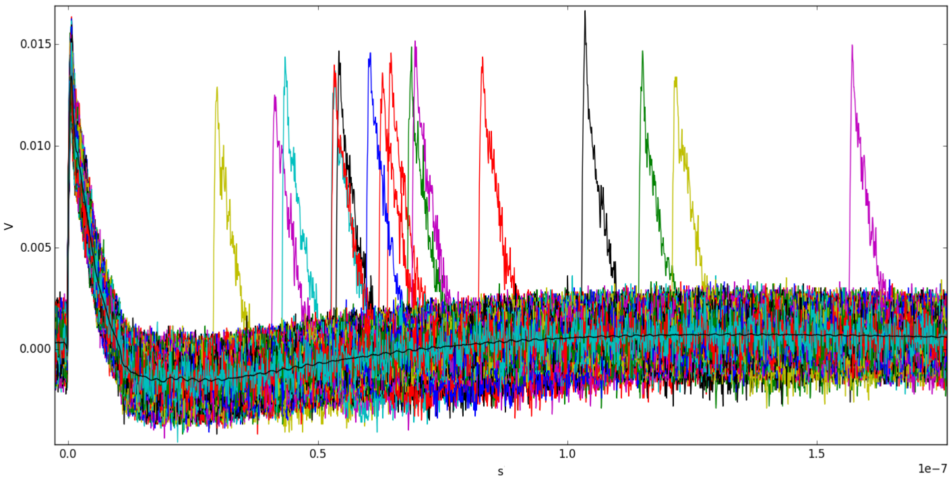

Figure 53: Single photon pulses from a SCONTEL SNSPD. The pulses are approximately 10ns wide and 15mV high.

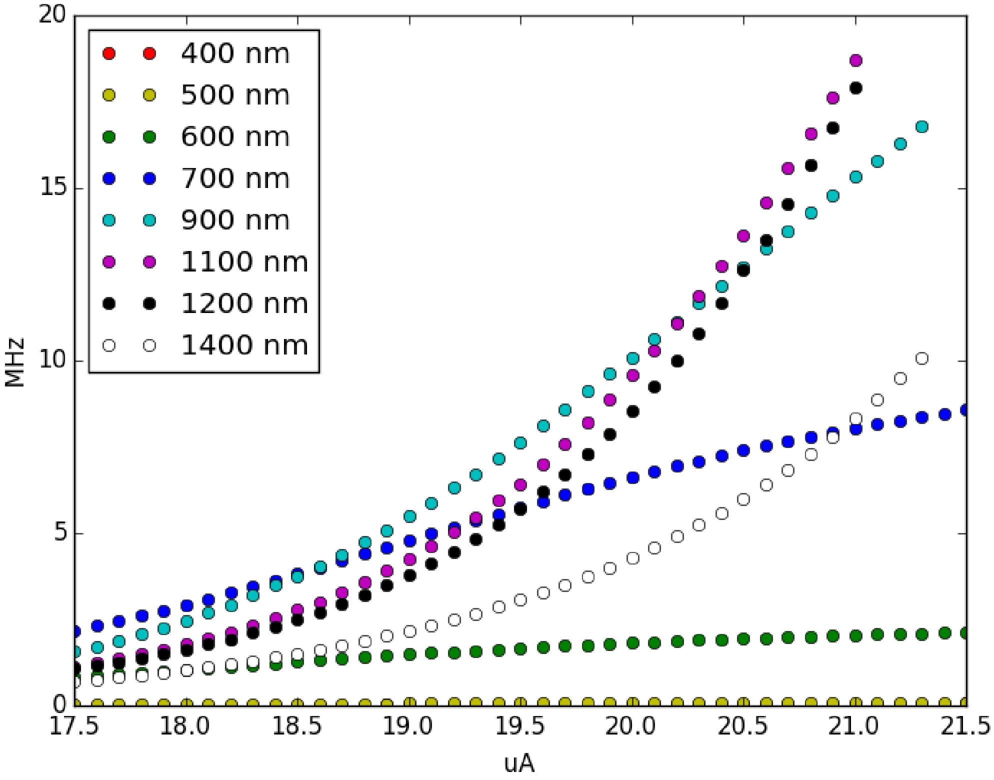

Figure 54: Count rate as a function of bias current for a SCONTEL SNSPD. A maximum count rate of ∼18MHz was achieved for 1100nm photons. These devices are most efficient in the near infrared range.

APPENDIX III: SUMITOMO RP-082 CRYOSTAT TESTBED SETUP

Most of the testing completed for this dissertation was done with a Sumitomo RP-082, closed cycle, cryogenic cooler. The critical temperature of our devices was determined to be $\sim$ 7K. Our intention was then to condition the coldplate (second stage) of the cryostat to reach $\leq$ 4K. This was achieved by minimizing thermal loading onto the second stage and by the efficient heat transferring from the cold head to the stages of the cryostat via copper braids.

Due to a (mostly) fixed thermal mass when the first and second stage were installed, concerns of thermal loading were focused on radiation and conduction. Thermal shielding and isolation were therefore the focus when setting up the testbed. The heat loading from radiation goes as the surface area of the object on which the radiation is incident. Since the coldplate is large, this was a major concern. To mitigate the effects of radiation, shielding in the form of aluminum cylinders encased the plates. Additionally, multi-layer insulation (MLI) was attached to the outside surface of both shields (see Figure 55) and aluminum tape was applied to the inside surfaces. Aluminum tape was also applied to the first stage.

The heat transferred via radiation is given as

$$Q = \epsilon \sigma T^4, \tag{19}$$

where Q is the heat transferred, ϵ is the emissivity, σ is the Stefan-Boltzmann constant, and T is the temperature. The first stage is made of unpolished aluminum. Due to its low emissivity, MLI was applied to the surface and to the shield. The MLI on the shield consisted of ten layers of aluminized mylar (high emissivity) thermally insulted from each other and the surface with gauze netting. The plate had eight layers.

Another source of heat transfer that was minimized was that from the supporting struts between the stages. The struts are in contact with both stages and 300K.

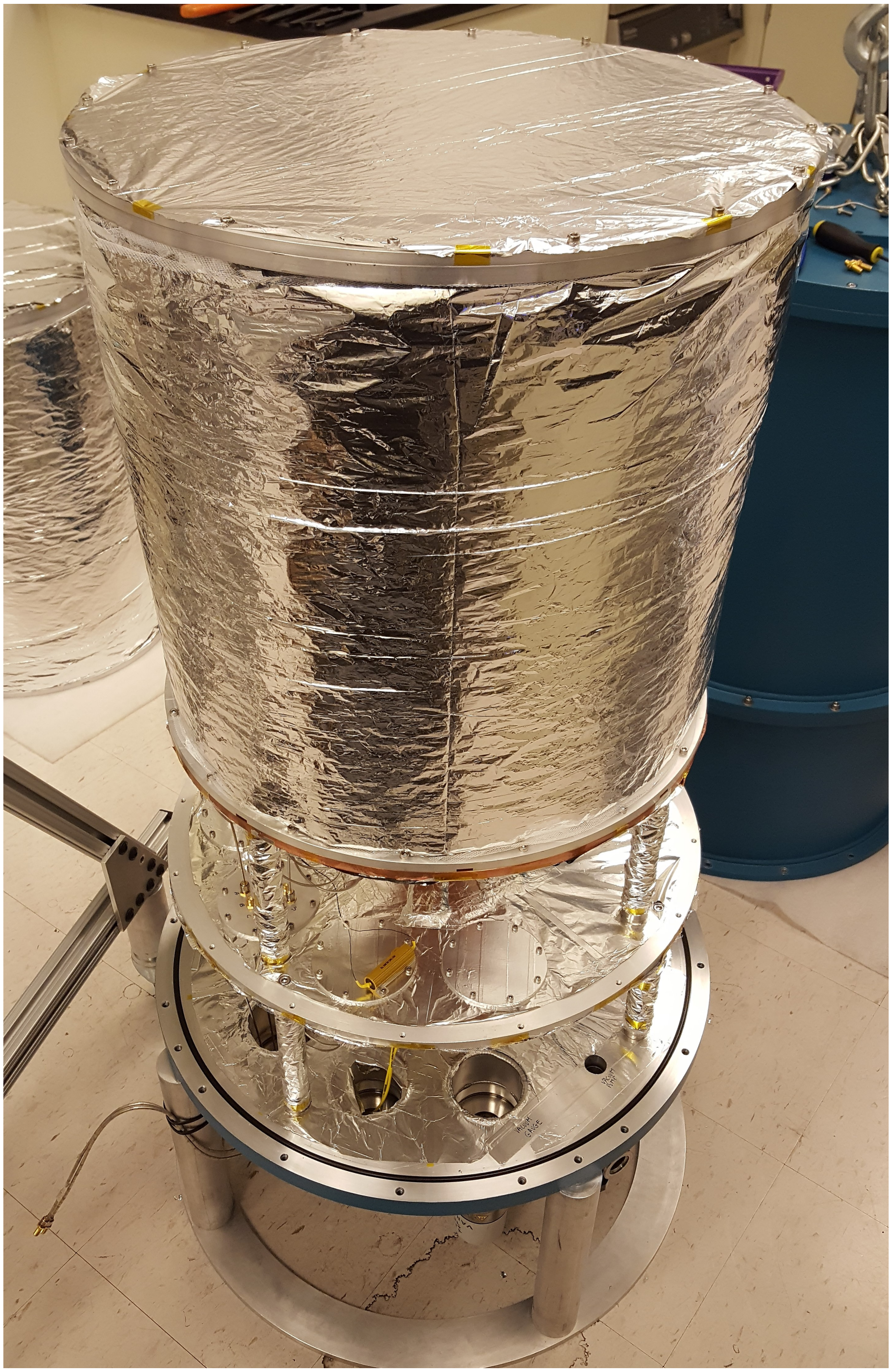

Figure 55: The 300K and first stage are shown along with the inner MLI-covered shield and supporting struts.

Conductive heat transfer is given as

$$\delta Q = \frac{Ak(t)\delta T}{L} \tag{20}$$

where A is the cross-sectional area, k is the thermal conductivity factor, T is the temperature, and L is the length. Integrating Equation 20 to arrive at the heat transferred between regions of varying temperatures, we arrive at

$$Q = \frac{AK}{L}, \tag{21}$$

where K is the value of the integral of thermal conductivity from the lower temperature to the higher temperature.

The cross-sectional area was minimized by preparing hollow struts with 10mil thick walls. The thermal conductivity was minimized by using stainless steel (high mechanical strength, low thermal conductivity). The expected power transfered from 300K to the first stage and from the first stage to the second stage was 3W and 0.1W, respectively. Additionally, two layers of MLI was added to the struts to minimize radiative heat loading.

The second stage was gold plated to increase thermal contact for cooling devices as well as to increase emissivity. Two layers of MLI were added to the bottom of the plate. The second stage shield was fitted with ten layers of MLI. The final base temperature reached was ~ 2.25K (see Figure 56) with multiple devices attached to the coldplate along with a sorption fridge.

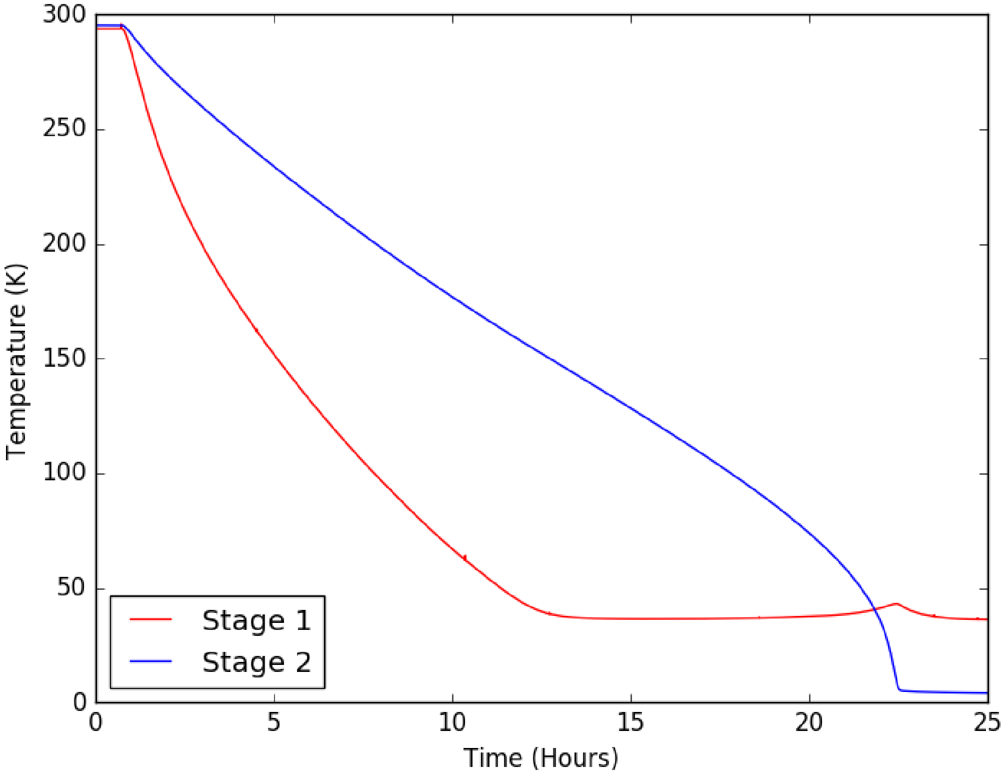

Figure 56: Temperature versus time for the first and second stages of the cryostat.

APPENDIX IV: SIGNAL-TO-NOISE DERIVATION

Our sources are incoherent and therefore follow Bose-Einstein statistics. The occupation number in this case is

$$n_{occ} = \frac{1}{e^{\frac{h\nu}{kT}} - 1}, \tag{22}$$

where h is Plank's constant, ν is the central frequency of the light, k is Boltzmann's constant, and T is the temperature of the source.

The occupation number is the number of photons per second per mode per Hertz and is representative of the probability that a photon is occupying a particular state. If two detectors are measuring emitted radiation from a single source, then the probability that both detectors will measure a photon in the same state (i.e. the same time) is $P = n_{occ}^2$. If we integrate for some amount of time τ_{int}, we will detect the following number of photons:

$$n_{correlations} = \epsilon \Gamma_{det} n_{occ} \tau_{int}, \tag{23}$$

where Γ_{det} is the number of photons per second detected by a detector, n_{occ} is the occupation number, and τ_{int} is the integration time. These are the correlated photons (i.e. the signal). Multiplying Γ_{det} and τ_{int} gives the number of photons counted at one detector in a given amount of time and multiplying this value by the probability of detecting a photon in the same state at the second detector gives the number of correlations. This can be written as

$$S = \epsilon^2 n_{occ}^2 \Delta\nu \tau_{int}. \tag{24}$$

In addition to photons that are occupying the same state causing these detected coincidences, there are random coincidences that are not correlated. This is where the noise associated with this measurement arises. Consider two detectors A and B. The number of coincidences that are random can be determined by multiplying the number of coincidences in A by the probability that for a particular photon detected in A, a photon is detected in B within the detector time constant τ_{det}.

The number of coincidences in A is given by

$$n_A = \epsilon n_{occ} \Delta\nu \tau_{int}. \tag{25}$$

The probability that another photon will be detected in B within τ_{det} is

$$P(B : A) = \epsilon n_{occ} \Delta\nu \tau_{det}, \tag{26}$$

where this is just the rate of photons detected by B in the time window for the photons to be considered coincident with a photon arriving at A.

The number of random coincidences detected is then given by

$$n_{random} = n_A P(B : A) = \epsilon^2 n_{occ}^2 \Delta\nu^2 \tau_{int} \tau_{det}. \tag{27}$$

Since the noise associated with random coincidences is Poissonian, we get

$$N = \sqrt{n_{random}} = \epsilon n_{occ} \Delta\nu \sqrt{\tau_{int} \tau_{det}}. \tag{28}$$

We arrive at the signal-to-noise ratio for the HBT experiment:

$$\frac{S}{N} = \epsilon n_{occ} N_{modes} \sqrt{\frac{\tau_{int}}{\tau_{det}}}. \tag{29}$$

APPENDIX V: SYSTEM EFFICIENCY

The efficiency of each detector channel can be determined by calculating the expected throughput of the system with a given configuration and comparing it to the measured count rates at each detector. In our system, the number of photons incident on a detector that are detected is given by

$$\Gamma_{det} = \epsilon n_{occ} \Delta\nu N_{modes}, \tag{30}$$

where ϵ is the overall efficiency of the system leading up to a particular detector that determines the number of photons that are counted based on the number of photons that arrive at the beginning of the system, n_{occ} is the occupation number, $\Delta\nu$ is the observed bandwidth of the radiation field, and N_{modes} is the number of modes.

The system efficiency for a detector is then given by

$$\epsilon = \frac{\Gamma_{det}}{\Gamma_{det}(\epsilon = 1)}, \tag{31}$$

where Γ_{det} is the measured count rate at the detector and $\Gamma_{det}(\epsilon = 1)$ is the expected throughput given 100% efficiency.

The number of modes can be determined by comparing the minimum distance requirement for a single mode from the source to pass through the pinhole to the actual position of our pinhole. For the pinhole to be the size of one spatial mode, the resolving power needs to equal the angular size of the pinhole. In one-dimension, this is given by

$$\frac{1.22\lambda}{D_{pinhole}} = \frac{R_{source}}{d}, \tag{32}$$

where λ is the central wavelength, $D_{pinhole}$ is the pinhole diameter, R_{source} is the source radius, and d is the distance from the source to the pinhole. For $\lambda = 650$nm, $d = 0.2$m. This means that as long as the pinhole is 0.2m or greater from the source, only light from a single spatial mode is incident on our detectors. For zero-point correlation measurements, this is ideal.

APPENDIX VI: PHOTON NUMBER CALCULATION FROM HOTSPOT ANALYSIS

When a photon is incident on the active area of a nanowire, a hotspot is formed. The size of the hotspot can be estimated from a comparison of the number of quasiparticles generated per photon with the number of quasiparticles available per unit volume. The number of quasiparticles generated by a single-photon is given as

$$N_{qp} = \frac{\eta E_\gamma}{\Delta}, \tag{33}$$

where $\eta \sim 50\%$ is the internal quasiparticle generation efficiency for absorbed optical power, $E_\gamma \cong 0.95\text{eV}$ is the energy of a $1.3\mu m$ photon, and $\Delta = 1.1\text{meV}$ is the band-gap energy. N_{qp} is then found to be ~ 440 quasiparticles.

The number of quasiparticles available per unit volume is given as

$$n_{qp} = 4N_0\Delta \ln 2, \tag{34}$$

where $N_0 \cong 1.6 \times 10^{10}/\text{eV}/\mu\text{m}^3$ is the density of states at the Fermi level such that n_{qp} is found to be 4.88×10^7 quasiparticles per micron.

The volume of the hotspot is then given as

$$V_{spot} = \frac{N_{qp}}{n_{qp}} = 9 \times 10^3 nm^3, \tag{35}$$

where since the thickness of the NbN film is 4 nm, the area of the hotspot is $A_{spot} = 2250\text{nm}^2$. It can be shown that the change in kinetic inductance, δL_K, is dependent on this area and the width of the hotspot, w_{spot}. While w_{spot} and the length of the hotspot, ℓ_{spot}, may vary, A_{spot} will remain constant (Figure 57).

The total kinetic inductance of the nanowire before a photon is incident is given as

$$L_K^0 = \mathcal{L}_K N_\square^0, \tag{36}$$

where $\mathcal{L}_K$ is the kinetic inductance per square and is a constant of the NbN film and $N_\square^0$ is the number of squares. $N_\square^0$ can be expressed as the length of the nanowire, ℓ_n, divided by the width of the nanowire, w_n.

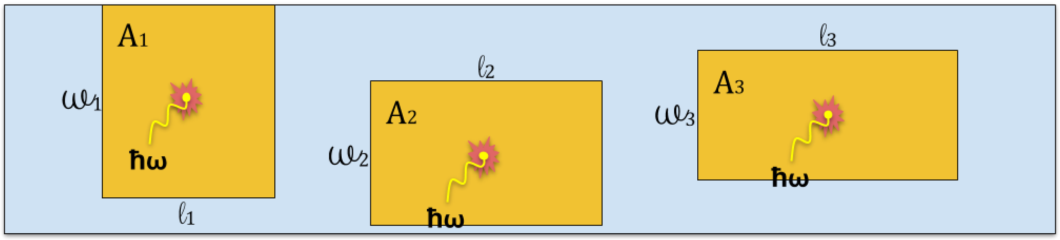

Figure 57: Nanowire strip with three hotspots of equal area ($A_1 = A_2 = A_3$), where $w_1 \neq w_2 \neq w_3$ and $\ell_1 \neq \ell_2 \neq \ell_3$.

The kinetic inductance of the nanowire in the presence of a photon-generated hotspot is given as

$$L_K^1 = L_K^0 - \mathcal{L}_K \frac{\ell_{spot}}{w_n} + \mathcal{L}_K \frac{\ell_{spot}}{w_n - w_{spot}}, \tag{37}$$

where $\delta L_K = L_K^1 - L_K^0$. Then, the second term and third term account for the change in the kinetic inductance such that

$$\delta L_K = \mathcal{L}_K \ell_{spot} \left[\frac{1}{w_n - w_{spot}} - \frac{1}{w_n} \right] \cong \frac{\mathcal{L}_K A_{spot} \beta}{w_n^2}, \tag{38}$$

where β is a factor that relates w_n to w_{spot}. Moreover, if α is a multiplier that gives $w_n = \alpha w_{spot}$, then $\beta = (\alpha^{-1} - \alpha^{-2})^{-1}$. If w_{spot} is $\sim 90\%$ of w_n, then $\alpha \cong 1.11 \Rightarrow \beta \cong 11.1$.

The kinetic inductance per square is given as

$$\mathcal{L}_K = L_{tot} \frac{w_n}{\ell_n}, \tag{39}$$

where $L_{tot} = 600\text{nH}$ is the total kinetic inductance of the nanowire based on the experimental value of the resonance and the capacitance of the pixel, $w_n = 60\text{nm}$, and $\ell_n = 500\mu\text{m}$ such that $\mathcal{L}_K = 72\text{pH}/\square$.

The average change in kinetic inductance can be expressed as

$$\delta L_{avg} = \beta \mathcal{L}_K \Gamma_\gamma \tau_\epsilon, \tag{40}$$

where Γ_γ is the number of photons per second incident on the nanowire and τ_ϵ is the energy relaxation time.

The average change in kinetic inductance is also a function of the measured shift in frequency per mA of LED current and is given as

$$\delta L_{avg} = -2\frac{\delta f}{f_0}L_{tot}, \tag{41}$$

where $\delta f = 94$ Hz/mA is the shift in frequency and $f_0 = 45.85$MHz is the resonant frequency such that $\delta L_{avg} = -2.46$pH.

Solving for Γ_γ in Equation 40 we arrive at

$$\Gamma_\gamma = \frac{\delta L_{avg}}{\beta \mathcal{L}_K \tau_\epsilon}, \tag{42}$$

where $\tau_\epsilon = 50$ps such that $\Gamma_\gamma = 6.16 \times 10^7$ photons/s/mA. This can be compared to $\Gamma_\gamma = 1 - 5 \times 10^8$ photons/s/mA as calculated in Chapter 5.2.1 from the analysis of the effect of the change in quasiparticle number as a function of absorbed power.

APPENDIX VII: ABSORBED POWER FROM CHANGE IN QUASIPARTICLE NUMBER

We measured S_{21} for the resonators as a function of base temperature and at a fixed base temperature ($2.7K$) as a function of LED current. If we compare the frequency shift of the resonance as a function of LED current with the temperature dependence (Figures 58 and 59), we can calculate an effective temperature shift of the quasiparticles as a function of LED current with

$$\delta T = \frac{\Delta T_{base}}{\Delta I_{LED}}, \tag{43}$$

where $\delta T_{SNRSPD1} = 171\mu\mathrm{K/mA}$ and $\delta T_{SNRSPD2} = 197\mu\mathrm{K/mA}$. This effective temperature shift is a lower estimate because it assumes that the energy from each photon is distributed evenly throughout the nanowire. In fact, the energy from each photon is deposited locally and creates a hotspot of normal metal around which the current has to flow.

From the measured critical current and critical temperature, we calculated the change in quasiparticles per mA at low temperatures with

$$\frac{\delta N_{qp}}{\delta T} = \frac{N_{qp}}{T}\left(\frac{1}{2} + \frac{\Delta}{kT}\right), \tag{44}$$

where $\Delta \sim 1.764kT_C = 1.29\mathrm{meV}$, for $T_C \approx 8.5\mathrm{K}$, and $T \approx 2.74\mathrm{K}$. $N_{qp} \sim 10^5$ quasiparticles is found via analysis of the non-linear kinetic inductance and equating the scaling energy with the condensation energy of the superconductor.

The absorbed power per mA of LED current can be found by rearranging Equation 4.49 and is given by

$$P_{abs} = \tfrac{\delta N_{qp}\Delta}{\eta\tau_{qp}}.$$

In NbN HEB detectors, the bandwidth is about $3 - 5\mathrm{GHz}$. This corresponds to a time constant of $30 - 50\mathrm{ps}$. We will consider a lower bound to the time constant to be 20ps and an upper bound to be 1ns. Assuming a typical value for the production efficiency, $\eta = 0.57$, we find a range of $P_{abs} = 1.65 \times 10^{-11} - 8.23 \times 10^{-10}$W/mA for SNRSPD1 and $P_{abs} = 2.24 \times 10^{-11} - 1.12 \times 10^{-9}$W/mA for SNRSPD2.

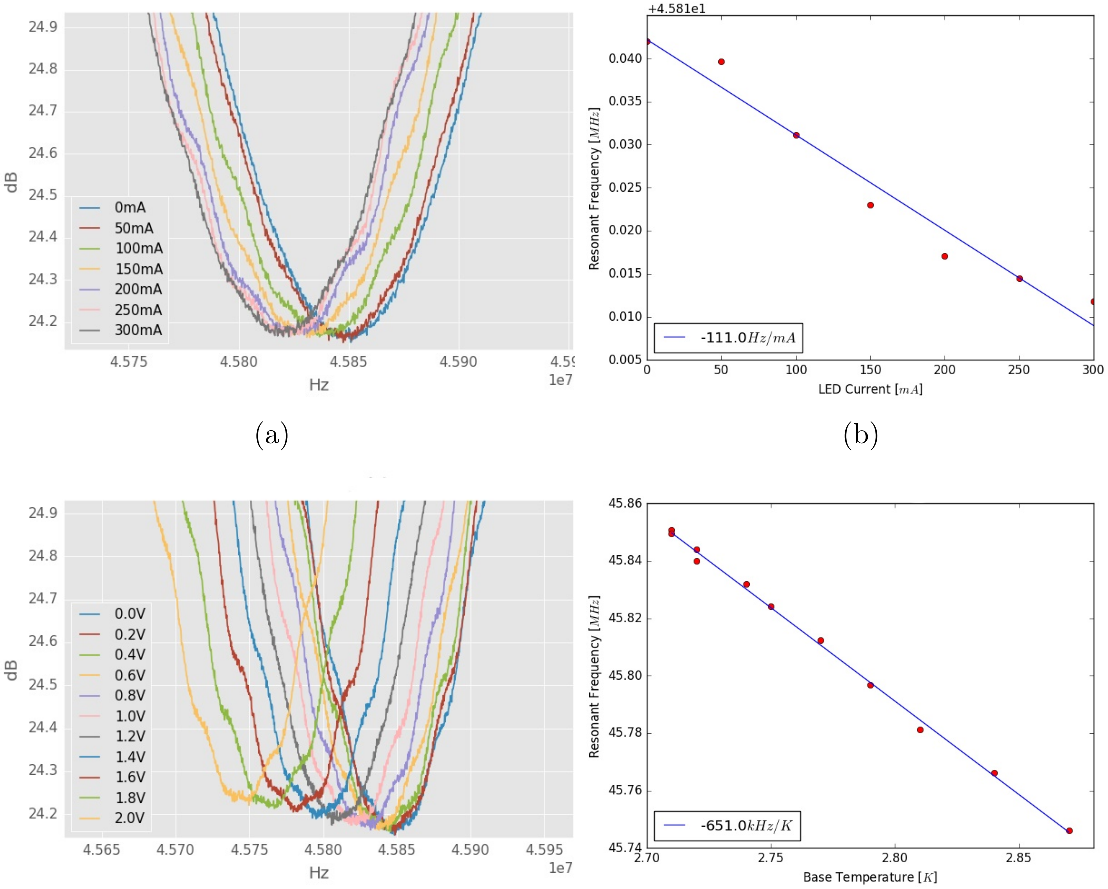

(a) (b)

(c) (d)

Figure 58: (a) Zoomed-in resonance shift as a function of LED current for SNRSPD1. (b) Linear fit for resonant frequency as a function of LED current for SNRSPD1. This yields a shift of 111Hz/mA. (c) Zoomed-in resonance shift as a function of base temperature. (d) Linear fit for resonant frequency as a function of base temperature. This yields a shift of 6.51×10^5Hz/K.

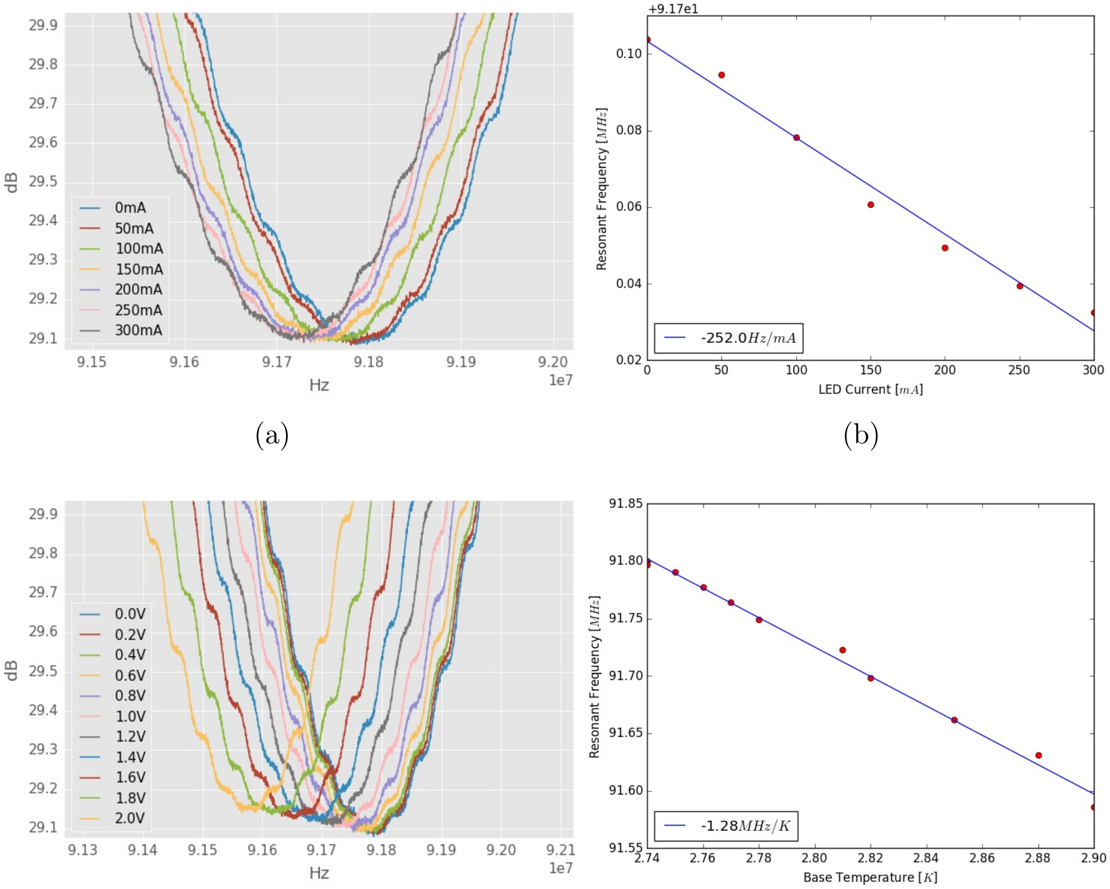

(a) (b)

(c) (d)

Figure 59: (a) Zoomed-in resonance shift as a function of LED current for SNRSPD2. (b) Linear fit for resonant frequency as a function of LED current for SNRSPD2. This yields a shift of 252Hz/mA. (c) Zoomed-in resonance shift as a function of base temperature. (d) Linear fit for resonant frequency as a function of base temperature. This yields a shift of 1.28×10^6Hz/K.

APPENDIX VIII: RESONANCE CURVE FITTING

We fit the resonance curves presented in this dissertation with *emcee*, which is a Python code Markov-chain Monte-Carlo (MCMC) method developed at MIT (Foreman-Mackey et al. 2013). The fits were consistently within a tenth of a dB (Figure 60). Q_r is limited by the coupling to the transmission line and Q_i is limited by loss in the parallel SMD capacitor.

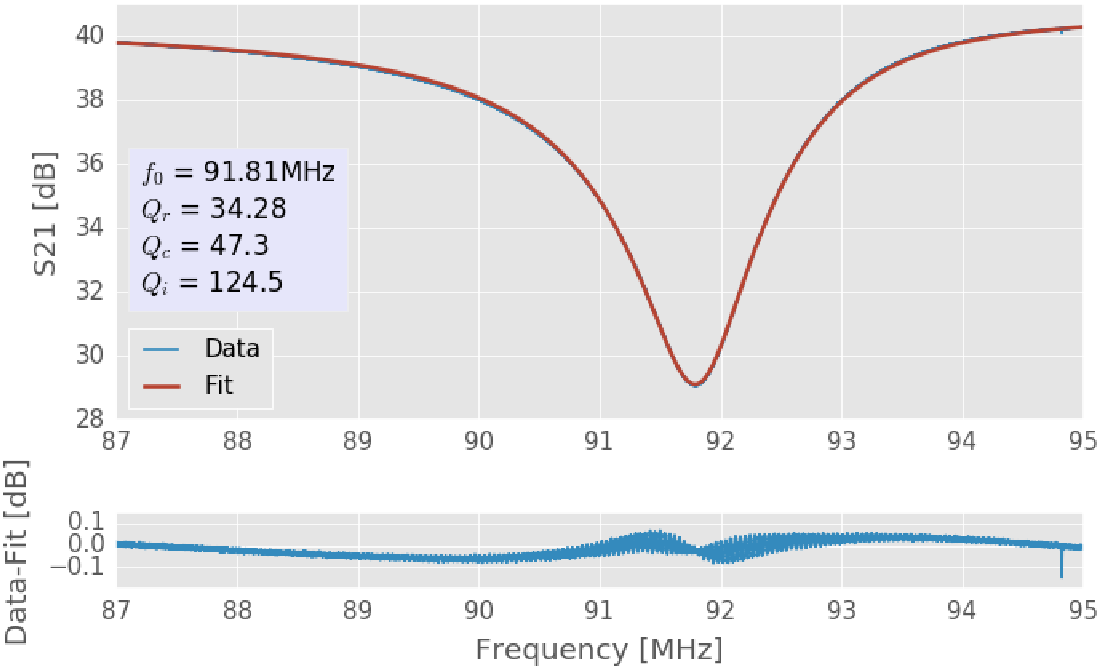

Figure 60: Example resonance fit of an SNRSPD S_{21} curve using *emcee*.